University of Denver
Digital Commons @ DU

Electronic Theses and Dissertations | Graduate Studies

1-1-2019

Empirical Evaluation of Ground, Ceiling, and Wall Effect for Small-Scale Rotorcraft

Stephen Austin Conyers
University of Denver

Follow this and additional works at: https://digitalcommons.du.edu/etd

 Part of the Mechanical Engineering Commons

Recommended Citation

Conyers, Stephen Austin, "Empirical Evaluation of Ground, Ceiling, and Wall Effect for Small-Scale Rotorcraft" (2019). *Electronic Theses and Dissertations*. 1570.
https://digitalcommons.du.edu/etd/1570

This Dissertation is brought to you for free and open access by the Graduate Studies at Digital Commons @ DU. It has been accepted for inclusion in Electronic Theses and Dissertations by an authorized administrator of Digital Commons @ DU. For more information, please contact jennifer.cox@du.edu,dig-commons@du.edu.

Empirical Evaluation of Ground, Ceiling, and Wall Effect for Small-Scale Rotorcraft

Abstract

Ground effect refers to the apparent increase in lift that an aircraft experiences when it flies close to the ground. For helicopters, this effect has been modeled since the 1950's based on the work of Cheeseman and Bennett, perhaps the most common method for predicting hover performance due to ground effect. This model, however, is based on assumptions that are often not realistic for small-scale rotorcraft because it was developed specifically for conventional helicopters. It is clear that the Cheeseman-Bennett model cannot be applied to today's multirotor UAVs. Experimental findings suggest that some of the conventional thinking surrounding helicopters cannot be applied directly to rotorcraft using fixed propellers at variable speeds (e.g. multirotors). A parametric multirotor-specific ground effect model is developed and presented to overcome some of the limitations in classical helicopter theory.

Likewise, ceiling effect refers to the apparent increase in lift that a rotorcraft experiences when flying close to a ceiling or any similar surface that is present above the rotor(s). Ceiling effect is similar in principle to ground effect, and can be explained using a similar equation. Ceiling effect, however, was never explored in detail for conventional helicopters because large manned aircraft do not operate in enclosed spaces. For multirotors, the work presented in this dissertation suggests that the classical helicopter theory adequately describes ceiling effect performance.

Wall effect is the phenomena that occurs when a rotorcraft flies near a vertical wall, and has the tendency to pitch towards the wall and be drawn into it. Wall effect is the least-understood of these three areas of interest. Wall effect has not been explored in great detail for any aircraft, and is addressed in detail in this dissertation.

The recent widespread use of small-scale UAVs and the demand for increased autonomy when flying in enclosed environments has created a need for detailed studies of ground effect, ceiling effect and wall effect. Ultimately, this work provides foundations for the development of an improved UAV flight controller that can accurately account for various aerodynamic disturbances that occur near surfaces and structures to improve flight stability.

Document Type

Dissertation

Degree Name

Ph.D.

Department

Engineering

First Advisor

Matthew J. Rutherford

Second Advisor

Kimon P. Valavanis

Keywords

Ceiling Effect, Ground Effect, Helicopter, Mechatornics, Unmanned Aerial Vehicle, Wall effect

Subject Categories
Engineering | Mechanical Engineering

Publication Statement
Copyright is held by the author. User is responsible for all copyright compliance.

This dissertation is available at Digital Commons @ DU: https://digitalcommons.du.edu/etd/1570

EMPIRICAL EVALUATION OF GROUND, CEILING, AND WALL EFFECT FOR SMALL-SCALE ROTORCRAFT

A Dissertation

Presented to

the Faculty of the Daniel Felix Ritchie School of Engineering and Computer Science

University of Denver

In Partial Fulfillment

of the Requirements for the Degree

Doctor of Philosophy

---

by

Stephen A. Conyers

June 2019

Advisors: Matthew J. Rutherford, Ph.D.

and Kimon P. Valavanis, Ph.D.

© Copyright by Stephen A. Conyers 2019

All Rights Reserved

Author: Stephen A. Conyers
Title: EMPIRICAL EVALUATION OF GROUND, CEILING, AND WALL EFFECT FOR SMALL-SCALE ROTORCRAFT
Advisors: Matthew J. Rutherford, Ph.D. and Kimon P. Valavanis, Ph.D.
Degree Date: June 2019

Abstract

Ground effect refers to the apparent increase in lift that an aircraft experiences when it flies close to the ground. For helicopters, this effect has been modeled since the 1950's based on the work of Cheeseman and Bennett, perhaps the most common method for predicting hover performance due to ground effect. This model, however, is based on assumptions that are often not realistic for small-scale rotorcraft because it was developed specifically for conventional helicopters. It is clear that the Cheeseman-Bennett model cannot be applied to today's multirotor UAVs. Experimental findings suggest that some of the conventional thinking surrounding helicopters cannot be applied directly to rotorcraft using fixed propellers at variable speeds (e.g. multirotors). A parametric multirotor-specific ground effect model is developed and presented to overcome some of the limitations in classical helicopter theory.

Likewise, ceiling effect refers to the apparent increase in lift that a rotorcraft experiences when flying close to a ceiling or any similar surface that is present above the rotor(s). Ceiling effect is similar in principle to ground effect, and can be explained using a similar equation. Ceiling effect, however, was never explored in detail for conventional helicopters because large manned aircraft do not operate in enclosed spaces. For multirotors, the work presented in this dissertation suggests that the classical helicopter theory adequately describes ceiling effect performance.

Wall effect is the phenomena that occurs when a rotorcraft flies near a vertical wall, and has the tendency to pitch towards the wall and be drawn into it. Wall effect is the least-

understood of these three areas of interest. Wall effect has not been explored in great detail for any aircraft, and is addressed in detail in this dissertation.

The recent widespread use of small-scale UAVs and the demand for increased autonomy when flying in enclosed environments has created a need for detailed studies of ground effect, ceiling effect and wall effect. Ultimately, this work provides foundations for the development of an improved UAV flight controller that can accurately account for various aerodynamic disturbances that occur near surfaces and structures to improve flight stability.

Acknowledgments

Thank you to my wonderful wife Mary for standing by me from the very beginning,
and through so many years of school.

Thank you to my parents David, Julie, Kate, and Buddy, my sister Hallie,
my grandma Betty and grandpa Wiz for always believing in me and supporting me.

Thank you to my friends, who have all been so understanding over the years.

Table of Contents

List of Figures

Chapter 1

Introduction

It is well known that aircraft experience significant aerodynamic interactions when flying close to the ground, ceiling, and/or walls. Ground effect manifests as an apparent increase in lift experienced as the aircraft approaches the ground. Close to the ground, the downward flow is slowed and forced to spread out radially as it encounters the ground. A similar increase in lift is experienced as an aircraft approaches a ceiling surface, known as ceiling effect, as illustrated in Fig. 1.1. While ground effect is experienced every day by full-scale manned aircraft, ceiling effect is not something that these aircraft encounter because they do not fly in enclosed spaces. Ceiling effect is largely unique to small-scale VTOL (Vertical Take-Off and Landing) aircraft that frequently operate and hover in interior spaces that have defined ceilings and walls.

Similar effects occur when flying close to walls and other large barriers / obstacles. Rotorcraft, in particular, are susceptible to these effects, especially while hovering or performing delicate low-speed maneuvers [34]. As with fixed-wing aircraft, rotorcraft can exhibit significant variations in control sensitivity and responsiveness when flying close to a large rigid surface. Any control input near these surfaces can result in unequal / disproportionate loading of the rotor disk. Such control complications make these surface

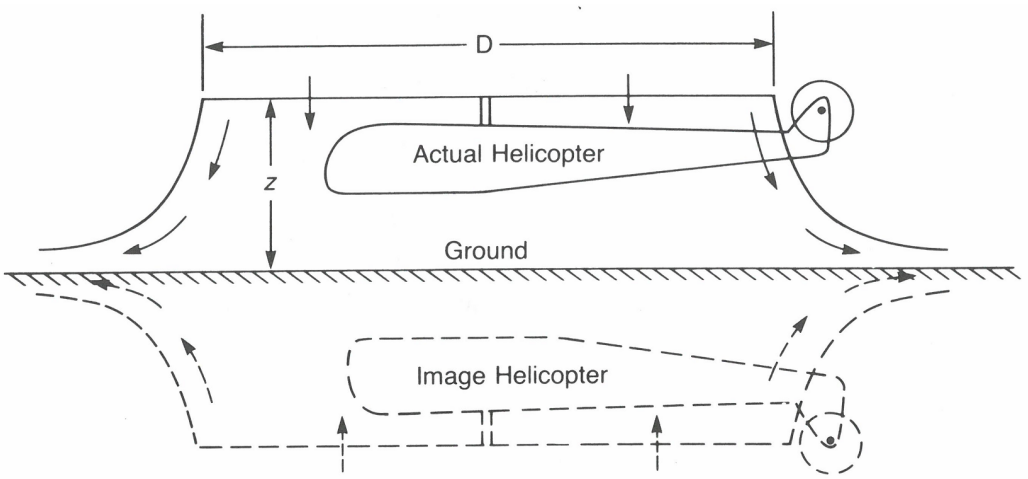

Figure 1.1: Ground effect diagram showing a mirrored image representing ceiling effect for conceptual clarification [34].

interactions of a particular interest in autonomous flight research. This work seeks to study and quantify ground, ceiling and wall effect in a comprehensive manner for small-scale multirotor aircraft in an effort to develop this improved flight controller in the future. Many UAV flight controllers deal with this problem by minimizing the time spent in these regions, and managing the multifaceted aerodynamic interactions as a generalized disturbance. This approach is somewhat crude, and if the application requires flying in close-quarter indoor environments, it is desirable to have a flight controller that includes model-based prediction of ground, ceiling and wall effect.

1.1 Motivation

The motivation for this work comes from a demand for highly-stable near-obstacle flight control systems for the purposes of observation, inspection, and analysis. In potential applications where precision hovering and close-quarter maneuvering are required, the ability to fly with utmost stability is a desirable asset. To accomplish this goal, it is necessary do accumulate a better understanding of the physical interactions that arise when flying very near to large rigid surfaces. Studying these phenomena through empirical evaluation using precision instrumentation under controlled conditions provides the necessary data to identify correlations and draw specific conclusions. The detailed experimental studies form the foundation for developing mathematical models to describe the effects that are experienced by an aircraft. The mathematical models must consist of a set of parameterized equations that can be applied to a variety of multirotor UAV designs. These parameters can include metrics such as rotor diameter, rotor spacing, number of rotors, etc. that are easily obtained by the end user and are specific to the aircraft of interest.

A set of parametric equations that can accurately describe the performance of multiple aircraft configurations near walls, ceilings, and the ground, allow for improved predictability of autonomous flight. Using this information, it is possible to incorporate an autonomous flight controller that can take advantage of a model-predictive approach. This will allow an autonomous UAV to anticipate the disturbances it will encounter as it approaches a wall, ceiling, or floor. Ultimately, this will lead to better stability when performing precision aerial inspections and repairs.

Other potential applications include:

- Detailed visual or sensory inspection of structures that are difficult to access (e.g. bridges, transmission towers, smoke stacks, etc.).

- Detailed exterior and interior investigation and inspection of damaged buildings (e.g. in an earthquake-ravaged building), to identify damage and hazards that could endanger human rescuers / workers.

- Increasing flight time of small-scale battery-powered multirotor UAVs by intentionally taking advantage of the added lift / efficiency in ground effect and/or ceiling effect (e.g. when navigating long corridors, tunnels, water mains, oil pipelines, etc.).

- Cobot UAV work teams operating in cluttered, disorderly or close-quarter indoor environments with their human counterparts close by; in which case, superior flight stability amongst numerous obstacles and surfaces is essential to avoid potential damage or injury to human counterparts.

1.2 Problem Statement

Research on ground effect for conventional full-scale helicopters dates back to the end of World War II and the development of the first generation of modern helicopters. For several decades, with the exception of a few experimental prototypes, the conventional helicopter (single main-rotor with a boom-mounted tail-rotor as shown in Fig. 1.2) was the only successful VTOL rotary-wing aircraft; and thus, this is the only configuration for which ground effect has been thoroughly studied.

Three notably successful designs that deviate from the conventional helicopter configuration are:

1. The tandem-rotor (e.g. Boeing CH-47 Chinook in Fig. 1.3a) that employs two counter-rotating main-rotors placed one behind the other, and does not use a tail-rotor. The two rotor disks overlap in the middle and therefore do not produce two discrete air streams like a pair of separated / isolated rotors would.

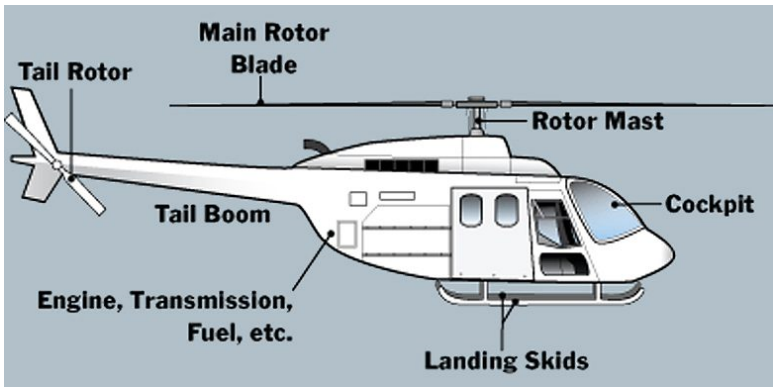

Figure 1.2: Illustration of the general configuration for a conventional helicopter design.

2. The coaxial-rotor (e.g. Russian Kamov Helicopters like the one in Fig. 1.3b) that uses two counter-rotating main-rotors stacked one on top of the other, and does not use a tail rotor. The two rotor disks completely overlap, effectively acting as a single more powerful rotor, but each one can operate at different speeds or with different collective pitch.

3. The tilt-rotor (e.g. Bell-Boeing V-22 Osprey in Fig. 1.3c) that combines the benefits of a helicopter and a fixed-wing airplane using two large wingtip rotors that can be tilted vertically or horizontally. This design is not strictly considered a helicopter, but is capable of VTOL operation using the same principles that are common to all rotary-wing aircraft. The two rotor disks do not overlap, but they are typically spaced less than one rotor-diameter apart with the wings and fuselage occupying most of the open area beneath them.

In recent years, the development of multirotor UAVs has given rise to a new family of successful rotary-wing VTOL aircraft. While all of the aircraft in Fig. 1.3 have more than one lifting rotor, we do not consider such aircraft "multirotors" in this dissertation. For the research presented in this dissertation, a multirotor is defined as a VTOL rotorcraft with

(a) Boeing CH-47 Chinook tandem-rotor helicopter

(b) Russian Kamov Ka-52 coaxial helicopter

(c) Bell-Boeing V-22 Osprey tilt-rotor aircraft

Figure 1.3: Notable examples of unconventional helicopter designs.

four, six or eight independently-driven lifting rotors arranged symmetrically in the rotor plane around the aircraft's center of gravity (*CG*).

Conventional helicopters are the proven standard for full-scale manned VTOL flight, but the design is much harder to apply on a small-scale autonomous aircraft due to the mechanical complexity and highly-coupled non-linear dynamics [2] and [1]. In contrast, the multirotor is mechanically and mathematically simple, and has come to dominate the small-scale UAV market. Because multirotors use multiple small motors to power each rotor, it is not practical for replacing the conventional helicopter in large-scale aircraft due to the scalability and power source limitations. Nevertheless, multirotors have become an important type of aircraft in commercial and scientific fields across the world, and researching how they behave is a worthy endeavor.

It is clear that the existing conventional helicopter ground effect model has been widely applied to multirotors, however it is based on assumptions that are only valid for conventional helicopters that use large rotors with uniform blades and variable pitch spinning at a constant speed. However, the assumptions are not valid for rotorcraft with fixed-pitch multipurpose propellers that spin at variable speeds. Additionally, multirotor propellers typically have a tapered airfoil that varies both the angle of attack and the cord length across the span of the blade from root to tip. There are so many notable differences in the way that multirotors function compared to conventional helicopters, and it is necessary to study how these compare and the result they have on aircraft behavior. Ground effect, while well understood for conventional helicopters, has never been studied in detail for multirotor aircraft. Many UAV researchers have mistakenly applied the standard helicopter ground effect model to small-scale multirotor UAVs without any verification of whether or not it's still accurate with so many differences in scale and design of the aircraft in question.

Ground effect must be studied in detail specifically as it applies to small-scale multirotors to identify key factors that are unique to multirotors and are not addressed by conven-

tional theory. Because of the many differences between helicopters and multirotors, it is necessary to provide extensive empirical data accompanied by mathematical formulation.

Ceiling effect is similar in principle to ground effect, and for a single rotor, both can be modeled using different forms of the same equation. Because ceiling effect can only occur when flying close to an overhead barrier, full-scale helicopters are never expected to encounter it, and therefore, there is very little published data on the subject. It is, however, expected that small UAVs will need to contend with ceiling effect in any number of different scenarios, making it a valid research question for multirotors. Ceiling effect must also be studied in similar detail, and with a similar experimental approach to determine how it differs from the study of ground effect.

The final piece of research that is required is a study of near-wall effects, which may occur in conjunction with ground effect or ceiling effect. Flying near vertical walls is not something that is limited to small UAVs, full-scale helicopters may also need to contend with this scenario, but there is still limited information available. Using the refined experimental methods that are applied to ground effect and ceiling effect, a detailed study of near-wall effect must be performed to formulate and validate a mathematical model.

1.3 Proposed Methodology

The proposed methodology for this dissertation involves using empirical data to formulate parametric mathematical models for multirotors in close-quarter flight near large obstacles.

- An instrumented test stand is constructed to isolate the aircraft test frame from surrounding obstructions.

- Mechanical and electronic methods are implemented to minimize measurement noise and errors.
- Testing procedures are developed to maintain conditional consistency and minimize uncertainty in temperature, power quality, and motor speed.
- Verification of the experimental method by means of comparison to existing theory is used to demonstrate the accuracy and reliability of the experimental setup.
- Extensive experimentation is conducted for each study (ground effect, ceiling effect, and near-wall effect) that isolates the aircraft test frame from uncontrolled variables and undesirable external influences.
- Experimental results are compared to existing theory for conventional helicopters, and the discrepancies are discussed in detail.
- The study results are computationally analyzed to develop equations that accurately describe the data.
- These equations are merged with existing aerodynamic theory for propellers and rotorcraft to develop parametric mathematical formulas that describe ground effect, ceiling effect, and wall effect in terms of basic aircraft and situational metrics.
- The parametric models can be incorporated in future development of model-predictive autonomous multirotor flight controllers that are uniquely suited to operating in close proximity to large obstacles.

1.4 Summary of Contributions

The primary contribution of this work is the formulation of parametric mathematical models to describe ground effect, ceiling effect, and wall effect specifically for small-scale multirotor aircraft. Furthermore, these equations are intended to be applicable to a wide variety of multirotors by incorporating basic parameters for aircraft dimensions and specifications. The secondary contribution of this work is the detailed presentation of empirical data that illustrates the general behavior of multirotor aircraft operating near walls, ceilings, and the ground. This data can provide UAV researchers with pure examples of multirotor performance in these various operational scenarios. The final contribution is the extensive documentation of the experimental process and how to overcome potential challenges, easing the burden on future researchers who may continue work on these topics.

The specific contributions of this work include the following:

- Experimental methods and procedures for evaluating aircraft performance near walls, ceilings, and the ground.
- Comprehensive empirical studies of ground, ceiling, and wall effect under controlled conditions for various quadrotor scales and configurations, as well as single isolated propellers, at multiple throttle levels.
- Detailed comparisons between multirotor empirical data and existing theory and research, including the classical models for helicopter ground effect.
- Empirical data indicating how rotor wake interactions affect multirotors differently than conventional helicopters in ground effect hover flight; and clear demonstration that the classical models for helicopter ground effect cannot be applied accurately to multirotor aircraft.

- Empirical results for single- and multirotor ceiling effect indicating no significant flow interactions occur between adjacent rotors upstream of the rotor disk; and clear demonstration that in ceiling effect, a multirotor acts like a single larger rotor, and therefore classical models for conventional helicopters can also be accurately applied for multirotor ceiling effect predictions.

- Multi-directional force-torque measurements of a multirotor hovering near a vertical wall at a wide range of separation distances and at various throttle levels; clear demonstration that the two components of wall effect act on the aircraft independently, showing that the pitching moment might exacerbate, but cannot be responsible for the horizontal attractive force that pulls the aircraft towards the wall.

- Development and validation of a parametric mathematical model of ground effect specifically for multirotor aircraft; requiring only basic physical measurements as inputs, remaining computationally lightweight, even for the small microcontrollers and embedded systems that operate most small-scale UAVs; and can be used in future development of enhanced autonomous flight controllers that can actively predict, and possibly exploit, ground effect for small-scale multirotors.

The research publications that have resulted from this work include the following:

- [10] S. A. Conyers, M. J. Rutherford and K. P. Valavanis. "An Empirical Evaluation of Ground Effect for Small-Scale Rotorcraft". In IEEE International Conference on Robotics and Automation (ICRA), May 2018. pp.1244-1250.
  DOI: 10.1109/ICRA.2018.8461035

- [9] S. A. Conyers, M. J. Rutherford and K. P. Valavanis. "An Empirical Evaluation of Ceiling Effect for Small-Scale Rotorcraft". In IEEE International Conference on Unmanned Aircraft Systems, June 2018. pp.243-249.
  DOI: 10.1109/ICUAS.2018.8453469

1.5 Organization of the Dissertation

The remainder of the dissertation is organized as follows:

Chapter 2 presents underlying aerodynamic theory, and a literature review of ground effect, ceiling effect, and wall effect studies as the apply to various rotorcraft, highlighting gaps in the existing literature that are addressed in this dissertation.

Chapter 3 presents the development of the experimental equipment and procedures, including the challenges that were encountered and how they were overcome. A validation of the experimental setup using existing theory is presented to demonstrate the accuracy and reliability of the results. The results of the multirotor ground effect study are presented with a discussion of how multiple rotors behave differently from existing helicopter theory.

Chapter 4 presents a validation of the ceiling effect experimental process, and the results of the ceiling effect study compared to existing theory derived from helicopter ground effect.

Chapter 5 presents the modification of the experimental setup for evaluating wall effect, and the additional challenges that arose. The results of the wall effect study are presented, with a discussion of the variables at play and how they influence near-wall behavior.

Chapter 6 describes the remaining research questions that must be answered to complete the remainder of this research process. A proposed step-by-step procedure for completing the remaining research tasks is presented with a detailed timeline.

Chapter 2

Background & Literature Review

This chapter discusses some of the fundamental knowledge surrounding propeller operation in open air, as well as near rigid surfaces such as ceilings, vertical walls, and the ground. Historical and contemporary research on the primary topics of ground, ceiling and near-wall effect are presented in this chapter, along with a comparison to the research presented in this dissertation. Beginning with the background theory of propeller operation, dating back almost two centuries, this provides the fundamental evidence of the fluid interactions that are observed in this dissertation. This is followed by the background theory of ground effect that goes back to 1957, and is still scientifically relevant. Further insight is provided by detailing the theories and related research specific to ground effect, which is explored in particular depth. Ceiling effect, being conceptually similar to ground effect, is described next. Finally, theory and related work of near wall effect completes this chapter.

2.1 Background of Propeller Theory

The underlying mathematics that describe propeller function and thrust generation dates back centuries. Modern propeller theory can be traced back to 1865 with the work of Rankine [35], [40], and [30], who recognized that a propeller generates thrust as a reaction to accelerating a mass of air in the opposite direction (Newton's 3rd Law of Motion). Eventually, this led to what is now known as *Momentum Theory*, and is one of the most widely accepted methods for describing propellers. Momentum Theory is based on the assumptions that a stationary propeller in a moving air stream can be represented as an infinitely thin disk of diameter D across which the pressure increases discontinuously, and the stream velocity far ahead of the propeller (V_o) and far behind the propeller ($V_o + \omega$) is uniform, shown in Fig. 2.1. Additionally, the static pressure is assumed to be constant and equal to the free-stream pressure. It is important to recognize that under these conditions, the cross-section of the flow in the ultimate wake of the propeller is smaller than the disk area of the propeller. This theory is computationally simple for estimating basic quantities such as thrust (T), power (P), efficiency, and the propeller induced velocity (ω) as shown by equations (2.1), (2.2), and (2.3). It is clear that the maximum thrust occurs when the stream velocity $V_o = 0$ (static thrust), which is the assumed case for (2.3).

When applied to a lifting rotor, Momentum Theory can provide valuable insight into aircraft behavior in different flight cases and provide an estimate of induced velocity. Fig. 2.2 graphically illustrates the momentum theory solution for induced velocity for helicopters, according to [24]. It should be noted that momentum theory cannot provide a realistic solution in the second quadrant of the graph, however, these flight conditions do actually exist.

Momentum Theory offers computational simplicity for basic propeller analysis; however, it does not take into account the actual propeller geometry (pitch, airfoil, number of

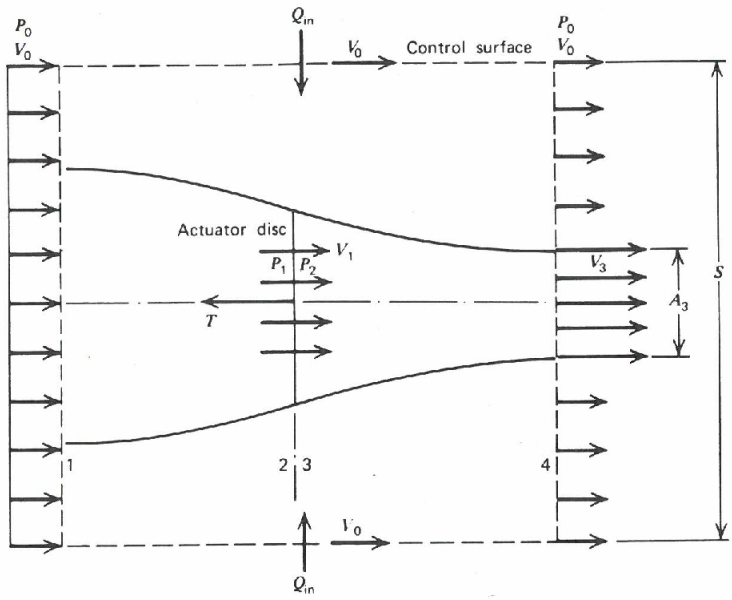

Figure 2.1: Idealized flow diagram for classical Momentum Theory [30].

blades, etc.), nor the fact that the propeller induces both angular and axial velocity components to the air stream. To address these limitations, Stefan Drzewiecki published a theory in 1909 based on the opposite approach of a rotating blade element advancing axially through stationary air [40] and [30]. This so-called *Blade Element Theory* often combines pieces of Momentum Theory to provide a more complete description of propeller performance, sometimes called *Blade Element Momentum Theory*.

In the same manner as the linear motion of a fixed-wing, the rotating airfoil of a propeller blade generates aerodynamic lift and drag, which ultimately determine the thrust and required torque. More recently however, it became evident that the vortices observed in the wake of a moving airfoil were the result of bound circulation around the airfoil, and directly related to the production of lift. Likewise, this bound circulation occurs around the blades of a propeller and thus, directly relates to thrust. *Vortex Theory* [30] and [29] quantifies this bound circulation (Γ) and ultimately provides a numerical method for directly calculating the induced velocity (ω) in terms of axial (ω_a) and tangential (ω_t) components using (2.4)

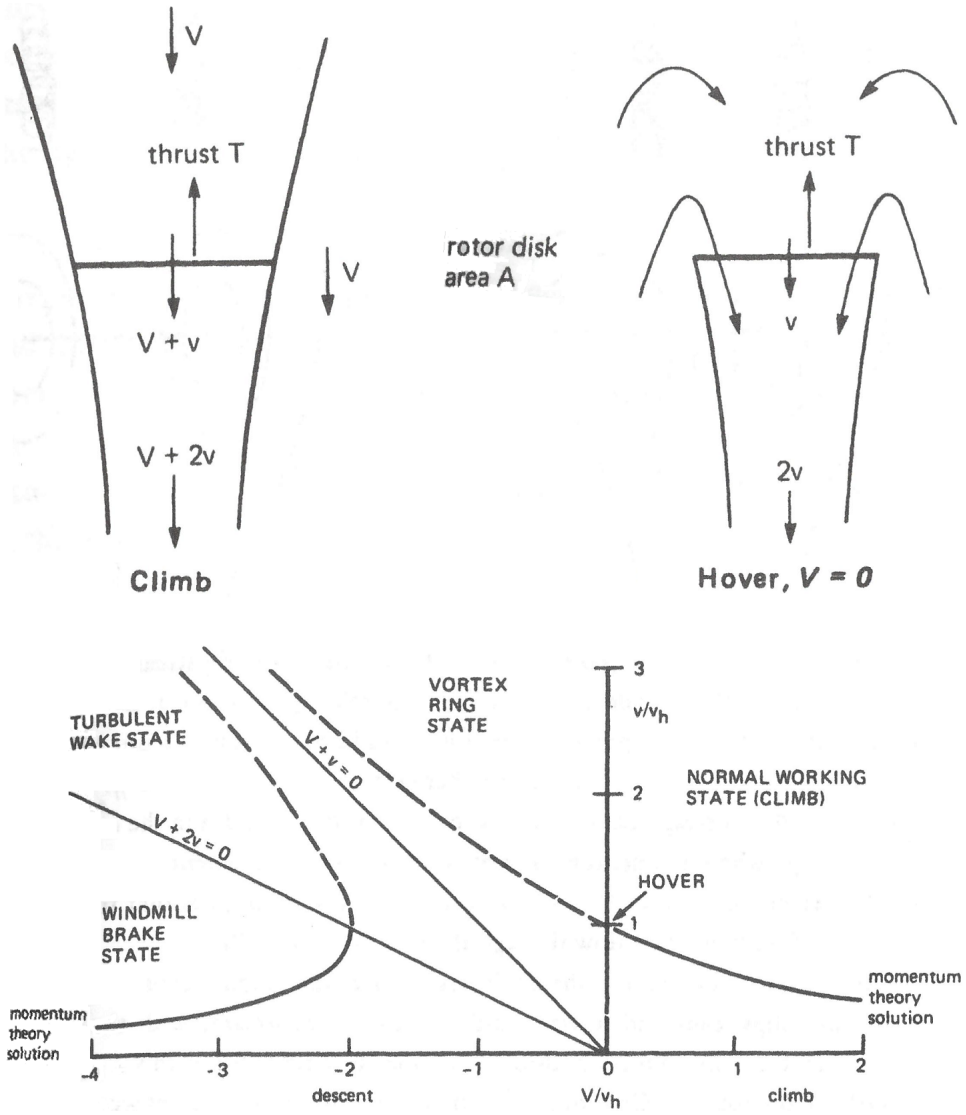

Figure 2.2: Illustration of the flow through a rotor disk in two levels of a vortex ring state [24].

as demonstrated by [16], where α_i is the induced angle of attack. Combined, these three theories form a complete mathematical description of propellers.

$$T = 2\rho A\omega(V_o + \omega) \tag{2.1}$$

$$P = 2\rho A\omega(V_o + \omega)^2 \tag{2.2}$$

$$\omega = \sqrt{\frac{T}{2\rho A}} = \frac{P}{T} \tag{2.3}$$

$$\omega_t = V_R\alpha_i \sin(\phi + \alpha_i) \quad and \quad \omega_a = V_R\alpha_i \cos(\phi + \alpha_i) \tag{2.4}$$

2.2 Ground Effect Theory for Conventional Helicopters

It is well known that aircraft experience significant aerodynamic interactions when flying close to the ground. Ground effect manifests as an apparent increase in lift experienced as the aircraft approaches the ground. Ground effect for helicopters can be described as the increase in main rotor lift per unit power (this ratio is called power loading) experienced when flying close to the ground. The increase in power loading is inversely proportional to the aircraft's height above the ground, and is generally insignificant at heights greater than twice the effective rotor diameter. Ultimately, ground effect is the result of a reduction in the induced velocity from the rotor when flying close to the ground, as illustrated in Figs. 2.3 and 2.4. When high above the ground, the induced velocity is higher because the downward airflow is unobstructed. Close to the ground, the downward flow is slowed and forced to spread out radially as it encounters the ground. According to Blade Element Momentum Theory, thrust is inversely proportional to induced velocity, explaining the apparent increase in thrust in ground effect.

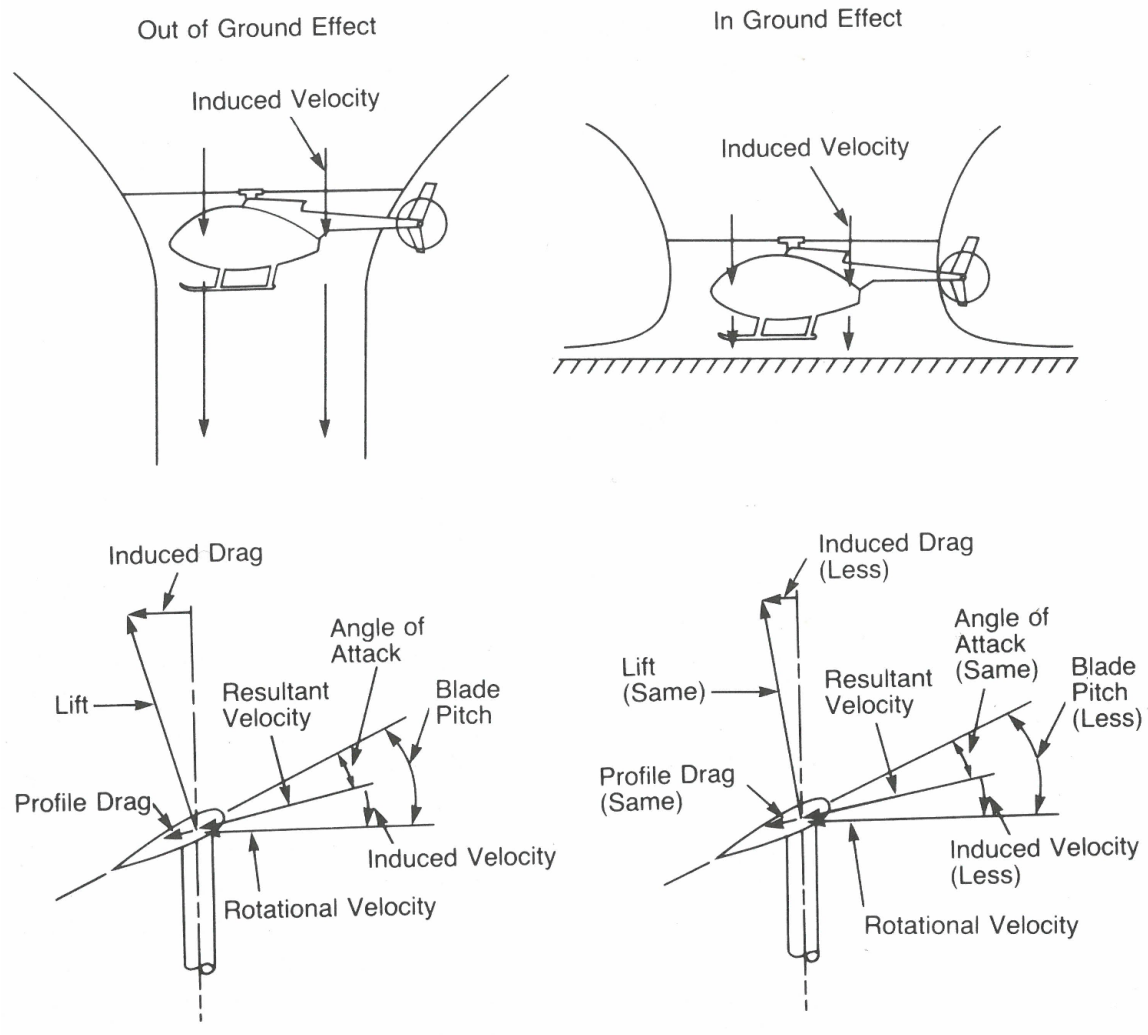

Figure 2.3: Ground effect according to Blade Element Theory [34].

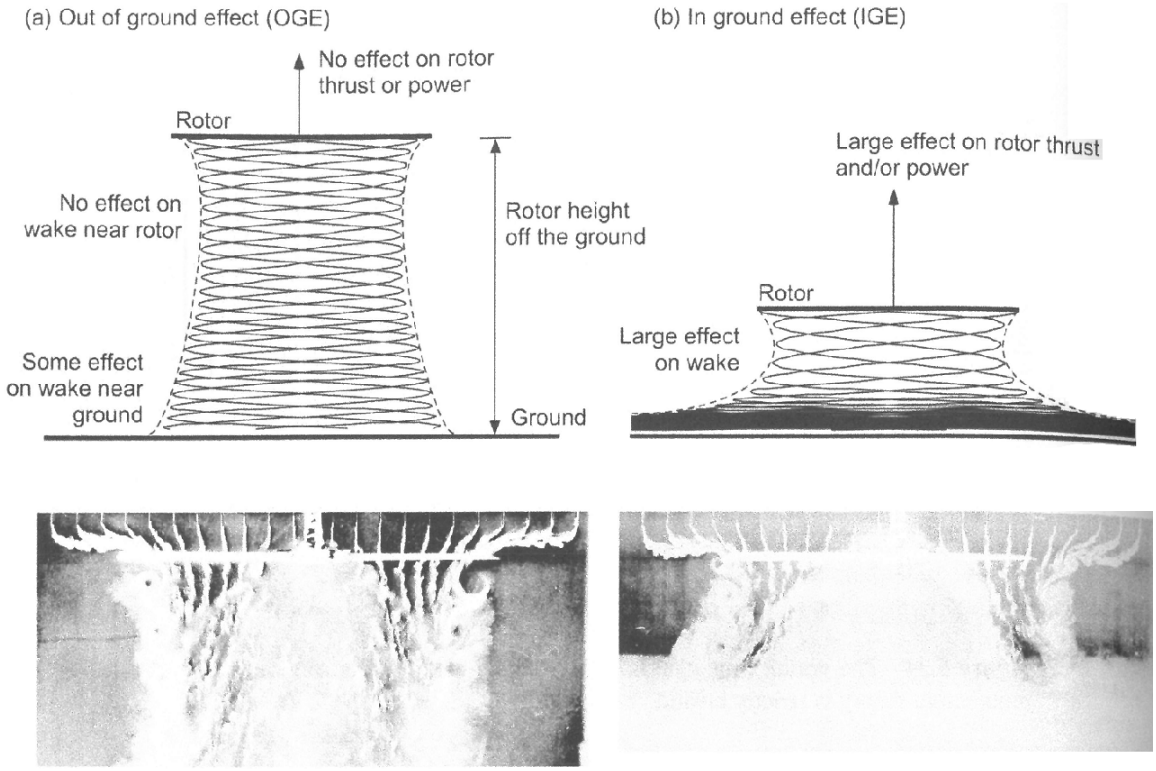

Figure 2.4: Illustrations and smoke-trail photos of the spirialing rotor downwash in OGE and IGE scenarios. [27].

Similar effects occur when flying close to ceilings, walls, and other large barriers / obstacles. Rotorcraft, in particular, are susceptible to these effects, especially while hovering or performing delicate low-speed maneuvers [34]. As with fixed-wings, rotorcraft can exhibit significant variations in control sensitivity and responsiveness during takeoff and landing because of ground effect. Any roll or pitch corrections near the ground can result in unequal and disproportionate loading of the rotor disk due to one side being closer to the ground than the opposite side. In other words, ground effect can create instability by changing the aircraft's response to a given control input. Additionally, maintaining a constant rate of ascent / decent is more difficult near the ground because the power loading is variable. Many UAV flight controllers ignore these problems, treating ground effect like any other disturbance and intentionally minimizing the time spent in immediate proximity to the ground during takeoff and landing. It is desirable to develop an improved flight controller that includes model-based prediction of ground effect, as well as near-wall and near-ceiling effects. This work seeks to study and quantify ground effect in a comprehensive manner for multirotor aircraft in an effort to develop this improved flight controller in the future.

2.2.1 Cheeseman-Bennett Model

Conventional helicopter ground effect has been well studied since the 1950s, with the most widely accepted mathematical model published by Cheeseman and Bennett in 1957 [8]. The Cheeseman-Bennett model [8] is most commonly defined by the equation in the form of (2.5) which provides a relationship between the radius (R) of the propeller, the height above the ground (Z), the thrust generated by the rotor while operating far from the ground (T_{OGE}), and the apparent increase in thrust experienced close to the ground (T_{IGE}).

However, this model assumes a single variable-pitch rotor turning at a constant speed using constant engine power.

$$\frac{T_{IGE}}{T_{OGE}} = \frac{1}{1 - \left(\frac{R}{4Z}\right)^2} \qquad iff \qquad \frac{Z}{R} > 0.25 \tag{2.5}$$

The Cheeseman-Bennett model employs the single equation and boundary condition in (2.5) to conveniently calculate the ratio of the lift experienced while hovering in-ground-effect (IGE) and out-of-ground-effect (OGE). Because the equation only requires two basic measurements to predict the ground effect, it has been widely utilized. Other studies of the era [25], [43] validate the Cheeseman-Bennet equation (2.5) using experimental data to focus on a change in thrust approach. This equation assumes that the main rotor speed and power output both remain constant in IGE and OGE flight. These assumptions may be reasonable for helicopters, but they are inherently impossible for multirotors that are continuously varying the rotor speeds to generate control authority.

It is clear that (2.5) from the Cheeseman-Bennett model has been widely used, however it is based on assumptions that are only valid for conventional helicopters that use large rotors with uniform blades and variable pitch spinning at a constant speed. However, the assumptions are not valid for rotorcraft with fixed-pitch multipurpose propellers that spin at variable speeds. Additionally, these propellers typically have a tapered airfoil that varies both the angle of attack and the cord length across the span of the blade. These fundamental differences in aircraft design suggest a possible disconnect when attempting to apply conventional helicopter ground effect models to another rotorcraft such as a multirotor.

2.2.2 Hayden Model

An alternative model is presented in [34] and [21] that describes the decrease in power consumption seen in the IGE case using (2.6), rather than the increase in thrust. Equation

(2.6) is for power measured in HP units only, but it can be reduced to the dimensionless ratio form in (2.7). Assuming that the power required during OGE hover (P_{OGE}) can be measured directly, the power required during IGE hover (P_{IGE}) can be calculated using equation (2.7) . The induced velocities at constant thrust ω_{IGE} and ω_{OGE} can be calculated using an equation such as (2.3), experimentally determined, or from results of previous published experiments such as [34], [21] and [4].

This model, commonly referred to as the "Hayden" model, is equally useful in predicting ground effect performance, and it is not limited by assuming constant power and speed. A comparison of the ground effect predictions using (2.5) and (2.7) are shown in Fig. 2.5, along with some experimental helicopter flight data. Instead, this model assumes a constant thrust condition in both OGE and IGE cases. This assumption is easy to apply to any electric powered aircraft, because the aircraft weight is equal to the overall downward thrust during hover. Because electric aircraft do not consume fuel during flight, their weight remains constant. Therefore, the constant thrust assumption holds true during hover if the minor thrust variations due to attitude corrections average out over any non-zero length of time.

$$\Delta HP = \frac{Tv_{1OGE}}{550}\left[1 - \left(\frac{\omega_{IGE}}{\omega_{OGE}}\right)\right] \tag{2.6}$$

$$P_{IGE} = P_{OGE}\left(\frac{\omega_{IGE}}{\omega_{OGE}}\right) \tag{2.7}$$

2.3 Ground Effect Research

In the two decades after [8] was published, researchers had already noticed several factors that could influence the ground effect predictions. The work published in [19] and [15] present evidence that bench tests using an isolated rotor could not recreate the ground

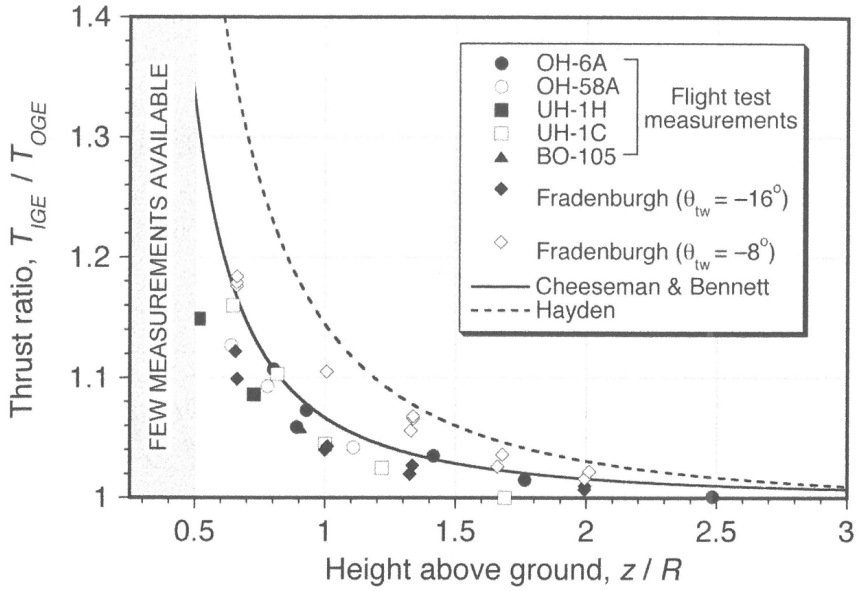

Figure 2.5: Comparison of Cheeseman-Bennett and Hayden ground effect models, with additional helicopter flight test data [27].

effect performance increase that was seen in full scale flight tests. A helicopter in flight benefits more from ground effect due to the decreased download on the airframe/fuselage that is directly beneath the rotor. A bench test however, does not experience this benefit, and thus the results will produce lower T_{IGE} values under similar conditions. Equation (2.5) also does not account for the lift loading or the number of rotor blades. This means that a smaller propeller with greater pitch is capable of producing the same thrust under the same conditions as a larger propeller, but (2.5) cannot account for this. Therefore, the equation can overestimate T_{IGE} for a large rotor with low lift loading, and underestimate T_{IGE} for a small rotor with high lift loading.

2.3.1 Ground Effect Research for UAVs and Multirotors

It is clear that (2.5) from the Cheeseman-Bennett model has been widely used, however it is based on assumptions that are not valid for multirotor aircraft. These fundamental differences in aircraft design suggest a possible disconnect when attempting to apply conven-

tional helicopter ground effect models to another rotorcraft such as a multirotor. Additional variables such as changing rotor speeds, number of rotors, rotor placement (e.g. different spacing and angles between rotor supports), dihedral, and possibly ducted/shrouded rotors can all apply to multirotors and their influence on ground effect is not well studied.

Recent work from G. M. Eberhart, et al. in [14], [13] and [12] focuses on developing a numerical method for predicting the thrust and power consumption in ground effect. The authors make use of classical propeller aerodynamic theory to develop a ground effect model based on *Blade Element Momentum Theory* (BEMT) to model OGE performance for a single 11×7 composite propeller. The BEMT OGE model is combined with the Cheeseman-Bennett predictions for IGE performance based on (2.5). The resulting model provides a purely analytical method for modeling the ground effect performance of a specific propeller geometry as a function of the height-ratio Z/R. The advantage of this model is that it does not require any empirical measurement of OGE baseline propeller performance, as is required when using (2.5) alone to model ground effect. The authors present a basic empirical validation of the BEMT model for the specific propeller geometry that was chosen.

The work presented in [14], [13] and [12] provides a valid method of characterizing the performance of a specific propeller in OGE and IGE conditions without requiring any actual hardware or experimentation. The authors have produced one of the most comprehensive investigations to date of ground effect for small-scale rotorcraft, but although they frequently discuss applying of their BEMT-GE model to multirotor aircraft, their methods do not explore potential interactions between multiple adjacent rotors, and therefore this is still only a single-rotor model, not a true multirotor-specific model. The BEMT-GE model presented by G. M. Eberhart, et al. has one significant drawback, it requires extensive knowledge of a specific propeller design (airfoil geometry, twist/pitch, cord taper, etc.) that is not be easy to obtain from typical RC parts suppliers, and exceedingly difficult to mea-

sure without specialized instrumentation. This leads to inherent difficulties when evaluating multiple different motor / propeller combinations or varying throttle / RPM levels, which are key steps in the process of developing and evaluating aircraft performance, efficiency, and stability.

A few attempts have been made to comprehensively model ground-effect in multirotors, but do not address the overarching assumptions used to simplify the problem [33] and [37]. The gradual shift from conventional helicopter UAVs to multirotor UAVs, has led some researchers to study ground effect on multirotor platforms using (2.5) from the Cheeseman-Bennett model. In the work of [5], the ground effect on a typical quadrotor is considered using (2.5) for the purpose of modeling and control development, a goal that is shared by many UAV researchers. The work presented in [33] goes into greater detail using experimental data and theory to describe the effect on a *KMel Robotics kQuadNano* micro-quadrotor flying close to the ground and the ceiling. The experimental testing is performed in hover flight within a motion-capture system, and the T_{IGE} measurements are taken indirectly using the average rotor tip speed at each height. This work presents actual flight data, however, the indirect method of measurement introduces the potential for large errors and limited accuracy.

The work presented in [22] takes a different approach to estimating ground effect by augmenting the Cheeseman-Bennett equation with flow field measurements of rotor downwash. This work focuses exclusively on conventional helicopter UAVs, but no specific aircraft is mentioned because no physical experimentation is performed, only simulation results are presented. The authors expand radially outward from the Cheeseman-Bennett equation using ring sources to create an improved uniform spatial distribution of the flow field. This work presents a strong combination of fluid mechanics, analytics, and control development techniques, but does not offer any empirical data or hardware-in-the-loop testing. This work also does not present any plots of ground effect thrust ratio, making

their results difficult to verify and compare to others. The authors make extensive use of computational tools and aerodynamic theory to predict ground effect, but do not offer any numerical solution methods or discussion of applications for multirotors.

Building upon [5], [33] and [6], the work presented in [37] uses (2.5) to evaluate the ground effect on a *Draganflyer X8* octorotor that features four coaxial pairs of propellers. This work treats each coaxial pair as a single rotor based on Blade Element Momentum Theory, therefore equating the aircraft to a quadrotor. The claim that the ground effect for a quadrotor can modeled by (2.5) as four single rotors summed together is shown to be inaccurate by the results presented below. This work also uses a test stand to isolate one coaxial pair of rotors and evaluate them before conducting flight tests. Because only a single (coaxial pair) rotor is evaluated, the authors fail to address how possible interactions between multiple flow streams may affect ground effect performance. This work does not directly measure T_{IGE}, but rather assumes it to be equal to the aircraft takeoff weight. Additionally, this work does not directly measure the rotor power, but rather assumes that the power at a given RPM is constant in both OGE and IGE cases.

Recent work published in [20] aims to capitalize on the reduced power consumption associated with flying in ground and ceiling effect by developing a real-time path planning methodology which intentionally keeps the aircraft near a floor or ceiling. To accomplish this, the authors develop methods for detecting and identifying floors and ceilings autonomously while in flight using the mid-scale *AscTec Hummingbird* quadrotor (54 cm diagonal span with 20 cm propellers). The authors also perform empirical studies with this aircraft using a motion-capture system and telemetry for throttle level and power consumption to indirectly measure ground and ceiling effects. They present results that are generally in agreement with the work presented later in Chapters 3 and 4, but their data is not as complete or comprehensive. Their plots of ground effect show the observed T_{IGE} to be significantly greater than the Cheeseman-Bennett predictions using (2.5) in the mid-

range height ratio region. These findings are consistent with those in our ground effect study presented later in Chapter 3, but the authors of [20] do not explore the extremely low height ratios that this dissertation discusses in detail.

Perhaps the most significant contribution made by [20] is the flow field visualization around a quadrotor in both ground and ceiling effect. Because of the enormous complexity of creating a CFD model of a complete multirotor in hover, no such work has been published thus far, and detailed flow visualization has remained largely out of reach. Instead of simulation, the authors of [20] employ stereoscopic Particle Image Velocimetry (PIV) to directly capture the flow field around a quadrotor. The PIV studies are performed with a micro-scale *Crazyflie* UAV (9.2 cm diagonal span with 4.6 cm propellers) suspended from a rigid instrumented test frame that measures thrust in various IGE, ICE and free-flight conditions. Because PIV technology has a limited field field of view, the flow fields can only be captured using a very small aircraft. The authors claim that the T_{IGE}/T_{OGE} ratio can be scaled to the larger UAV without considering the dramatically different Reynolds number regime that occurs with a $\approx$600% dimensional scaling. The ground and ceiling effect conditions are reproduced by placing large acrylic sheets above or below the aircraft on the test frame. Although the measured thrust data in the micro-scale UAV experiments is not directly presented in the paper, the PIV flow field visualization, shown in Figs. 2.6 and 2.7 provide valuable insight into the airflow patterns around a multirotor aircraft.

The topic of ground effect for small-scale UAVs has captured the attention of many researchers working in this field, with the majority of them focusing on how to improve flight control stability in and around the ground effect region of influence. Recently, more researchers are motivated to intentionally take advantage of ground effect to extend the limited flight times of small-scale UAVs by reducing power consumption. The overwhelming majority of published research on this topic shows a tendency to simply accept that the classical Cheeseman-Bennett theory is applicable to small-scale multirotors, often with no

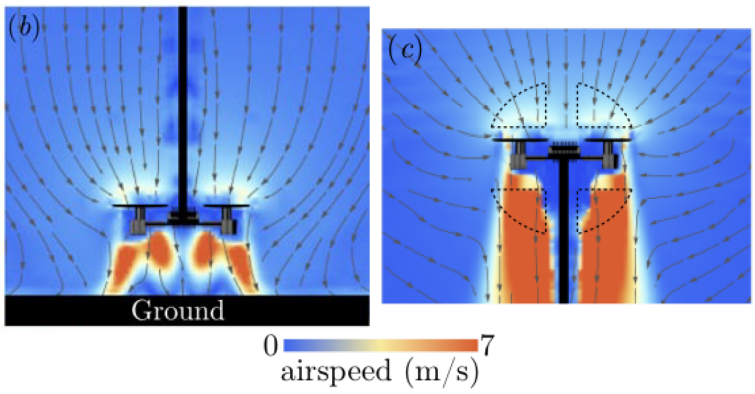

Figure 2.6: PIV measured flow fields surrounding a micro-scale quadrotor in IGE and OGE flight conditions [20].

consideration given to the important differences in the mechanics, physics and dimensional scale. Despite the interest in UAV ground effect, there has been surprisingly little work or discussion about whether or not the classical model defined in (2.5) actually holds true for small-scale multirotors. This dissertation aims to demonstrate that ground effect for small-scale multirotor aircraft cannot be accurately described using conventional ground effect theories such as (2.5). Multiple factors can have a dramatic effect on hover performance near the ground, and in many cases this effect is contrary to the predictions made by the existing conventional models.

2.4 Background of Ceiling Effect Theory

Ceiling effect is fundamentally similar to ground effect because it arises from the same physical processes, and for the single-rotor case, the same equation (2.8) can be used to describe both scenarios. When a rotorcraft is in-ceiling-effect (ICE) there is a reduction in the induced velocity from the rotor(s) due to the airflow obstruction that results in a greater pressure difference across the rotor disk. This can envisioned simply as a rotorcraft being sucked up into the ceiling when it gets too close. In a real-world scenario, this would also

result in a decrease in drag on the rotor(s) which causes them to spin faster, and produce even more thrust. The assumptions of (2.8) however, require a constant rotor speed and power output. The experimental results presented in this paper use a closed-loop speed controller to ensure these assumptions are met, thus allowing a direct application of (2.8).

$$\frac{T_{IGE}}{T_{OGE}} = \frac{T_{ICE}}{T_{OCE}} = \frac{1}{1 - \left(\frac{R}{4Z}\right)^2} \qquad iff \qquad \frac{Z}{R} > 0.25 \tag{2.8}$$

When considering ground effect, the airflow downstream of the propeller is columnated and directional, and is ultimately responsible for the observed interactions between multiple adjacent propellers in the multirotor ground effect studies presented in [10]. Conversely, for ceiling effect the airflow upstream of the propeller is disorganized by comparison, with very little directional flow until immediately above the propeller disk. Because ceiling effect results from flow phenomena upstream of the propeller, it is reasonable to assume very little interaction will occur between the adjacent propellers of a multirotor UAV. This suggests the ICE hover performance of a multirotor can also be accurately predicted using (2.8). This paper aims to determine whether or not this assumption is valid (i.e. can (2.8) be directly applied to multirotors with equivalent accuracy). A greater understanding of ceiling, ground, and wall effects will ultimately facilitate the development of an improved flight controller that can provide improved stability in enclosed spaces using a model-predictive approach.

2.5 Ceiling Effect Research

There have been few attempts to evaluate ceiling effect in small-scale multirotor UAVs. The work presented in [36] is the first known example of an experimental evaluation of ground and ceiling effect for a single 324 mm propeller. The experimental testing per-

formed at NASA Ames Research Center explored a variety of distances, propeller speeds, and environmental conditions. The authors present a detailed mathematical analysis of the fluid mechanics surrounding the propeller, and attempt to directly calculate the thrust in each test case. The authors also present a similar analysis of ground effect and the comparison between the two. Overall, [36] is one of the most comprehensive studies to date for both ground and ceiling effect, however, only a single isolated propeller is evaluated. In this research, various quadrotor configurations are explored in addition to a single propeller case for the purposes of determining if (2.8) can be applied to multirotor UAVs to predict ceiling effect. Using a highly-refined experimental method with sophisticated control and data acquisition equipment, the results presented below provide a comprehensive evaluation of ceiling effect for quadrotors of different sizes.

The work presented in [33] attempts to measure both ground and ceiling effect using for the very small KMel Robotics kQuadNano. The experimental testing is performed in hover flight within a motion-capture system, and the T_{ICE} measurements are taken indirectly using the average rotor tip speed at each height. According to Blade Element Theory, the thrust of a rotor increases proportionally to the square of the angular velocity, making it possible to estimate T_{ICE} assuming T_{OCE} is equal to the aircraft takeoff weight. While the results in [33] do not closely match the theory, it is the only such example of evaluating ceiling effect in actual flight tests.

Previous work described in [31] attempts to experimentally evaluate and model ceiling effect performance for a multirotor UAV designed for bridge inspection. The authors focus on taking advantage of ceiling effect to operate a shrouded quadrotor in direct contact with the underside of a bridge. By utilizing ceiling effect in this way, the UAV can operate with extended flight times by expending less energy to remain airborne. This is an example how an improved understanding of close-quarter flight near a surface can provide a practical advantage, and improve the usability and versatility of small-scale multirotors. This

work uses a basic instrumented test stand with a single DOF to perform an experimental evaluation of a single quadrotor configuration at varying distances from a ceiling surface analogue. However, this work fell short of achieving agreement between the experimental results and the theory, and arbitrary correction factors were inserted into a rewritten form of (2.8). An open-loop speed controller is used, allowing the propellers to spin faster while in the ceiling effect region, and is inconsistent with the constant speed/power assumptions required for (2.8). With these correction factors, the rewritten equation differs significantly from (2.8), and thus, somewhat invalidate the predicted ceiling effect performance. Additionally, the correction factors must be experimentally determined specifically for each UAV, making this method impractical for the UAV industry and the scientific community seeking to advance autonomy. The ceiling effect results presented below need no such modification, as the experimental data and the mathematical predictions are in agreement. This can be attributed to the highly refined experimental apparatus and data collection techniques that are used.

As discussed in Section 2.3, recent work published in [20] aims to capitalize on the reduced power consumption associated with flying in ground and ceiling effect by developing a real-time path planning methodology which intentionally keeps the aircraft near a floor or ceiling. They present results that are generally in agreement with the work presented later in Chapters 3 and 4, but their data is not as complete or comprehensive. The authors observe that the measured T_{ICE} is noticeably over-predicted by the model using (2.8) at very low height ratios, but otherwise the curves are similar. The results presented later in Chapter 4 show a similar divergence from the theory in this region, but to a lesser degree. Because of the inaccuracies that are inherent with the indirect motion-capture measurements, especially when flying very close to the ceiling where the cameras might have more difficulty tracking, it is reasonable to assume that measurement error would be most pronounced in this sensitive region.

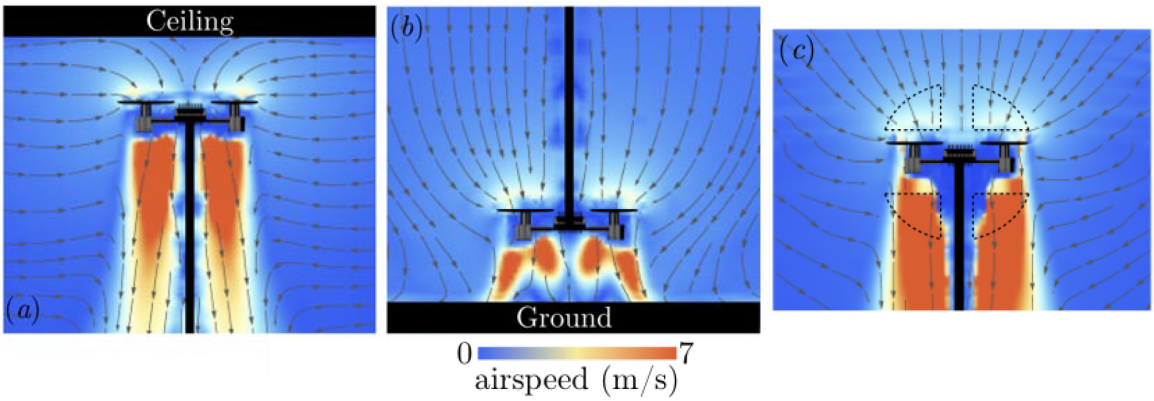

Figure 2.7: PIV measured flow fields surrounding a micro-scale quadrotor in ICE, IGE and OGE flight conditions [20].

The T_{ICE} measurements in [20] for the mid-scale *AscTec Hummingbird* are largely unremarkable compared to the PIV flow field visualization around the micro-scale *Crazyflie* UAV. Instead of attempting to simulate or simplify the flow fields, the authors employ stereoscopic Particle Image Velocimetry (PIV) to directly capture the flow field around a quadrotor. As mentioned previously, the limited field field of view of the PIV system requires the authors to use a much smaller aircraft than in their other experiments. Although this UAV is unusually small compared to what is commonly used by UAV researchers, the flow field patterns should be very similar for a larger scale multirotor. The PIV flow field visualization in free flight, ICE and IGE conditions are shown in Fig. 2.7. The images clearly illustrate the differences in the aerodynamic mechanisms of ceiling effect versus ground effect.

2.6 Wall Effect Research

Wall effect for rotorcraft occurs when hovering in close proximity to any large vertical surface, and causes the aircraft to be unexpectedly "sucked" towards the wall. The risks of flying too close to a wall are generally understood by UAV operators as being

something that should be avoided, but very few researchers have attempted to study and characterize the effect of a vertical wall on a nearby hovering rotorcraft. The generalized behavior of an aircraft in this situation has been observed by many UAV operators as a pitching moment that forces the aircraft to accelerate towards the wall. The magnitude of the pitching moment increases rapidly as the aircraft gets closer to the wall leading to feedback effect can result in an unavoidable collision. Even with state-of-the-art flight controllers, wall effect is very difficult to compensate for when close to a wall because a small change in distance can have a large influence on the aircraft that overwhelms the otherwise stable control response to normal transient disturbances. Understanding the fundamental physical interactions the are responsible for producing wall effect is essential to developing improved flight control methods for stable autonomous flight near walls and vertical obstacles.

The work in [11] makes use of Computational Fluid Dynamics (CFD) to model the aerodynamic interaction between a hovering UAV and a vertical wall at various separation distances. The analysis of Fluid-Solid Interaction (FSI) uses a three-dimensional mesh that encompasses the rotating cylindrical near-field region around the rotor, and the stationary far-field up to a distance of $15D$. The aircraft that is modeled in simulation is a *Blade Nano CPX* small-scale conventional helicopter with a main rotor diameter (D) of 20.6 cm (8.1 inches) and an operating speed of 3200 rpm. This publication focuses exclusively on computational modeling and simulation to study wall effect, and does not present any empirical data. Nonetheless, the computational analysis is very elaborate and comprehensive given the difficulties associated with this type of problem.

The results presented in [11] are free from the uncontrolled external influences that are unavoidable in empirical studies, and offer valuable insight into the fluid mechanics of a lifting rotor operating next to a vertical wall. Additionally, the contour plots such as those shown in Fig. 2.8 provide useful flow visualization that cannot be duplicated in real-world

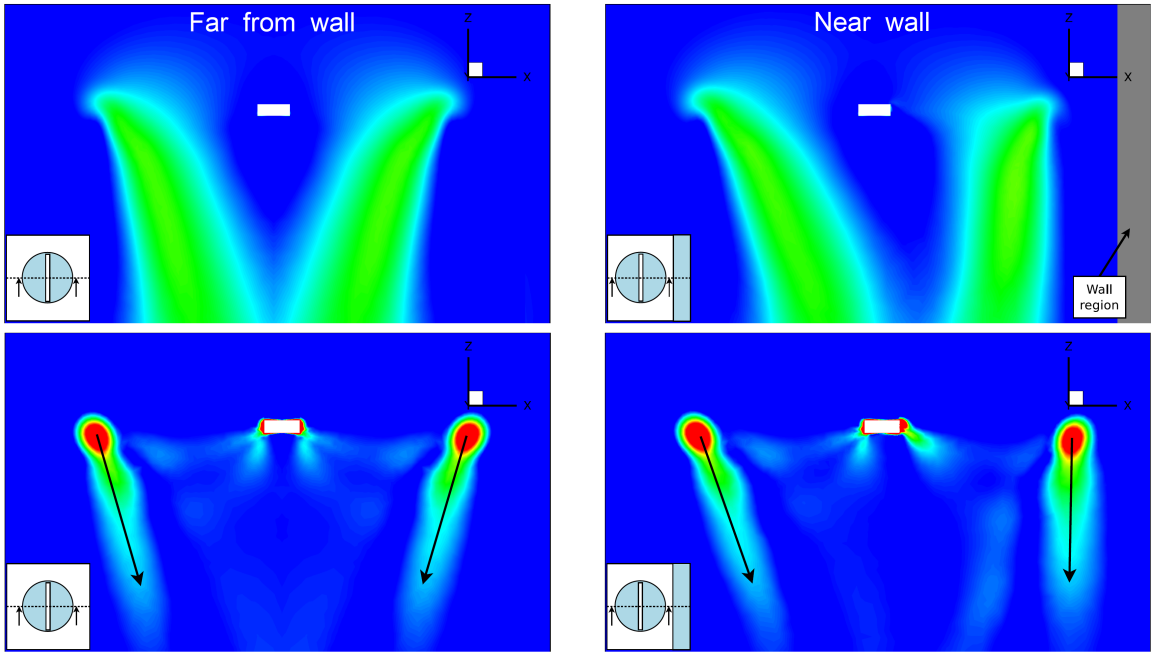

Figure 2.8: CFD contour plots illustrating how wall effect alters flow velocity (top) and vorticity (bottom) downstream of a single lifting rotor [11].

experiments. The results quantify the forces acting on the rotor blades due to the lift imbalance created by the wall, and the pitching / rolling moments on the rotor disk that ultimately influence the aircraft. Because the analysis does not allow any change in the relative position and orientation of the rotor disk, the data is comparable to the studies presented in this dissertation using a fixed rigid test stand. While this work does not consider multirotor aircraft, the small main rotor of the helicopter is very similar in scale to the propellers used on many multirotor UAVs, making the results more comparable to the work presented in this dissertation. As with ground effect, the downstream interactions between the adjacent propellers of a multirotor are likely to influence near-wall flight behavior differently from a single rotor. This type of comprehensive wall effect study is a research topic that remains unexplored for multirotor aircraft, and is a central component of this dissertation.

Developing an autonomous flight controller that can effectively compensate for wall effect is a goal shared by many UAV researchers. The work presented in [26] describes

the development of an adaptive quadrotor flight controller that is specifically designed for near-wall stability. A neural-network-based control approach is used to compensate for variable external disturbances, specifically ground effect and wall effect. Because there is so little published research on wall effect for small-scale rotorcraft, there is no established parametric model (i.e. an equation analogous to (2.5)) for predicting the magnitude of the disturbances caused by the wall. Rather than attempting to characterize wall effect in terms of physical metrics, the authors treat it as a arbitrary external disturbance based on the generalized equations of motion for a quadrotor. Because these disturbances could be the result of other external influences, not necessarily due to wall effect, the proposed controller does not represent a significant breakthrough in wall effect research. Additionally, the figures in this paper indicate that the authors incorrectly attribute wall effect to some kind of airflow recirculation occurring near the wall, which does not occur in reality.

Also presented in [26] are some experimental results for an unspecified quadrotor flying in wall effect using the proposed adaptive controller incorporating both IMU and Vicon motion capture data in the loop. Because motion capture systems are impractical outside the laboratory environment, and is required for this flight control system, this is not a good solution for extending the overall autonomous capabilities of UAVs without significant limitations. While this control method may provide a marginal improvement in near-wall stability, it fails to provide a true wall-effect model-predictive solution that could be easily implemented on any multirotor. Overall, the contribution of this paper is somewhat limited because it does not provide any significant advancement in technology that could benefit the ordinary UAV operator in the field. Ideally, a flight controller is needed that can accurately predict the pitching moment produced by wall effect based on the measured separation distance using only a simple set of sensors, and incorporate basic aircraft-specific parameters to calculate the precise control input required to counteract the disturbance and maintain

level flight. The work presented in this dissertation aims to provide future researchers with the information necessary to achieve this goal of model-predictive near-wall flight control.

2.7 Literature Review Remarks

This chapter reveals the state of the art for close-quarter near-obstacle flying as it applies to rotorcraft. This includes ground effect, ceiling effect, and near-wall effect. In this chapter, it is clear that a great deal of research has been done for conventional helicopter ground effect. This research, however, has not been extended to small-scale multirotor aircraft such as those that are so commonly used in today's scientific community. Ceiling effect is similar in principle to ground effect, and has also not been directly explored for multirotors. This dissertation aims to address some of the limitations in the existing vertical-obstacle characterization methodology specifically for multirotor UAVs.

The literature on near-wall effect is more limited than the other subjects, and therefore there is less room for comparison of existing research. The examples of conventional helicopter wall effect research and multirotor wall effect research employ vastly different methods of exploring this phenomena. While simulation can be a powerful tool in aerodynamic modeling, there is very little experimental data available for multirotor wall effect. This dissertation provides an empirical evidence-based approach to describe how near wall flight affects aircraft behavior.

Chapter 3

Ground Effect

In this chapter, the details of the ground effect study are discussed. This begins with a description of the instrumented test stand that is used for all of the experiments in this dissertation. The first section also includes a discussion of the challenges that are faced with mechanical vibration, measurement noise, and component selection, as well as what methods are used to overcome these difficulties. This discussion also serves to justify the final component selection for the remainder of the empirical testing in this dissertation.

The next section discusses the specific experimental procedures that are used for the ground effect study. The section details exactly how each experiment is conducted, including the timing and filtering procedures. This is followed by a results section that describes the results of the ground effect study. The results begin with a verification of the experimental method by comparing a single isolated rotor with the known theory for conventional helicopters. Afterwards, the results of the ground effect study for multirotor ground effect study are presented. The discrepancies with existing theory are discussed in detail, and explained in terms of known aerodynamic phenomena that are unique to rotorcraft.

3.1 Instrumented Test Stand

A custom fabricated test stand, shown in Fig. 3.1, that minimizes airflow obstruction and mechanical vibration is constructed to be sufficiently far from ceilings, floors, and walls so as not to influence the measurements. The test stand features welded steel construction and a central hollow tube with removable end-caps, and is filled with 30 kg of sand to further reduce vibration. An ATI Mini-40 6-DOF force / torque sensor[1] is rigidly mounted to the top of the test stand, to which the aircraft test frame is directly attached. This sensor precisely measures the forces and torques acting on the aircraft test frame via the ATI DAQ F/T System [2], an OEM 'black-box' analog signal processor for converting the raw transducer output into six differential analog channels. This sensor has a capacity of 80 N (F_x, F_y), 240 N (F_z), and 4 Nm (T_x, T_y, T_z), with a minimum resolution of 0.02 N and 0.0005 N-m. These measurements along with the motor speeds are recorded through a National Instruments (NI) USB 6002 DAQ[3] which is interfaced with a computer via USB 2.0.

The early tests that were performed focused on exploring different motor and propeller combinations in an isolated single rotor configuration, as shown in Fig. 3.2. The primary goal was to evaluate what combinations had the most consistent performance over the entire throttle range. The parameters that were covered included motor size (power output and high-speed vs. high-torque), propeller diameter vs. pitch (e.g. large diameter / low pitch vs. small diameter / high pitch), number of blades (2, 3, or 4), and propeller material (nylon, fiber-reinforced nylon, and carbon fiber). In total, more than 20 combinations were tested, however, the initial data was found to be inconsistent for a number of reasons.

[1] Product Webpage: ATI Mini40 F/T Transducer

[2] Product Webpage: ATI DAQ F/T System

[3] Product Webpage: NI USB 6002 DAQ

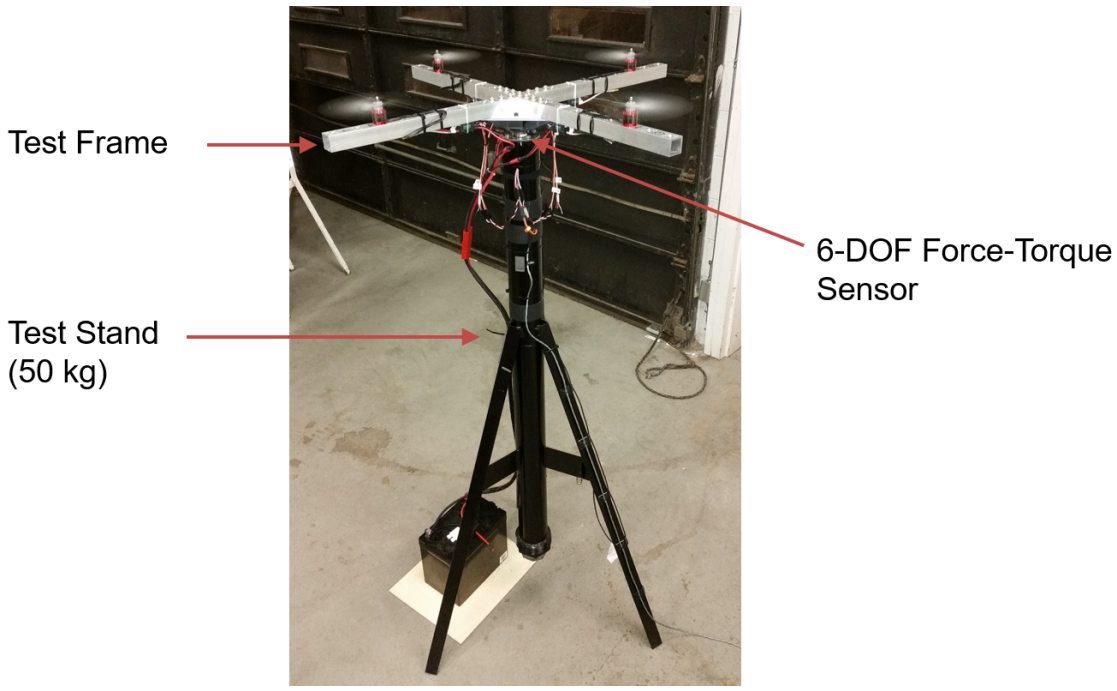

Figure 3.1: Instrumented test stand with the ATI Mini40 F/T sensor. The 12 V battery shown is replaced with an 1100 W PSU prior to the presented empirical studies.

Mechanical vibration causes significant noise in the force and torque measurements. In certain cases, a resonance state is achieved, making measurement impossible because the vibration amplitude often exceeded the limits the F/T transducer. In such instances, the test must be aborted, skipped, and restarted at the next throttle setpoint that is past the resonance frequency, leading to undesirable gaps in the data. Different propellers resonate at different RPMs that are impossible to predict, forcing some combinations to be abandoned altogether.

The vibration issues are not caused by a lack of rigidity in the test stand, but rather an imbalance in the propeller due to minor manufacturing imperfections. It has been determined that none of the propellers are perfectly balanced, even when the manufacturer claims otherwise, and this is true for even the most expensive products that were tested. To remedy the vibration problem, each propeller is carefully balanced using the frictionless balancing apparatus shown in Fig. 3.3 that levitates a shaft between two powerful magnets.

Figure 3.2: Photos of an early test setup using an ExceedRC MonsterPower15 motor with 12×6 3-blade fiber-reinforced composite propeller.

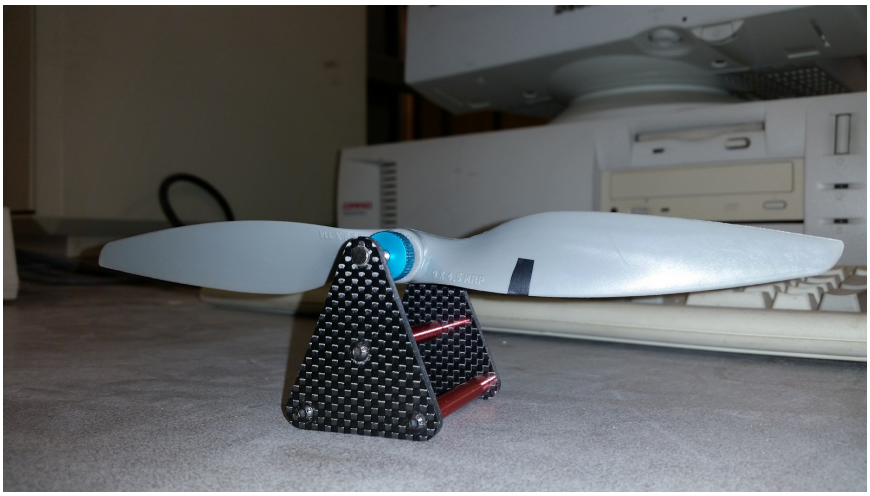

Figure 3.3: Propeller balancing on magnetic bearings. The strip of black tape is used as a counterweight to offset the heavier blade on the left side of the photo.

A small strip of tape wrapped over the leading edge of the blade adds the appropriate mass to one side of the propeller, and the location along the cord length depends on the severity of the imbalance. This procedure is relatively straight-forward for any 2-blabe propeller, but can be exceedingly time-consuming for a 3-blade or 4-blade propeller. Balanced propellers largely reduce the vibration and associated noise in the characterization tests, and eliminated the resonance problems.

The remaining vibration that persisted with balanced propellers is considered acceptable. The characterization tests are repeated to generate the basic characterization curves for shown in Fig. 3.4 for each motor / propeller combination. The first curve shows thrust as a function of motor speed, and the second plot shows measured mechanical power output (calculated from the measured reaction torque about the vertical axis) as a function of thrust.

Notable differences in persistent mechanical vibration are ultimately attributed to the material the propeller is constructed from. Propeller materials are directly associated with the responsiveness of the aircraft, with greater rigidity comes faster responsiveness to sudden changes in motor speed. Nylon propellers are very inexpensive and common among

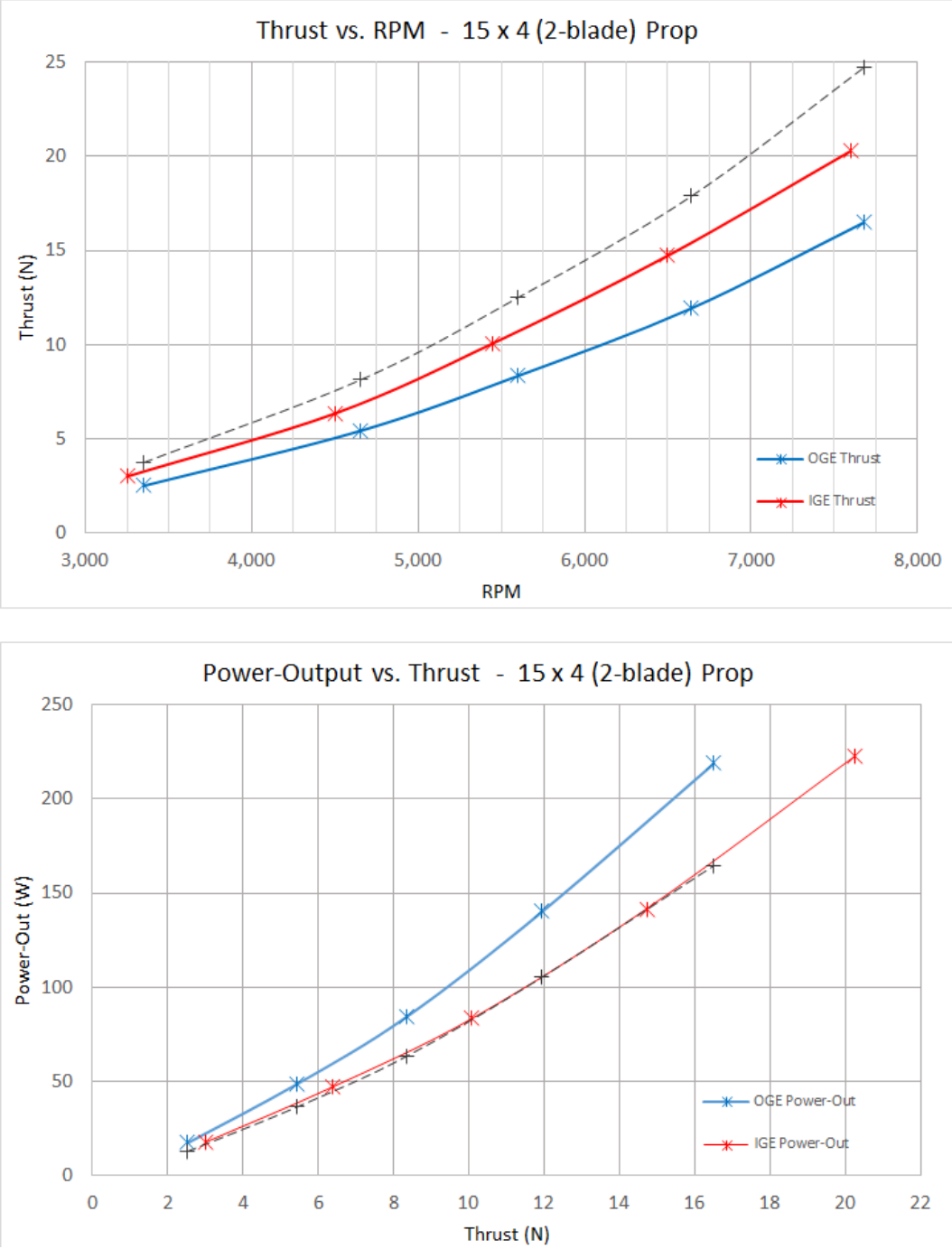

Figure 3.4: Example of the thrust curves as a function of RPM and mechanical power that result from early characterization of individual motor / propeller combinations.

multirotor UAVs because they are cheap to replace when damaged, but are not typically used on professional aircraft. Nylon propellers are also considered somewhat less dangerous because they are thin and flexible, and do not shatter when crashed. Fiber-reinforced nylon propellers are considered to have better performance because of the higher rigidity, and the thicker blades permit a true airfoil profile, but these propellers are much heavier by comparison. The professional level UAV propellers are made from carbon fiber composite, and offer even more rigidity than fiber-reinforced nylon with a significant weight reduction. Carbon fiber propellers have the disadvantage of being very expensive, and are more likely to fail catastrophically by splintering into dangerous fragments in the event of a blade strike.

All of these materials are included in the early characterization tests, and some of the examples are shown in Fig. 3.5. The common belief that an expensive composite propeller is better causes a perplexing dilemma when selecting the best propeller to use for this research. Rigid composite propellers offer better performance because of the reduced dampening of transient RPM changes, however, it was determined that this does not translate into better data quality for bench testing. The inherent dampening of a basic nylon propeller is found to be most desirable for minimizing vibration and improving the quality of the measurements. Eventually, composite propellers were abandoned in favor of nylon propellers for the final propeller selection used throughout this dissertation. Additionally, because of the low expense, it was possible to compare numerous different sizes and styles to find the propeller that results in the best data quality.

Another challenge that influences the accuracy of the data is motor temperature. The stator of a brushless DC motor has an inherent parasitic resistance that causes it to dissipate power in the form of heat. As the stator heats up, it's resistance increases, causing more of the electrical power to be dissipate as heat and reducing efficiency. This is a negative feedback process that can rapidly degrade the motor performance. The airflow from the

Figure 3.5: Some of the various propellers used in early characterization testing.

propeller provides most of the cooling for the motor, but the demands of the experimental process are arguable greater than what the motor might experience if it were powering an aircraft. As seen in Fig. 3.2, the early tests used a 3-D printed plastic adapter to attach the motors to the F/T transducer which thermally insulates the motor from the rest of the test stand. It large metallic mass of the test stand can provide an excellent heat sink if thermally coupled to the motor stator. A custom fabricated 45mm machined aluminum adapter, shown in Fig. 3.6 is used for all subsequent single-rotor experiments to attach the motor to the F/T transducer. This adapter can accommodate 3 different sizes of motors, and provides significantly more cooling capacity by permitting conduction heat transfer into the test stand. The data quality and consistently is greatly improved by keeping the motor temperature relatively stable during repeated high-power operation.

Based on preliminary research, a single motor and propeller combination is chosen that is representative of the most common small/medium scale quadrotors that are widely used by researchers and hobbyists. The 150 W Leopard LC2830-12T (980 kV) brushless

Figure 3.6: Fabricated 45mm aluminum adapter for single Leopard LC2830-980KV Motor and ATI Mini-40 F/T sensor.

motors[4] are comparable in size and power to the most common quadrotor motors offered by numerous manufacturers. The Gemfan 9×4.7 nylon propellers are flexible, inexpensive, widely available and generally more popular compared to composite propellers. This is the most commonly used motor and propeller throughout all of the empirical studies, and is shown in Fig. 3.7 operating as a single isolated rotor. The Castle Creations Phoenix Edge 50A ESCs[5] are not typical for quadrotor on this scale, but their high-quality construction and special features (speed feedback, data logging, superior programmability, etc.) are desirable for this specialized experimentation.

A custom fabricated X-shaped quadrotor test frame, shown in Fig. 3.8 is used for all of the quadrotor experiments. The test frame is specifically designed for this experimental application with heavy-duty construction using 31.8 mm (1.250 inch) square thick-wall aluminum tubing to maximize rigidity and heat dissipation from the motors. The test frame

[4] Product Webpage: Leopard LC2830-12T Brushless Motor (Altitude Hobbies)

[5] Product Webpage: Phoenix Edge 50A ESC (Castle Creations)

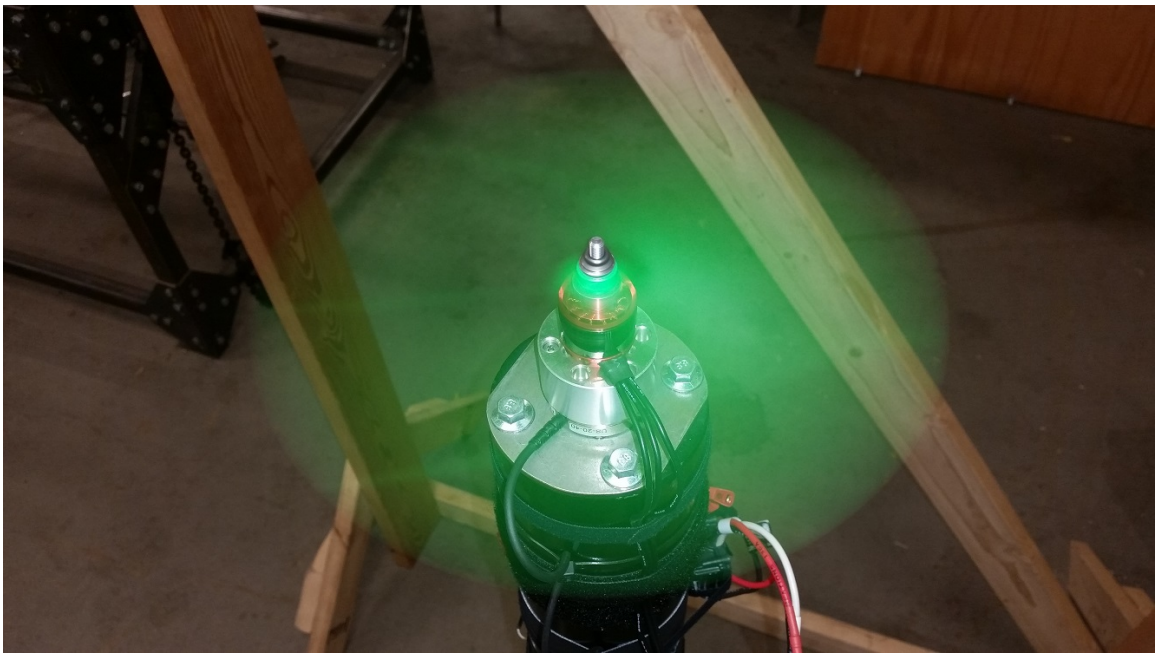

Figure 3.7: Leopard LC2830-12T Motor and GemFan 9×4.7 nylon propeller in single-rotor operation.

is machined with multiple motor mounting locations at 50 mm increments along each arm for exploring how the propeller spacing distance influences T_{IGE}, T_{OGE}, and thrust-power efficiency. The test setup is capable of simulating quadrotors between 390-890 mm as measured diagonally from the motor rotational axis centerlines (center of the motor shaft). Additionally, a different experimental setup is used to evaluate an isolated single propeller under the same test conditions as a point of comparison.

The motors / ESCs require a 12 VDC power source capable of producing at least 60 A overall. Initial attempts using various battery power sources resulted in measurement inconsistencies due to the voltage drop under load and as the state-of-charge decreased. This is normal for all batteries, however it was determined to be an unacceptable drawback because a constant motor speed could not be maintained for more than a few seconds. Instead, an AC-DC power supply unit (PSU) is used, consisting of two parallel Astec (Artesyn) DS550-3 distributed network power supplies[6] for a total output of 90 A at 12

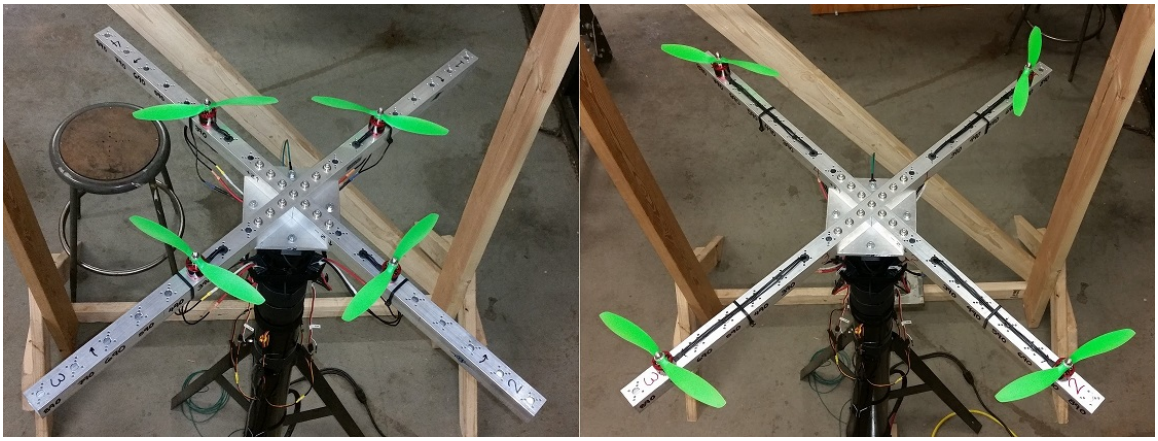

Figure 3.8: Custom fabricated quadrotor test frame composed of 92 cm thick-wall square tubing bolted to a $\frac{1}{4}$ inch plate. Multiple motor mounting locations are located at 50 mm increments along each arm.

VDC, shown in Fig. 3.9. The DS550-3 has an active load sharing feature that allows multiple units to be connected in parallel without the need for external rectifiers. Heavy 6AWG cables and high-power DC connectors carry the DC power to the ESCs and a large 33,000 uF capacitor minimizes transient voltage fluctuations under changing load conditions.

3.2 Methods & Procedures

This section focuses on the experimental evaluation of multiple quadrotor configurations to characterize IGE and OGE hover performance due to ground effect. Additionally, a single isolated rotor case is evaluated and compared to the theoretical predictions given by 2.5, and serves to validate the accuracy of the experimental setup. The experimental apparatus allows for incremental adjustment of three fundamental parameters: 1) the distance between the propeller plane and the ground (Z), 2) the spacing between the propellers on a typical X-shaped quadrotor frame, and 3) the speed of the motors. The experimental setup is focused on eliminating uncontrolled and undesirable influences as much as possi-

[6] Online Datasheet: Astec/Artesyn DS550-3 Power Supply

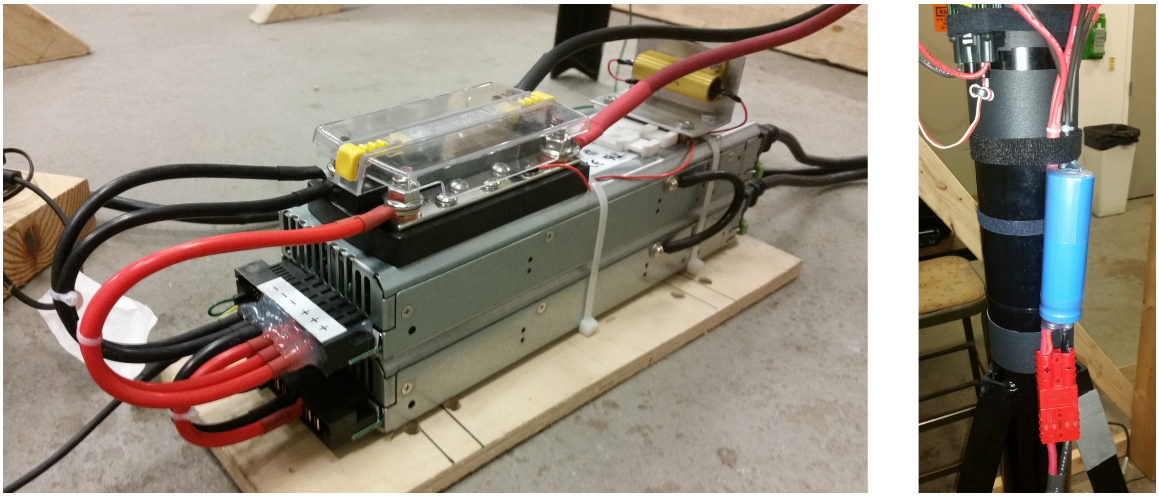

Figure 3.9: Two Astec DS550-3 power supplies connected in parallel using active load sharing. A large 33,000 uF capacitor is mounted to test stand close to the point of load.

ble to isolate only the desired test parameters. Every effort is made to minimize mechanical vibration, EMI, air flow obstruction, temperature variations, etc.

The experiments are performed indoors for climate control purposes in a large loading bay with a 5 m high ceiling so as not to influence ground effect measurements. The experimental setup is inverted so that the airflow directed upward against a large movable flat surface that serves as the"ground" plane. There are two reasons for this: 1) the test frame is at a fixed height so a movable ground surface is required, and 2) the ceiling is sufficiently high so that an upward airflow had more space to disperse without obstruction. The ground height incrementation is accomplished using a large structure that supports a 2.4 m square sheet of reinforced plywood that recreates a ground surface. The vertical posts of the structure have holes at increments of 2.5 cm, through which metal rods are inserted to support the plywood ground surface. The height is incremented by lifting each side of the plywood slightly, and reinserting the metal rod into the next hole on the structure. While simplistic, this apparatus makes it possible to evaluate ground effect in controlled small increments through a large range of heights from $\approx$3-120 cm. The results presented

in this chapter demonstrate that (2.5) cannot be applied to multirotors because it does not accurately predict the change in lift due to ground effect.

3.2.1 Testing Procedures

The raw data from the F/T sensor is inherently noisy due to mechanical vibrations from the motor and propeller. Each propeller is carefully balanced on magnetic bearing as shown in Fig. 3.3, but the mechanical noise cannot be eliminated using this method alone. An averaging filter is implemented because of its computational simplicity and overall effectiveness. The tests are all performed using a sampling rate of 1 kHz, and an averaging size of 250 samples. This results in an effective sampling rate of 40 Hz, with each sample consisting of 6 component measurements. The motor speeds and supply voltage are measured separately without filtering. Additional data recorded by the ESCs, including voltage, current, power, RPM, throttle input, temperature, and ripple voltage is downloaded from each ESC at the conclusion of each experiment.

Incrementing the speed of the motors directly affects thrust, disk loading, power loading, and induced velocities. Because the power output of the motor is directly related to propeller speed, an increase in speed also represents an increase in power, however the relationship in not linear. Therefore, when the propeller speed is constant, it can be assumed that, ideally, the motor power is also constant. A closed-loop speed controller is implemented by matching the timing of the motor speed feedback signals from the ESCs. A master-slave approach modulates the PWM signals for three of the ESCs to match the speed of the master ESC receiving the PWM signal set by the operator. This method ensures the motor speeds are always identical. While this is unlikely for a real quadrotor in flight responding to disturbances and unequal payload distribution, it is essential for replicating an ideal static hover scenario that is desirable in controlled empirical evaluation.

The data collection procedure begins with a 3 minute warm-up cycle to get the motors up to their typical operating temperature of ≈40°C. Motor temperature has a significant impact on performance, so it is critical to maintain a consistent operating temperature by carefully timing the duty cycle. At each increment of the test parameters described above, the motors are held at a constant throttle for a 10 second data collection of the vertical thrust (F_z). In the single-propeller experiments, the reaction torque (T_z) acting against the rotating propeller is also measured / recorded to directly calculate the motor's true mechanical power output and efficiency. After each 10 second test, the throttle is reduced to a minimum level for 90 seconds to avoid heat buildup in the motors. During the 90 second dead-time the test parameter is incremented again, after which the process repeats. This procedure is used throughout all of the experiments, and the temperature and humidity is always recorded.

In total, 396 separate data collections are recorded and analyzed in this study, exploring numerous combinations of the test parameters mentioned above. Three different motor speeds are tested at 22 height increments from the ground surface between ≈3-120 cm. In addition to the isolated single propeller case, this was performed for five different propeller spacings on the quadrotor test frame, 39-79 cm diagonally in 10 cm increments.

3.3 Results

This section presents the measured thrust performance of the chosen motor / propeller combination spinning at constant speed as a function of the height from the ground surface. Thrust performance is represented by the dimensionless ratio T_{IGE}/T_{OGE} in all cases, where 1 is the performance level when the propeller(s) is very far from the ground (OGE). When the ratio is greater than unity, there is an increase in thrust due to the ground effect. For comparison, the theoretical predicted thrust performance is calculated from (2.5) and

Figure 3.10: Experimental setup for a single isolated propeller, shown at a distance of $Z = R$ from the inverted ground surface.

represented by a dashed line. The comparison between measured and predicted thrust performance is discussed in detail.

3.3.1 Ground Effect Performance for a Single Isolated Propeller

The classical theories of propeller performance were developed for an isolated single-propeller case. Likewise, the conventional theories for helicopter ground effect in (2.5) and (2.7) that only consider a single main rotor. Beginning with the evaluation of an isolated single propeller serves to validate the experimental setup, and forms a basis for comparison to identify how the interactions between multiple propellers affect the overall hover performance. Figs. 3.7 and 3.10 show the single-propeller experimental setup and operation.

The data shown in Fig. 3.11 describes the measured and predicted thrust performance of a single motor and propeller at constant speed. This plot clearly shows the significant increase in thrust performance very close to the ground, and because this is a dimension-

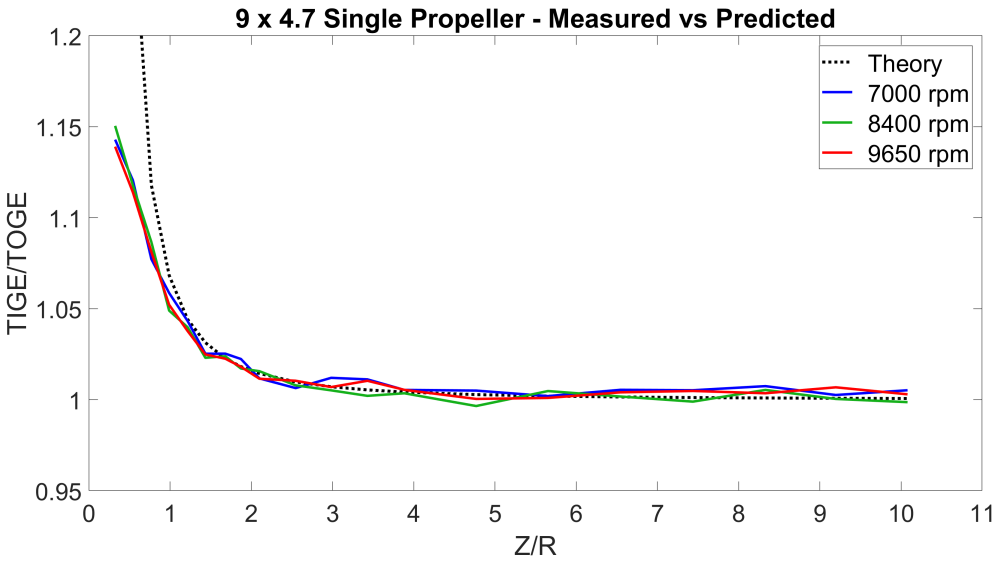

Figure 3.11: Ground effect performance for a single isolated propeller.

less value, it is essentially the independent of propeller speed and/or motor power. The plot also illustrates the rapid decrease in thrust performance as height increases, decaying asymptotically to 1, and ground effect becomes insignificant above $Z \simeq 4R$. All of these observations are characteristic of the classical ground effect model defined by (2.5), and can be seen in both the measured and predicted performance curves in all cases. The curves do not match up perfectly however, and there is a clear divergence at the extreme lowest height ratios (Z/R) as the curves approach the mathematical limitations of (2.5).

$$Re = \frac{inertial forces}{viscous forces} = \frac{\rho u L}{\mu} \tag{3.1}$$

Other minor deviations between the measured and theoretical curves could be attributed to the fact that small-scale aircraft operate in a sensitive range of Reynolds number that is not true of large-scale aircraft. For small-scale propellers, complex flow patterns can exist in the boundary region around the airfoil which can have a significant effect on the thrust performance [32]. Equation (3.1) defines Reynolds number in terms of L as the charac-

teristic linear dimension of the propeller blade, u is the fluid velocity w.r.t. the propeller blade, ρ is fluid density, and μ is the dynamic viscosity. In both full-scale and small-scale rotorcraft, the rotor tip speed is always limited by the speed of sound, therefore, the value of u is similar in both cases across the rotor blade span from root to tip. The length of the rotor blade span, however, is dramatically different in these two cases, resulting in a very large velocity gradient across the blade span for small-scale rotorcraft. Additionally, the value of L (which can be precisely determined from a *Blade Element Theory* analysis) is much smaller for small-scale multirotor propellers compared to full-scale helicopter rotors. So-called "*critical Reynolds numbers*" determine where turbulent flow transitions occur, and can indicate the vorticity of the flow. A flow that is close to these critical values will be highly sensitive to dimensional-scaling, which can significantly and abruptly affect the flow behavior as a result rotor dimensions.

3.3.2 Quadrotor Ground Effect Performance

The presumption that the thrust performance of a multirotor can be treated as the sum of single rotors is an oversimplification of a multifaceted problem. By applying (2.5) to a single rotor, and multiplying by the number of rotors (n), as suggested in [33] and [37] is equivalent to having one propeller of the same diameter that produces a thrust equal n times the thrust. According to Momentum Theory, the cross-section of the accelerated flow in the ultimate wake of the propeller is smaller than the disk area of the propeller, shown in Fig. 2.1. Therefore, without obstruction, the multiple discrete flow streams produced by a multirotor will not combine into one larger flow, but rather become more differentiated as they continue far beyond the propellers along parallel axes. The quadrotor experimental setup is shown in Fig. 3.12 for a 490 mm configuration.

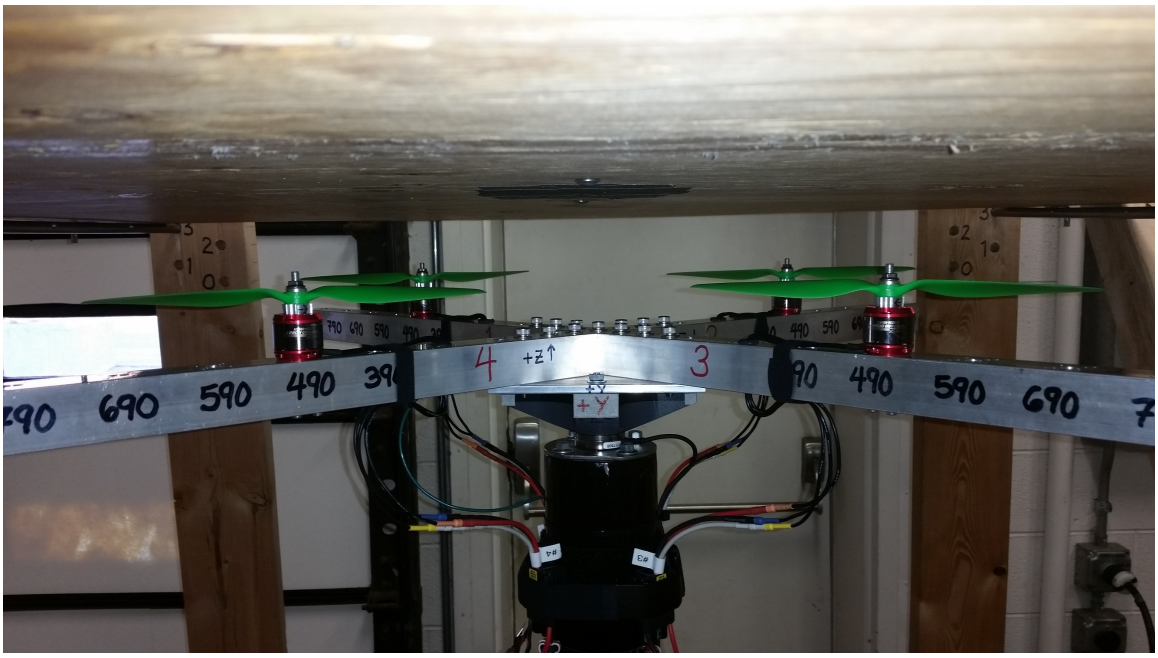

Figure 3.12: Experimental setup for a 490 mm quadrotor, shown at a distance of $Z = R/2$ from ceiling surface.

Close to the ground, it is necessary to consider how these flow streams will interact when they encounter the ground surface. As each discrete flow encounters the surface, it cannot spread out radially in all directions due to the adjacent flows. Colliding air from adjacent flow streams hitting the surface prevents the even radial spread seen in Fig. 2.3, further limiting the induced velocity of each flow. It is logical to expect an increase in thrust performance, as a result, that would not occur in a single-rotor situation.

The plots in Fig. 3.13 show several quadrotor thrust ratio curves of ground effect for various propeller spacings. Additionally, Fig. 3.14 shows quadrotor ground effect using several different propeller sizes at a fixed spacing of 690 mm. It is immediately evident that the measured thrust performance differs significantly from the predictions made by (2.5) as well as the single-propeller performance curves. As discussed, there is a significant increase in thrust performance that does not exist in single rotor cases, and as a result, is not predicted by (2.5). It is interesting to note that this increase does not occur closest to

the ground, but rather at a distance around $Z \simeq 4R$ where ground effect is supposed to become insignificant according to (2.5) and the single-propeller measurements.

Equally notable, between $Z \simeq 1.5R$ and $Z \simeq 2R$, the ground proximity actually produces a detrimental effect on the lift, which briefly drops below 1.0. This can be explained by examining the interaction / collision of discrete air flows at the ground surface described above. First, it is important to consider the structure of the wake flow below each individual rotor, a representation of this is shown in Fig. 3.15. Just as a fixed-wing aircraft produces wing-tip vortices that persist in the far wake of the plane, a lifting rotor also produces similar blade-tip vortices that are carried down in the wake boundary in a double-helical pattern (for a 2-blade propeller). These blade tip vortices produce upward recirculation around the outside of the wake boundary. Momentum Theory dictates that if the wake collides with the ground, the flow velocity slows, and the diameter of the wake must increase to conserve momentum, carrying the boundary vortices outward as well. If the height from the ground is similar to the radius of the blade-tip vortices, a recirculation can be created around the outside of the rotor and back through the center.

For a multirotor, the wake cannot uniformly spread out radially at the ground where it collides with an adjacent wake, some of the colliding air will be forced to curl away from the surface and away from the adjacent wake in the upward direction of the discrete blade tip vortices. Because the blade-tip vortices in all of the adjacent wakes curl upward in the same direction, the mixing of the discrete wakes at the ground surface can combine the vortices into a single recirculation flow around the outside circumference of the aircraft. If the rotor spacing of the aircraft is sufficiently large, the adjacent-wake blade-tip vortices can also combine within the center of the airframe, creating another recirculation path up through the center of the airframe between the propellers. As with the single rotor, if the height from the ground is similar to the radius of the combined-wake blade-tip vortices, a recirculation can be created around the circumference of the aircraft and another recircu-

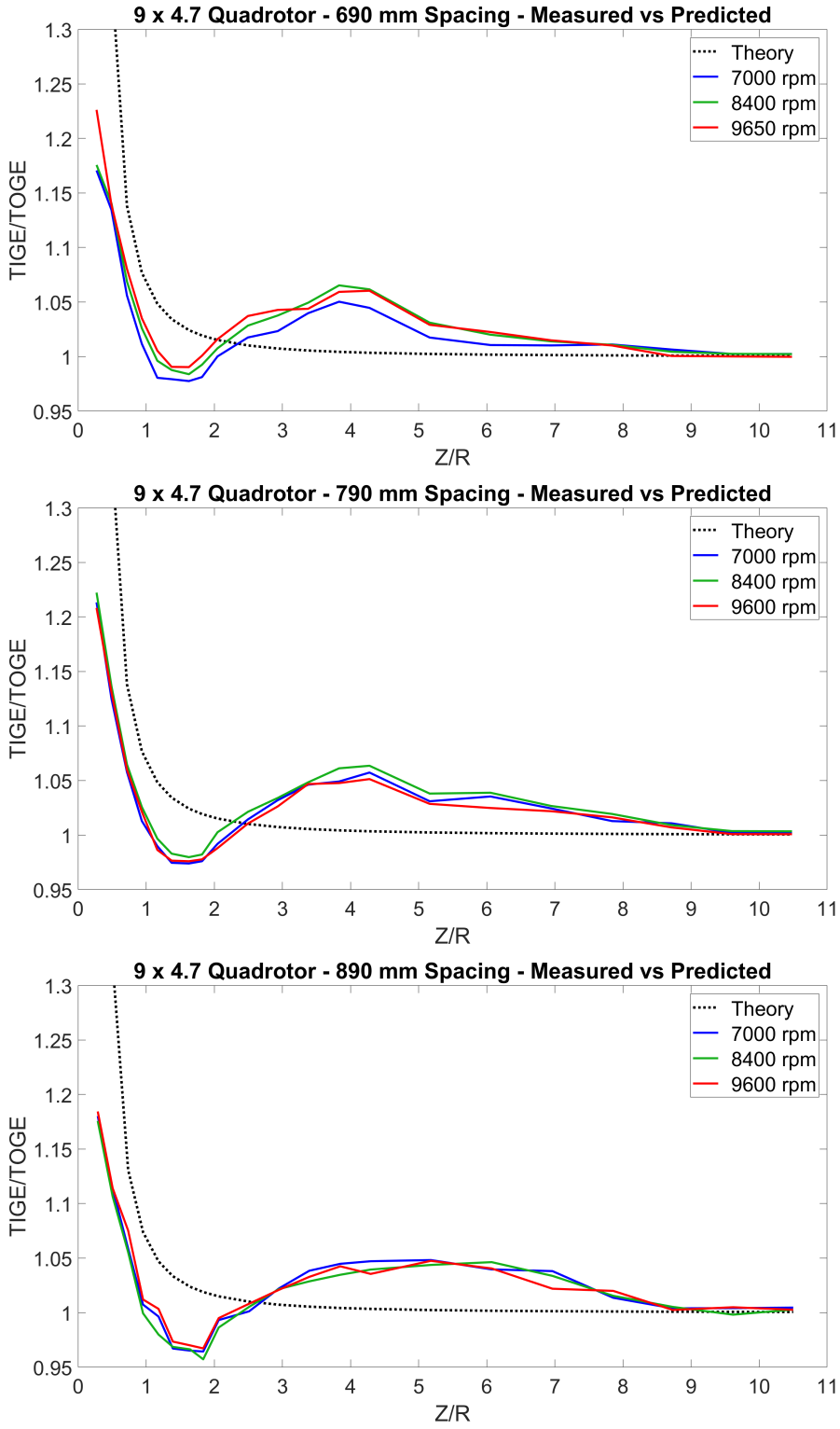

Figure 3.13: Ground effect performance for 690, 790, and 890 mm quadrotor configurations.

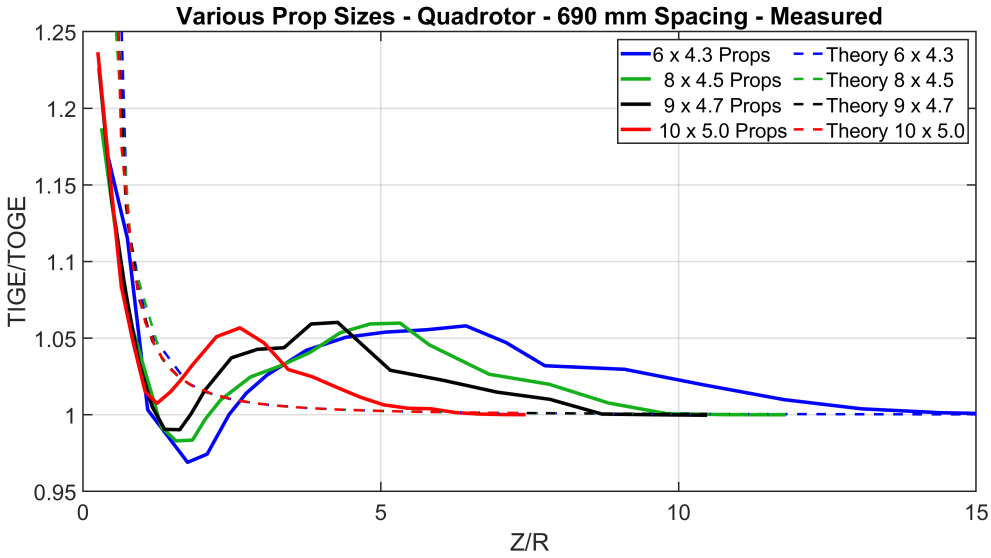

Figure 3.14: Quadrotor ground effect for various propeller sizes at 690 mm spacing.

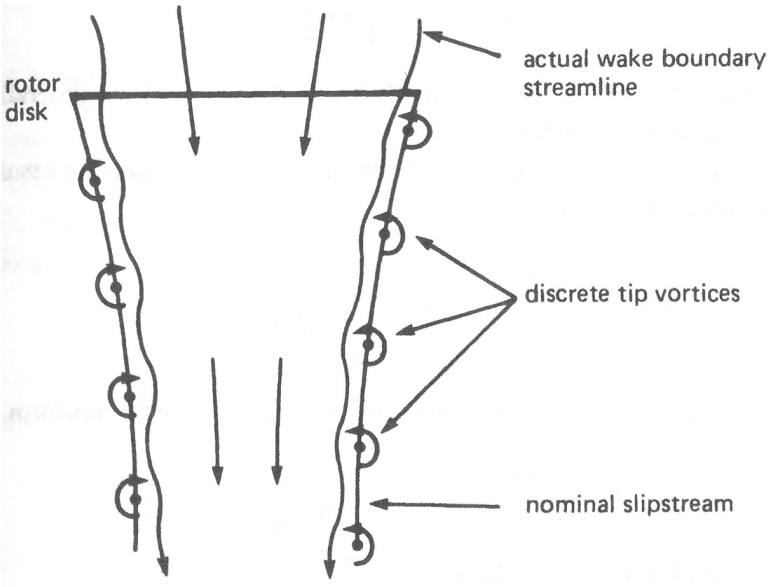

Figure 3.15: Illustration of the discrete wake of a lifting rotor with the blade-tip vortices carried in the downwash boundary [24].

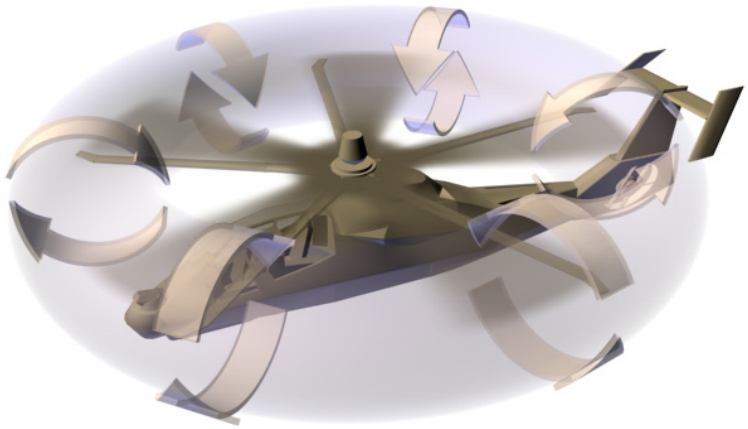

Figure 3.16: Illustration of a vortex ring state of a RAH-66 Comanche helicopter [41].

lation up through the center, with both being pulled back down through the rotors. This sets up a poloidal flow condition that is characteristic of a vortex ring [28] and [23], which have been observed in similar situations such as microbursts [7], [38] and [3]. When a vortex ring recirculates around a spinning rotor, it can result in a loss of thrust that cannot be corrected by increasing power, known in aviation as a *vortex ring state* [24], [18], [17] and [39] illustrated by Figs. 3.16 and 3.17. A vortex ring state is possible for multirotor aircraft as well, with smaller UAVs being the most susceptible [41], and experiences have been reported by RC quadrotor pilots [42]. Figs. 3.13 support this line of reasoning, since the reduced thrust performance in this region exists in curves measured at different power levels. When sufficiently far from the ground surface, any blade-tip vortices remain discrete and confined to the wake of each individual rotor until mixing occurs at the ground far downstream. Because any possible combined-wake tip vortices that may be produced at the ground surface are far below the rotor plane, there is no risk of recirculation through the rotors and there is no loss of thrust.

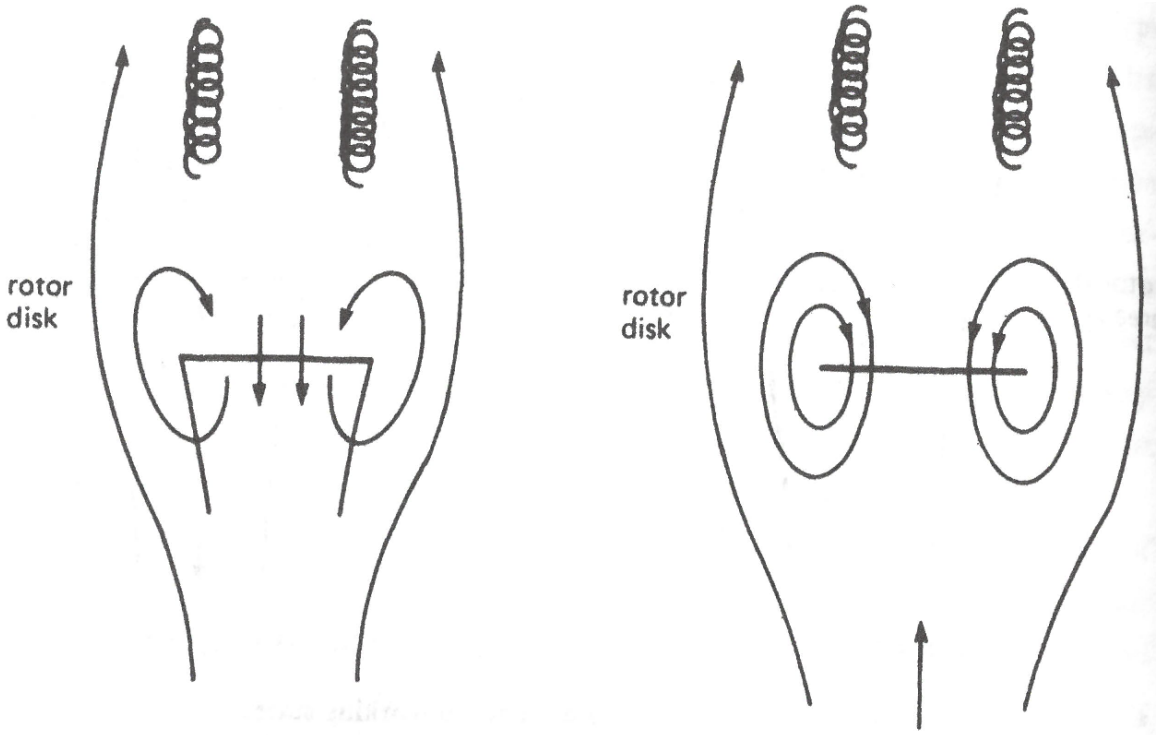

Figure 3.17: Illustration of the flow through a rotor disk in both developing (left) and fully-developed (right) vortex ring states [24].

Chapter 4

Ceiling Effect

In this chapter, the details of the ceiling effect study are discussed. The instrumented test stand shares the same configuration as the ground effect study, with the exception of the thrust direction, and is described in Chapter 3. The first section describes the experimental methods and procedures that are used for the ceiling effect study. The section details exactly how each experiment is conducted, including the timing and filtering procedures. This also includes a discussion of the new challenges that are faced which are unique to the ceiling effect experimentation, and the methods used to overcome these difficulties.

The next section discusses the results of the experimental testing that comprise the ceiling effect study. The results begin with a verification of the experimental method by comparing a single isolated rotor with the known theory for conventional helicopters. Afterwards, the results of the multirotor ceiling effect study are presented. The findings are discussed in detail, and explained in terms of known aerodynamic phenomena that are unique to rotorcraft. A comparison is made with the ground effect study in Chapter 3 and the observed differences are discussed and justified.

4.1 Methods & Procedures

This chapter focuses on the experimental evaluation of multiple quadrotor configurations to characterize ICE and OCE hover performance due to ceiling effect. The experimental apparatus allows for incremental adjustment of three fundamental parameters: 1) the distance between the rotor plane and the ceiling (Z), 2) the spacing between the propellers on a typical X-shaped quadrotor frame, and 3) the speed of the motors. The experimental setup is focused on eliminating uncontrolled and undesirable influences as much as possible to isolate the desired test parameters. Every effort is made to minimize mechanical vibration, EMI, air flow obstruction, temperature variations, etc.

4.1.1 Testing Procedures

The testing procedures for the ceiling effect experiments presented in this chapter are the same as those presented in Chapter 3 except that the direction of thrust is reversed. In Chapter 3 the setup is inverted with the thrust directed upward against the surface to reproduce a ground effect scenario. In all of the ceiling effect experiments in this chapter the thrust is directed downwards and away from the surface, therefore it is possible to reproduce a ceiling effect scenario using the same experimental apparatus.

The raw data from the F/T sensor is inherently noisy due to mechanical vibrations from the motor and propeller. Each propeller is carefully balanced on magnetic bearing as shown in Fig. 3.3, but the mechanical noise cannot be eliminated using this method alone. An averaging filter is implemented because of its computational simplicity and overall effectiveness. The tests are all performed using a sampling rate of 1 kHz, and an averaging size of 250 samples. This results in an effective sampling rate of 40 Hz, with each sample consisting of 6 component measurements. The motor speeds and supply voltage are measured separately without filtering. Additional data recorded by the ESCs,

including voltage, current, power, RPM, throttle input, temperature, and ripple voltage is downloaded from each ESC at the conclusion of each experiment.

Many of the challenges with mechanical vibration are overcome using the methods described in Chapter 3. The ceiling effect experiments also generate additional vibrations in the movable wooden ceiling surface that did not occur during the ground effect experiments. The resulting vibrations in the test apparatus create a very loud noise at the closest testing distance due to resonance in the ceiling surface. The amplitude of the vibrations is large enough to invalidate the set point distance for those particular tests. The loud noise also creates a sympathetic vibration in the quadrotor test frame, greatly increasing measurement noise. To eliminate this problem, four steel angle bars are bolted to the back side of the ceiling surface to increase rigidity. Flush carriage bolts are used so there are no protrusions on the flat testing side of the ceiling surface. The increased rigidity of the reinforced ceiling surface is sufficient to dampen the noise, and eliminate the sympathetic vibration in the quadrotor test frame.

Incrementing the speed of the motors directly affects thrust, disk loading, power loading, and induced velocities. Because the power output of the motor is directly related to propeller speed, an increase in speed also represents an increase in power, however the relationship is not linear. Therefore, when the propeller speed is constant, it can be assumed that, ideally, the motor power is also constant. A closed-loop speed controller is implemented by matching the timing of the motor speed feedback signals from the ESCs. A master-slave approach modulates the PWM signals for three of the ESCs to match the speed of the master ESC receiving the PWM signal set by the operator. This method ensures the motor speeds are always identical. While this is unlikely for a real quadrotor in flight responding to disturbances and unequal payload distribution, it is essential for replicating the ideal static hover scenario that is desirable for controlled empirical evaluation.

The data collection procedure begins with a 3 minute warm-up cycle to get the motors to their typical operating temperature of ≈40°C. Motor temperature has a significant impact on performance, so it is critical to maintain a consistent operating temperature by carefully timing the experimental duty cycle. At each increment of the test parameters described above, the motors are held at a constant throttle for a 10 second data collection, then the throttle is increased to the next setpoint and another 10 seconds of data is collected. After the tests are performed at three increasing throttle settings, the throttle is reduced to a minimum level for 90 seconds to avoid heat buildup in the motors. During the 90 second dead-time the test parameter is incremented again, after which the process repeats. This procedure is used throughout all of the experiments, and the temperature and humidity is always recorded.

Three different motor speeds are tested at 22 ceiling distance increments between ≈3-120 cm. In addition to the isolated single propeller case, data was gathered for five different propeller spacings on the quadrotor test frame, 39-79 cm diagonally in 10 cm increments. In total, 396 separate data collections (66 for single-rotor and 330 for quadrotor cases) are recorded and analyzed in this study, exploring numerous combinations of the test parameters mentioned above.

4.2 Results

This section presents the measured thrust performance of the chosen motor / propeller combination spinning at constant speed as a function of the distance from the ceiling to the rotor plane represented by the dimensionless ratio Z/R. The results from the single isolated propeller case and various quadrotor test cases are all presented in this section. Three different propeller speeds are shown in each plot to demonstrate that ceiling effect manifests in the same way regardless of the power required to maintain a hover (i.e. air-

Figure 4.1: Experimental setup for a single isolated propeller, shown at a distance of $Z = R$ from the ceiling surface.

craft payload or available thrust-to-weight ratio). Thrust performance is represented by the dimensionless ratio T_{ICE}/T_{OCE} in all cases, where a value of 1.0 is the performance when the propeller(s) is very far from the ceiling (OCE). When the ratio is greater than unity, there is an increase in thrust due to the ceiling effect. Because the plots are fully normalized, direct comparisons can be made between the results in all of the experimental cases presented. For comparison, the theoretical predicted thrust performance is calculated from (2.8) and represented by a dashed line. The comparison between measured and predicted thrust performance is discussed in detail.

4.2.1 Ceiling Effect Performance for a Single Isolated Propeller

The classical theories of propeller analysis were developed for a single isolated propeller case. Likewise, the conventional model for helicopter ceiling effect in (2.8) were derived for a single main rotor. Beginning with the evaluation of an isolated single pro-

peller serves to validate the experimental setup, and forms a basis for comparison to identify if any interactions occur between multiple propellers that could alter the performance, and thus, deviate from the theory. The data shown in Fig. 4.2 describes the measured and predicted thrust performance of a single motor and propeller at constant speed. Fig. 4.1 shows this experimental setup for this case.

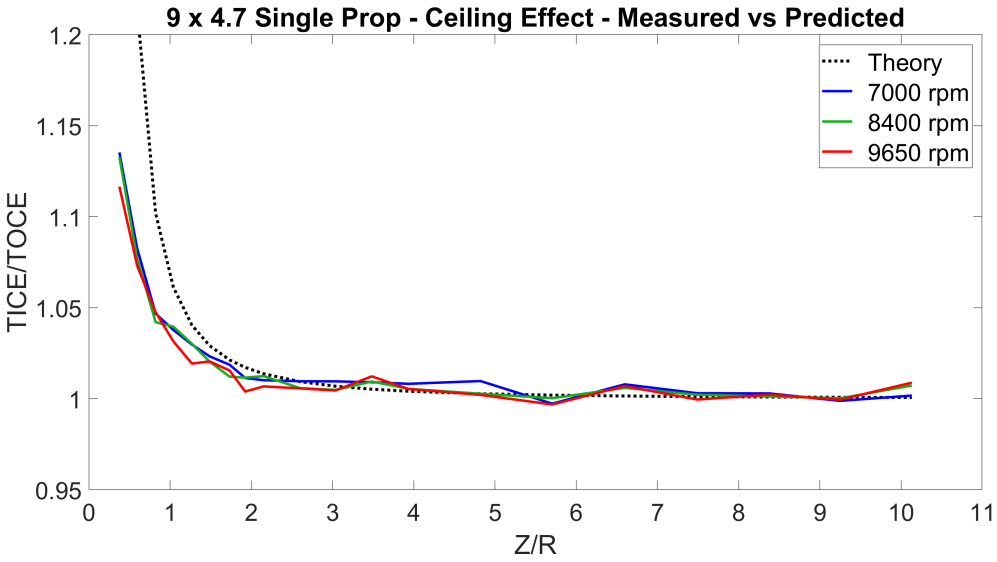

Figure 4.2: Ceiling effect performance for a single isolated propeller.

The plot in Fig. 4.2 clearly shows the significant increase in thrust performance very close to the ceiling, and because this is a dimensionless value, it is essentially independent of propeller speed and/or motor power. The plot also illustrates the rapid asymptotic decay of thrust performance as the distance increases, until ceiling effect becomes insignificant around $Z \simeq 2R$. These observations are all characteristic of the conventional ceiling effect equation (2.8), and there is clear agreement between the observed and predicted values. The curves do not match up perfectly however, which can be explained by two inaccuracies that are inherent to (2.8). 1) The equation's predicted change in thrust at very close distances increases exponentially toward ∞, which is beyond what is physically possible because of the finite theoretical maximum thrust that can be produced by a given motor and propeller.

2) small-scale aircraft operate in a sensitive range of Reynolds number in which complex flow patterns can exist in the boundary region around the airfoil [32], but this is not true of large scale aircraft.

4.2.2 Quadrotor Ceiling Effect Performance

The single-rotor case serves to validate the experimental setup by showing agreement between the measured and predicted ceiling effect thrust performance. Transitioning to a quadrotor configuration with various propeller spacings, as shown in Fig. 3.12 serves as the basis for determining whether or not the adjacent rotors interact in such a way that (2.8) cannot accurately predict ICE performance. The results presented in [10] using the same experimental procedure illustrate how these interactions have a significant effect on ground effect performance that deviated from the conventional helicopter theory (2.8). It is clear from [10] that the downstream interactions of the highly-directional adjacent flow streams below the propeller plane are responsible for the deviation from the theory, but ceiling effect is dependent only on the airflow above the rotor plane which is not purely directional and does not behave in the same way. The various experimental cases for a quadrotor configuration, shown in Fig. 4.3 support this line of reasoning, and show agreement between the measured ICE performance and the predictions made by (2.8). This agreement occurs in all six of the quadrotor configurations that were evaluated.

The results of the ceiling effect study confirm the hypothesis that the single-rotor equation (2.8) can be directly applied to predict the ICE performance of a quadrotor of varying configurations with equivalent accuracy. This also supports the argument that it is the downstream airflow interactions that are responsible for the differences in single-rotor and multirotor ground effect performance. Because of the direct correlation between single-rotor and multirotor ICE performance, and (2.8), it is reasonable to claim that the math-

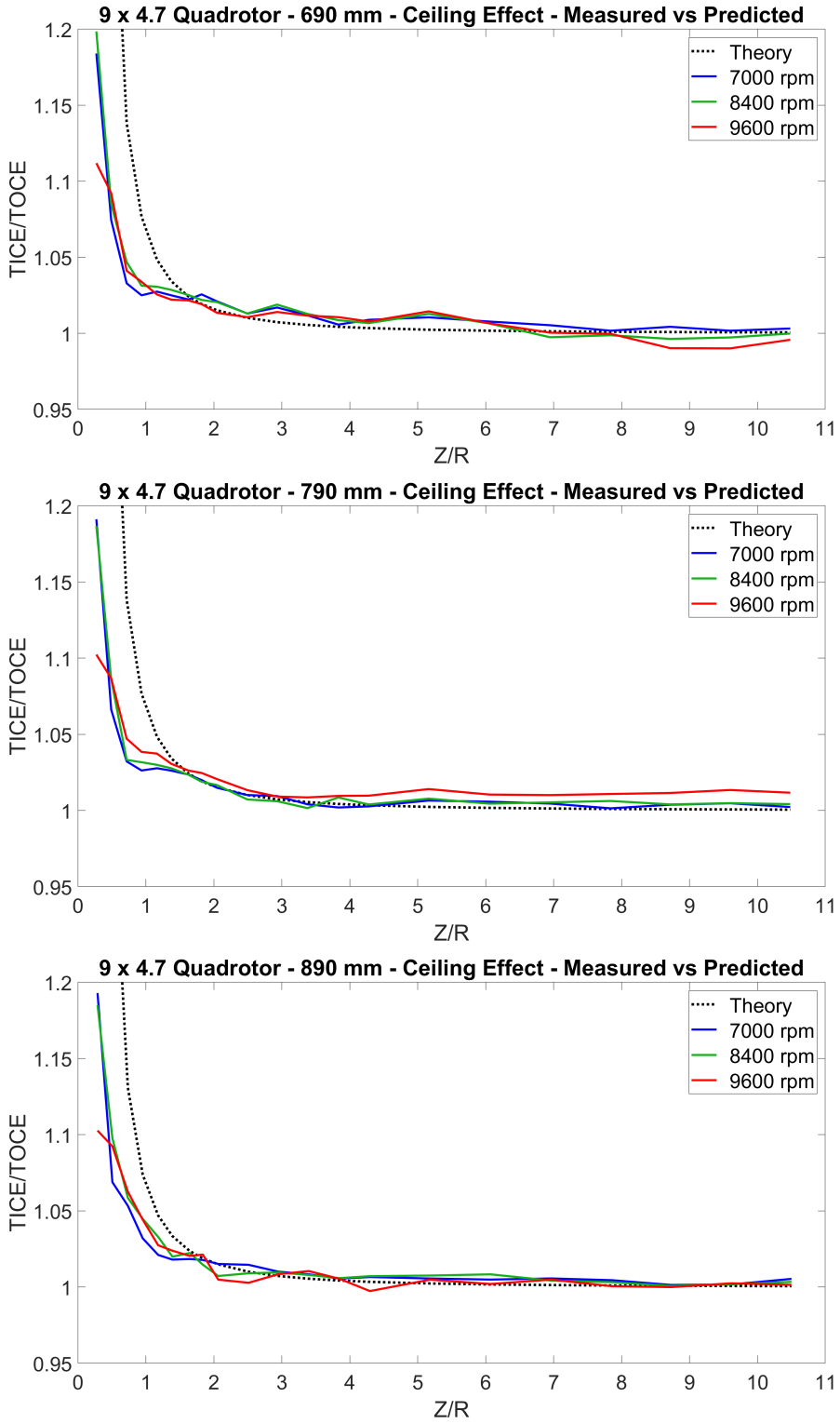

Figure 4.3: Ceiling effect performance for 690, 790, and 890 mm quadrotor configurations.

ematical model of multirotor ceiling effect has been established. A multirotor flight controller can be designed to use (2.8) to predict the change in thrust (motor speed) required to maintain a stable hover while varying in proximity to a ceiling. This model predictive controller would therefore only require three basic metrics to achieve stable ceiling effect flight:

- The known radius of the propellers with which the UAV is equipped. This can be a hard-coded value in the flight controller software that would only require changing if different propellers are equipped.
- A direct measurement of the distance between the rotor plane and the ceiling. This can be achieved using basic sensors such as laser or ultrasonic sensors that have a short measurement range of a few meters, but centimeter-level accuracy.
- The throttle level required to maintain a stable hover while Out of Ceiling Effect (OCE). Assuming the UAV payload does not change during flight, this can be recorded by the flight controller at the beginning of each flight during a brief hover when the aircraft is sufficiently far away from both ground and ceiling. This approach would not require any operator-defined changes to the flight control software if the payload varies between flights.

Using this ceiling effect model and a straight-forward approach to flight controller design, an autonomous multirotor UAV will be developed that can demonstrate superior stability when operating in close proximity to a ceiling.

Chapter 5

Near-Wall Effect

This chapter presents the empirical study of wall effect. The instrumented test stand shares the same configuration as the ground effect and ceiling effect studies, as described in Chapter 3, however, a new test apparatus is constructed to simulate a wall that can be incremented in distance from the aircraft test frame. The first section describes the experimental apparatus that is constructed specifically for simulating wall effect. The first section also includes a discussion of the challenges that are associated with the different experimental setup. The second section discusses the specific experimental procedures that are used for the wall effect study. The section details exactly how each experiment is conducted, including an explanation of how various aircraft orientations are explored and how the results are to be presented.

This is followed by a results section that describes the results of the wall effect study. The results describing quadrotor wall effect are presented according to the different orientations of the aircraft frame with respect to the wall. The observations of the measured forces and torques produced by the proximity to the wall are discussed and characterized according to the independent test variables that govern each set of experiments.

5.1 Experimental Apparatus

This section describes the experimental apparatus that is used for the wall effect studies, and some of the associated challenges and limitations that are encountered. The wall effect study uses the same instrumented test stand, aircraft test frame, power and control systems that are used throughout all of the studies presented in this dissertation, and described in detail in Chapter 3. The test stand is intentionally designed to be heavy, 50 kg overall, to help resist mechanical vibration, and the hollow center column is filled with 30 kg of sand that also absorbs vibration energy. Additionally, all of the wiring for power, control, and instrumentation is secured to the test stand and runs down to the floor. These considerations make moving the test stand impractical, therefore, a movable wall apparatus is needed to simulate wall effect. The experimental apparatus that is used for the ground effect and ceiling effect studies in Chapters 3 and 4 is constructed around the test stand to simulate an obstructing surface at incremental distances above the aircraft test frame. Because this vertically-oriented apparatus cannot be adapted to simulate a wall, it is necessary to construct a completely different structure that is specifically designed for wall effect experiments.

The wall effect apparatus must meet the following requirements:

- It must have a movable wall surface to provide the ability to quickly and accurately increment the separation distance between the test stand and the wall surface.
- It must be possible for a single person to operate the apparatus.
- The separation increments must be small in comparison to the aircraft test frame and the chosen propeller diameter to provide multiple data points in the critical region where the aircraft is closest to the wall.

- The wall must be sufficiently wide in comparison to the aircraft test frame to accurately represent an actual building wall and ensure that the airflow is not influenced by interactions with the edges of the wall.

- The wall must be sufficiently tall to extend from well above the test stand down to as close as possible to the ground, as would an actual building wall.

- The entire structure must be sufficiently rigid so that the wall does not move, flap, or vibrate even when exposed to the strong airflow produced during the the experiments.

The apparatus constructed according to these design requirements is shown in Fig. 5.1 with the instrumented test stand shown without the aircraft test frame mounted. This structure features a movable OSB plywood (Oriented Stranded Board) wall that is completely flat on the front side, with no gaps or raised features, and is reinforced on the back side to maintain sufficient rigidity. The plywood wall measures 8 feet tall and 7 feet wide, with the width being constrained by the available space in the equipment bay and the need for a person to be easily able to walk around the apparatus. A large wooden frame is constructed around the wall to act as a support structure and facilitate the distance incrementation. The frame is fully supported on three of the sides with cross beams and diagonal braces, but only a ground-level cross beam exists on the front side so as not to obstruct the wall.

The structure is no more complicated than absolutely necessary, and the method used to increment the wall separation distance is an integral part of the apparatus. The design allows the separations distance to be set between 0-60 inches from the front of the apparatus in increment of 2 inches, creating a total of 31 possible data points to test. Because the plywood wall is not attached to the surrounding frame, it is necessary to support both the top and bottom of the wall at every location within the apparatus to ensure it is vertical and does not fall over. A series of holes and slots in the cross beams make it possible to immobilize the wall at a known distance from the front of the apparatus, then quickly move

Figure 5.1: Wall effect test apparatus featuring a 8×7 foot OSB plywood wall that can be incremented horizontally from $0 - 60$ inches from the test stand.

the wall to the next increment. The width between the lower cross beams is narrower than the wall, but the width of the upper cross beams is wider than the wall. This allows the wall to fit between the upper cross beams, while resting on top of the lower cross beams. Precise slots are cut into the top side of the lower cross beams using a router, thus providing a cradle that secures the bottom edge of the wall at regular intervals along the beam, as shown in Fig. 5.2a. One person can easily lift one corner of the wall at a time and move it to the next slot, and the 1/16 inch oversized slots permit this temporary misalignment.

With the bottom edge of the wall held in place by the slots, the upper portion of the wall must also be secured so that the wall is completely immobilized at any given location. Three metal eyelets (U-shaped clamps used for securing water pipes) are attached to the back side of the plywood to allow a 1/2 inch aluminum rod to be passed horizontally through them. Corresponding holes are drilled through the upper cross beams at 2 inch increments so that the metal rod can be inserted all the way through the apparatus and secure the upper

portion of the wall, as shown in Fig. 5.2b. The holes and slots are offset by 1.25 inches to compensate for the width of the plywood and the eyelet radius so that the wall is perfectly vertical at each location. One end of the metal rod is pinned so that it is always inserted the correct amount. To change the separation distance, the rod is removed through one side of the apparatus, the bottom corners of the wall are moved to the next slot, and the metal rod is re-inserted. This incrementation usually takes between 30-40 seconds for a single person, ensuring that the tests can be performed in rapid succession so that the motors remain at a consistent operating temperature.

The wall effect apparatus performs its function well, but there are some unforeseen challenges that must be addressed to guarantee experimental accuracy and efficiency. Initially, it was thought that the size and mass of the apparatus would prevent it from shifting position during normal operation. The action of moving the wall position caused the entire apparatus to move slightly each time, requiring constant repositioning and compromising the accuracy of the experiment. The frame of the apparatus is bolted to the concrete floor using eight anchors, as shown in Fig. 5.3, and eliminating the problem of unintended shifts in position.

Another challenge arises from the decision to leave the front of the apparatus frame open so as not to obstruct the wall. Because the front of the frame is not braced with cross beams like the other three sides, it does not remain square, causing the wall to jam in the frame when moved to one of the forward positions. It became necessary to add a structural member across the top of the front side of the frame. Minimizing obstruction remains an important consideration, so instead of a wood cross beam, metal rod is pinned through the top of the frame and held in tension as seen in Fig 5.7.

Another issue is the deterioration of the bottom corners of the plywood that fit into the slots of the cross beam. During regular use, the corners of the plywood gradually crack and

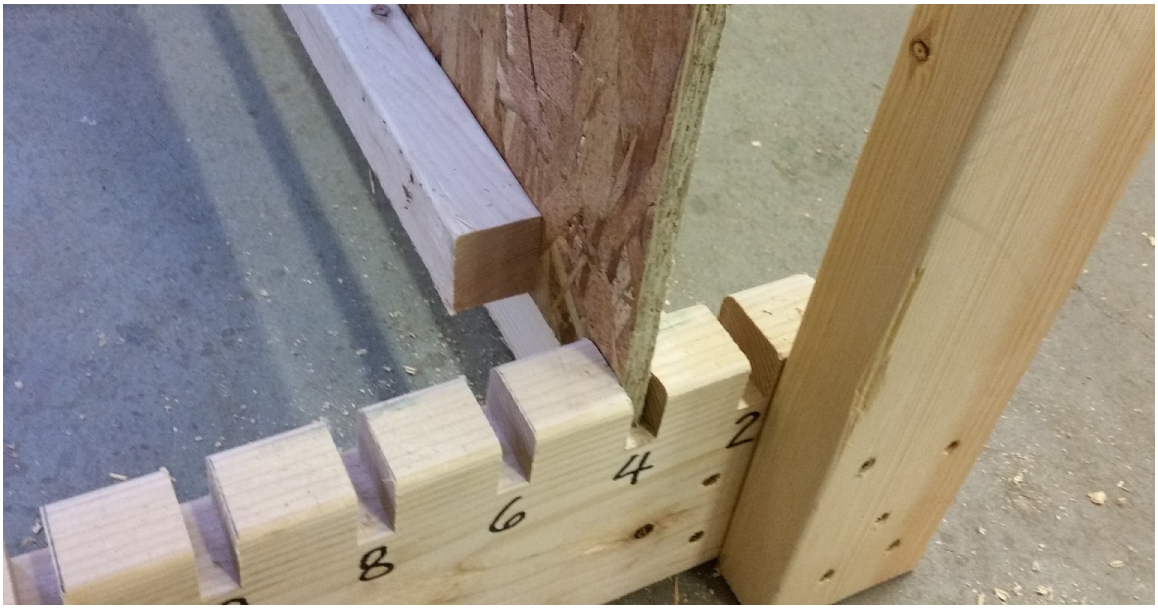

(a) Wall rests in routed slots in the base cross beams

(b) Removable metal rod secures the wall through holes and eyelets

Figure 5.2: Photos of the rear side of the plywood wall showing how the incrementation is achieved with precise slots and holes. A removable metal rod passes through holes in the upper cross beams and eyelets on the back of the plywood.

Figure 5.3: Anchor bolts and steel bracket securing each corner of the experimental apparatus to the concrete floor.

break apart, causing it to rest unevenly in the slots. It is necessary to reinforce the bottom edge of the plywood with a strip of metal to prevent any further deterioration.

5.2 Methods & Procedures

This section describes the experimental process used to evaluate wall effect. The quadrotor test frame that is used throughout this dissertation allows for propeller spacing from 390-890 mm along the diagonal, as shown in Fig. 3.8. For the purposes of evaluating wall effect, only the 890 mm configuration is used to keep the the propellers as close as possible to the wall. The experiments are performed indoors for climate control purposes in a large loading bay with a 5 m high ceiling so as to minimize external influences. The test stand is initially positioned in front of the wall so the the tips of the propellers are as

close as possible to it without colliding. The distance to all four corners of the test frame is measured to ensure that the orientation of the test frame with respect to the wall is correct for the experiment.

The multirotor wall effect studies explore two different orientations of the aircraft with respect to the wall, as shown in Fig. 5.4:

1. The "broadside" pose, in which the quadrotor is oriented at 45° to the wall so that two rotors are equally close to the wall on either side of the centerline.

2. The "tip-side" pose, in which the quadrotor is oriented at 90° to the wall so that a single rotor is closest to the wall directly on the centerline, as shown in Fig. 5.7.

In either case, the experiments are performed as four separate tests, one test case for each of the four poses in the chosen orientation. The aircraft test frame is rotated $\pm$ 90° to the next pose between each test, thus changing which of the individually-numbered motor-propeller pairs are closest to the wall, as shown in Fig. 5.5. This multi-pose method is used because the motors and propellers are not identical, and the measurement data can vary slightly depending on which propeller(s) are closest to the wall. To deliver the most accurate results, the four poses of each orientation are averaged into a single data set for each experiment. This method smooths out most of the minor variations associated with the different motors-propeller pairs, improving the quality of the measurement data while maintaining a realistic set of results.

5.2.1 Testing Procedures

The raw data from the F/T sensor is inherently noisy due to mechanical vibrations from the motor and propeller. Each propeller is carefully balanced on magnetic bearing as shown in Fig. 3.3, but the mechanical noise cannot be eliminated using this method

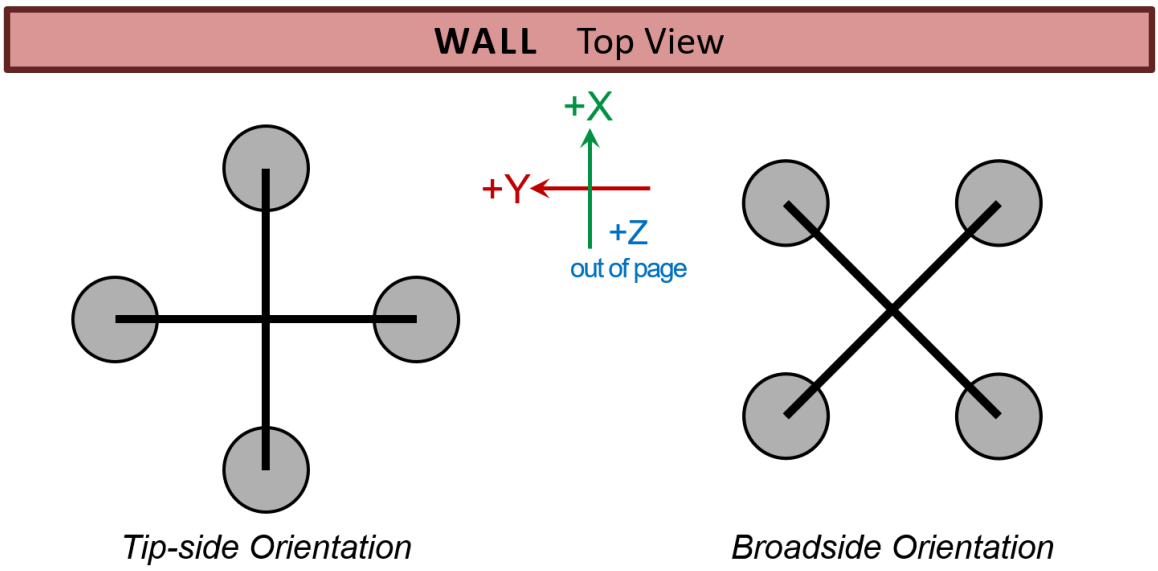

Figure 5.4: Top-view illustration of the "tip-side" and "broadside" aircraft orientations with respect to the wall.

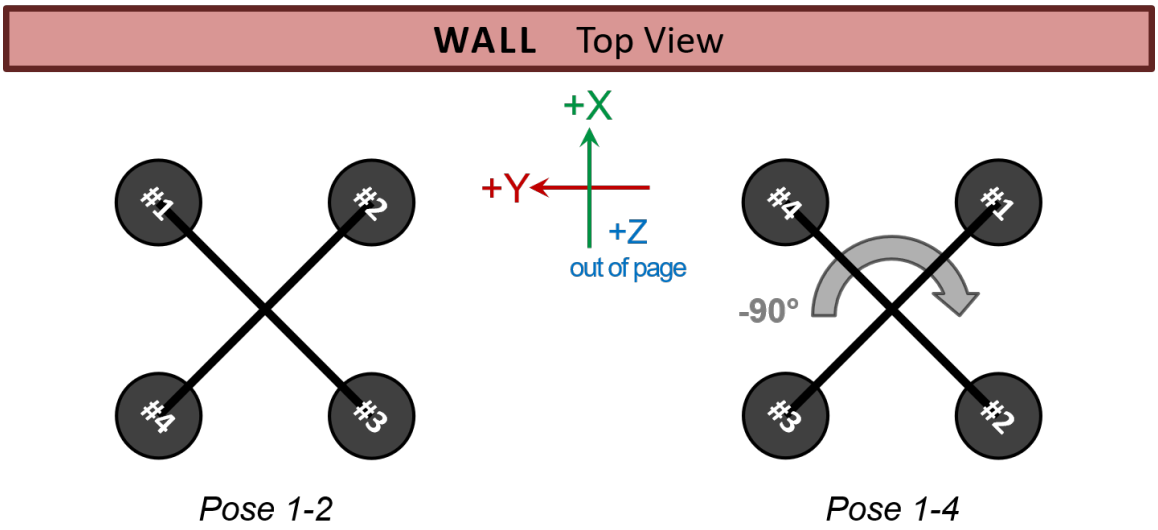

Figure 5.5: Top-view illustration of the transition from one aircraft pose to the next, thereby changing which motor-propeller pairs are closest to the wall.

alone. An averaging filter is implemented because of its computational simplicity and overall effectiveness. The tests are all performed using a sampling rate of 1 kHz, and an averaging size of 250 samples. This results in an effective sampling rate of 40 Hz, with each sample consisting of 6 component measurements. The motor speeds and supply voltage are measured separately without filtering. Additional data recorded by the ESCs, including voltage, current, power, RPM, throttle input, temperature, and ripple voltage is downloaded from each ESC at the conclusion of each experiment.

Incrementing the speed of the motors directly affects thrust, disk loading, power loading, and induced velocities. Because the power output of the motor is directly related to propeller speed, an increase in speed also represents an increase in power, however the relationship in not linear. Therefore, when the propeller speed is constant, it can be assumed that, ideally, the motor power is also constant. A closed-loop speed controller is implemented by matching the timing of the motor speed feedback signals from the ESCs. A master-slave approach modulates the PWM signals for three of the ESCs to match the speed of the master ESC receiving the PWM signal set by the operator. This method ensures the motor speeds are always identical. While this is unlikely for a real quadrotor in flight responding to disturbances and unequal payload distribution, it is essential for replicating the ideal static hover scenario that is desirable for controlled empirical evaluation.

The data collection procedure begins with a 3 minute warm-up cycle to get the motors up to their typical operating temperature of $\approx$40°C. Motor temperature has a significant impact on performance, so it is critical to maintain a consistent operating temperature by carefully timing the duty cycle. At each increment of the test parameters described above, the motors are held at a constant throttle for a 10 second data collection. After each 10 second test, the throttle is reduced to a minimum level for 90 seconds to avoid heat buildup in the motors. During the 90 second dead-time the test parameter is incremented again,

after which the process repeats. This procedure is used throughout all of the experiments, and the temperature and humidity is always recorded.

5.3 Results

This section describes the results of the wall effect study. The data is presented in terms of normalized non-dimensional forces and torques exerted on the aircraft test frame as a function of the separation distance from the wall. The separation distance is measured from the rotating axis (center of the shaft) of the closest motor(s) to the wall. The four different poses of each orientation are averaged together to provide a single pair of plots for each orientation.

5.3.1 Single Isolated Propeller Behavior

The evaluation of a single isolated propeller in wall effect is an important aspect to consider to develop an overall understanding of this phenomena. Single-propeller wall effect experiments are completed, but not to the extent of producing presentable data. These experiments, as shown in Fig. 5.6, have produced only preliminary data because of the physical challenges of conducting these tests. The width of the base of the test stand prevents close-proximity tests of single-propeller wall effect. The wall effect test apparatus must be modified to to allow for these single-propeller tests. This task is considered potential future work, and is discussed further in Chapter 7.

5.3.2 Quadrotor Wall Effect Behavior

The studies described in Chapters 3 and 4 focus on quantifying the apparent increase in lift (vertical thrust) experienced by a rotorcraft as it approaches the ground or the ceil-

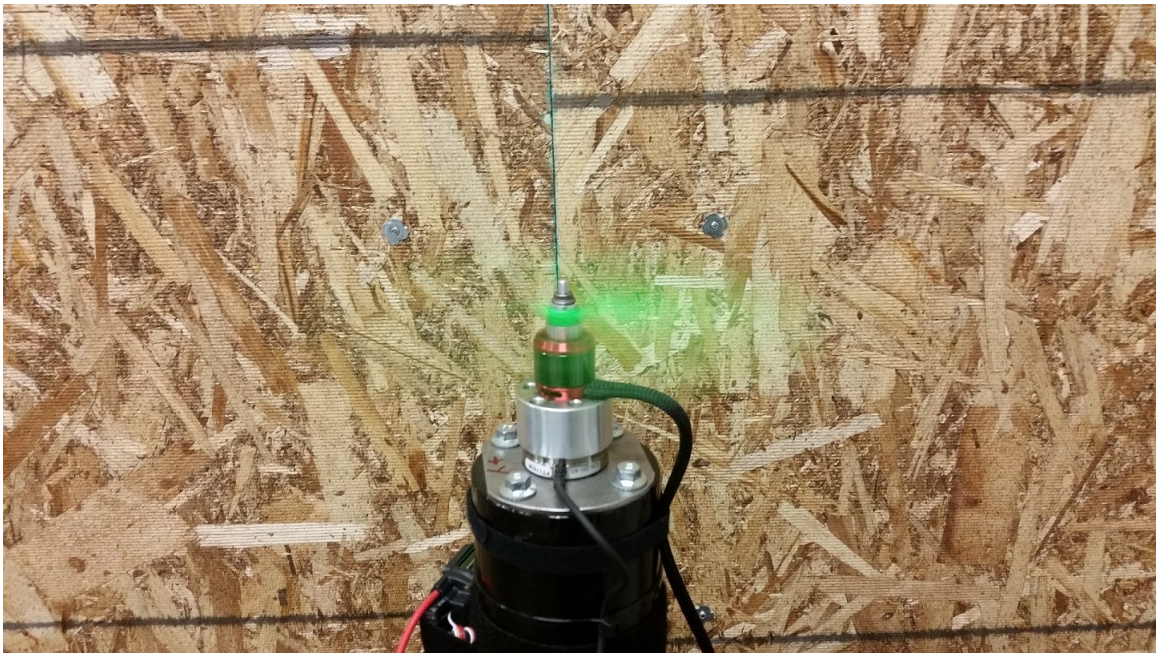

Figure 5.6: A single isolated propeller operating in one of the wall effect experiments.

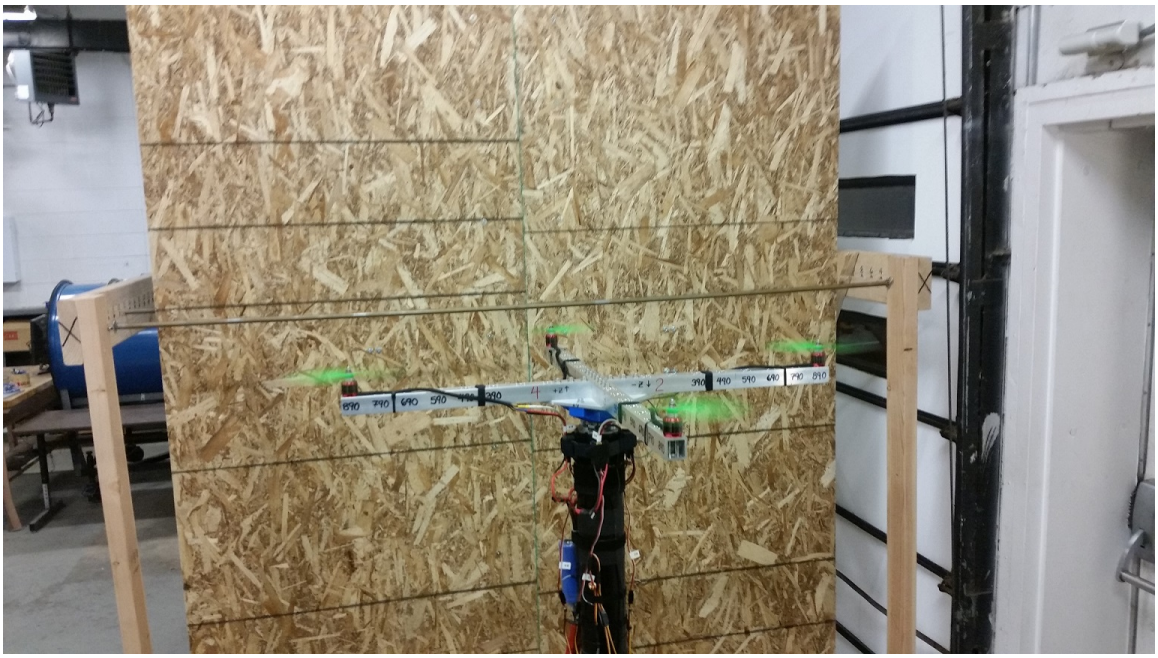

Figure 5.7: Wall effect testing with quadrotor test frame in a tip-side orientation at a 90° angle to the wall.

ing. Both ground effect and ceiling effect are quantified by a single vertical force vector (F_z) corresponding to the rotor-generated thrust from the aircraft. In the single-propeller experiments, the reaction torque (T_z) acting against the rotating propeller is also recorded to directly calculate the motor's true mechanical power output and efficiency. This study experimentally evaluates and quantifies the multi-directional forces and moments that act on a hovering rotorcraft as a function of its proximity to a vertical wall. Similar to ground and ceiling effect, flying in close proximity to a vertical wall results in aerodynamic interactions that effect the stability and predictability of a rotorcraft. This wall effect manifests as both a pitching moment (T_y) and a horizontal attraction force (F_x) on the aircraft frame. Contrary to the ground effect and ceiling effect measurements, the force and torque on the vertical axis (F_z and T_z) should ideally remain zero throughout the wall effect experiments, indicating no external disturbances and confirming the rotor plane is perpendicular to the wall.

The proximity of the wall causes the aircraft to pitch down toward the wall, and simultaneously be pulled towards it, as shown in Figs. 5.8, 5.9, and 5.10. As stated earlier, the four different poses of each orientation (90° apart from each other) are averaged together to provide a single pair of plots for each orientation at three different throttle levels. The horizontal force directed toward the wall is represented by the green line in Figs. 5.8a, 5.9a, and 5.10a, and clearly exhibits a dramatic increase in very close proximity to the wall, and diminishes sharply as the separation distance increases. Likewise, the dotted red line in Figs. 5.8b, 5.9b, and 5.10b clearly exhibits a dramatic pitching moment very close to the wall, and also decreases rapidly as the separation distance increases.

Because the aircraft test frame is fixed, the pitching moment cannot change the direction of the thrust vector, which remains vertical and parallel to the face of the wall. Therefore, the pitching moment is not the source of the accompanying attractive force that pulls the aircraft towards the wall. These results show that the two principle components of wall

effect act independently on the aircraft, and even without any change in pitch angle, the aircraft is still pulled towards the wall. Of course, a free-flying aircraft isn't constrained in this way, and would pitch down towards the wall without any control input; This angles the thrust vector away from vertical and more towards the wall, increasing the overall attraction of the aircraft towards the wall. This inherent coupling between the pitch angle and the thrust vector has frequently been assumed to be the cause-and-effect of the characteristic wall effect attraction. The results presented here represent the first empirical data for multirotor wall effect that shows the pitching moment (T_y) and the attractive force (F_x) are independent of each other; the pitching moment does not cause the attractive horizontal force.

This data does not represent all of the wall effect experiments that have been performed, however it does show the most complete datasets that have thus far been collected. Further research and experimentation on wall effect is included as potential future work, and will continue as described in Chapter 7.

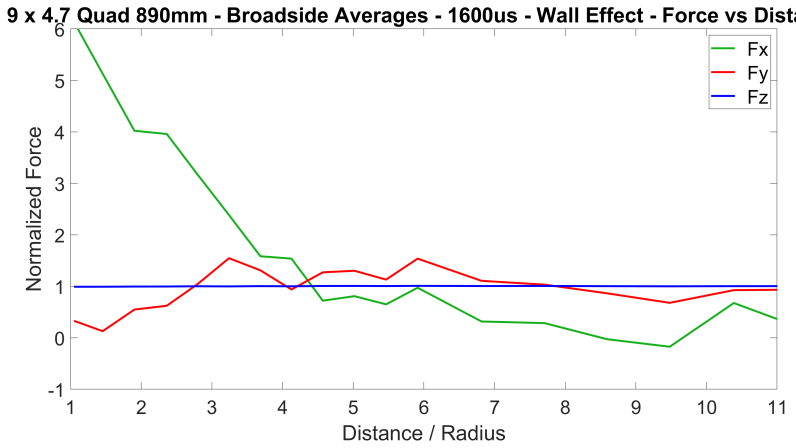

(a) Normalized reaction forces at 50% throttle.

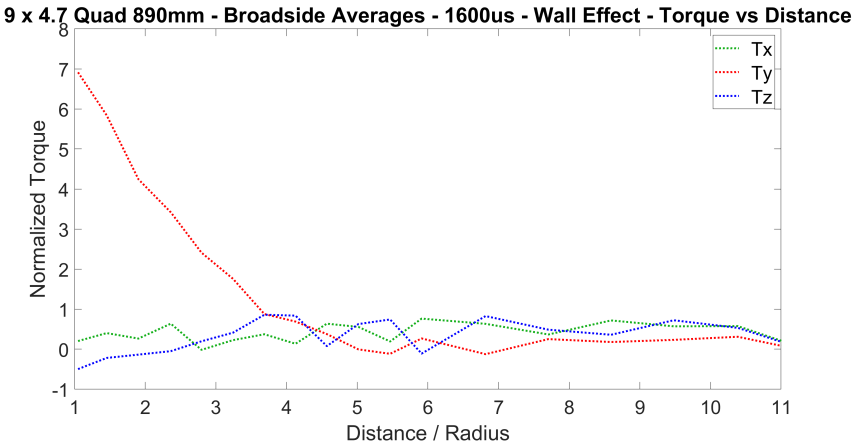

(b) Normalized reaction torques at 50% throttle.

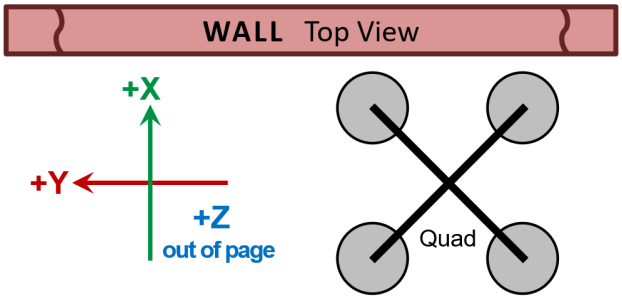

(c) Broadside orientation with color-coded F/T measurement axes.

Figure 5.8: Force and torque due to wall effect for broadside 890 mm quadrotor configuration according to color-coded measurement axes in illustration. Throttle set point at 50%.

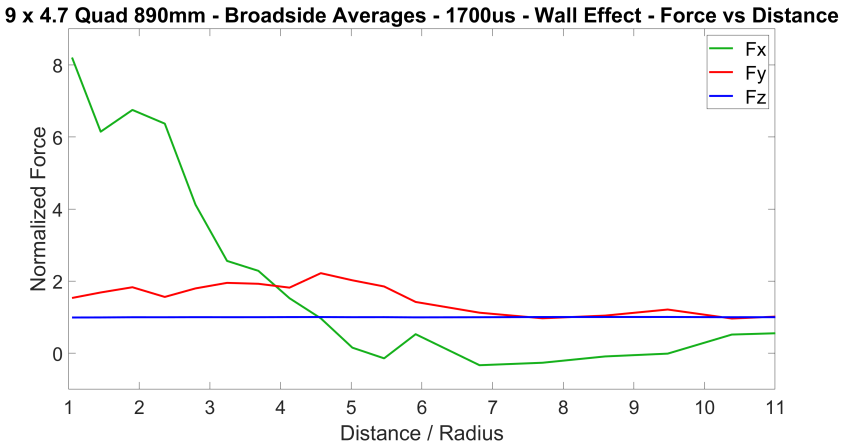

(a) Normalized reaction forces at 70% throttle.

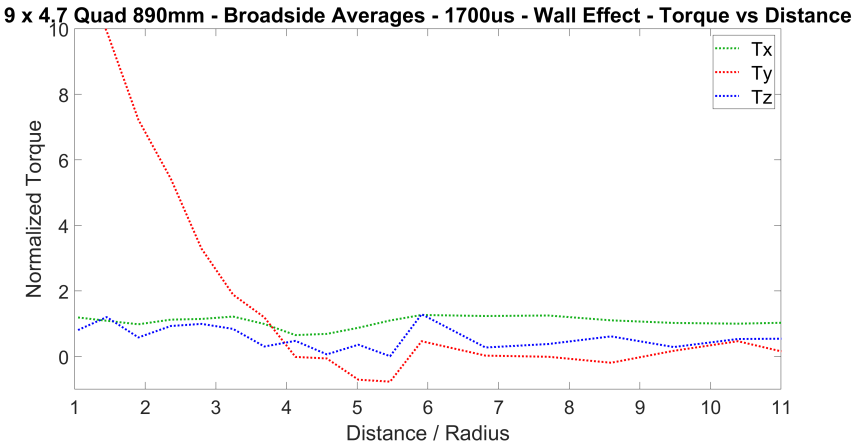

(b) Normalized reaction torques at 70% throttle.

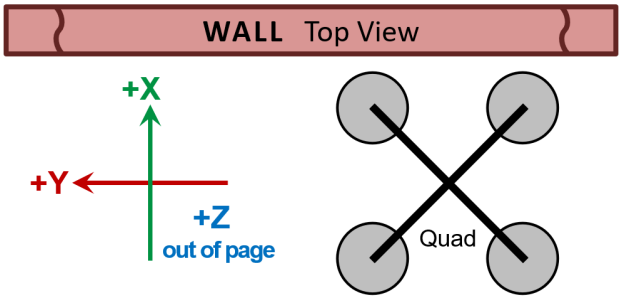

(c) Broadside orientation with color-coded F/T measurement axes.

Figure 5.9: Force and torque due to wall effect for broadside 890 mm quadrotor configuration according to color-coded measurement axes in illustration. Throttle set point at 70%.

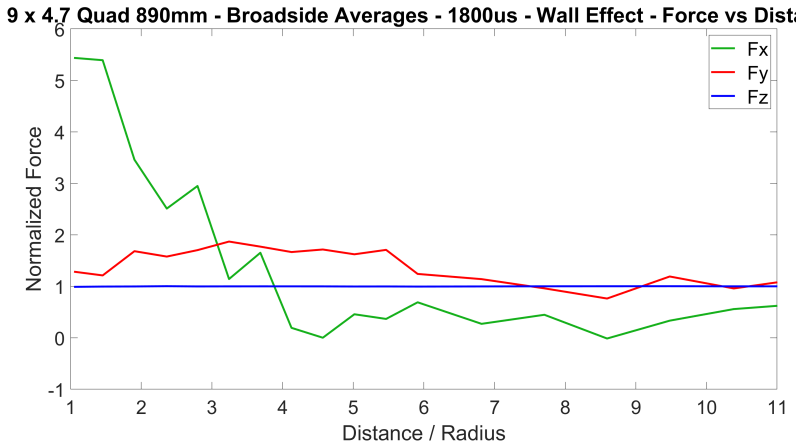

(a) Normalized reaction forces at 90% throttle.

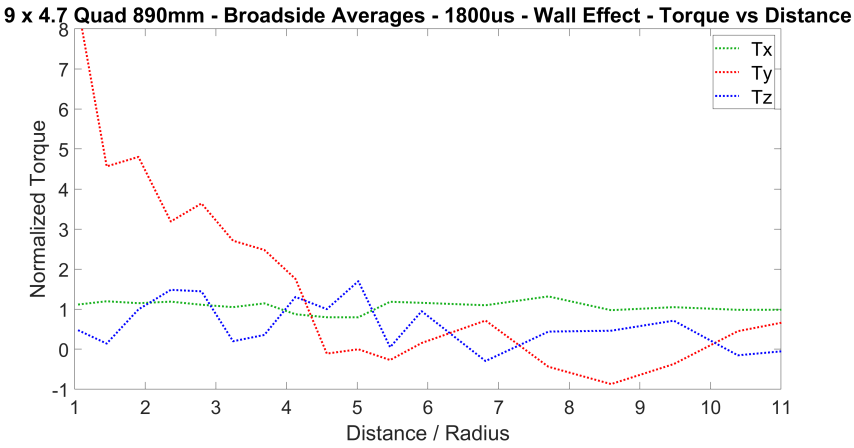

(b) Normalized reaction torques at 90% throttle.

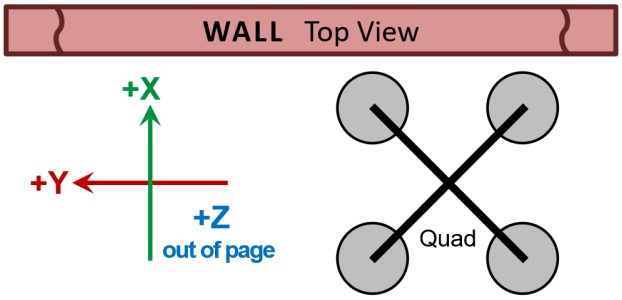

(c) Broadside orientation with color-coded F/T measurement axes.

Figure 5.10: Force and torque due to wall effect for broadside 890 mm quadrotor configuration according to color-coded measurement axes in illustration. Throttle set point at 90%.

Chapter 6

Multirotor Ground Effect Model

The work presented in this dissertation represents a comprehensive study of wall, ceiling, and ground effect using empirical methods. The UAV community has demonstrated a particular interest in ground effect and ceiling effect, often for the purpose of extending flight time by exploiting the increased lift generated for a given power expenditure. The results presented in Chapter 4 indicate that existing helicopter theory can accurately predict the increased lift that a multirotor experiences in ceiling effect. Conversely, the results presented in Chapter 3 show that the classical Cheeseman-Bennett model for full-scale conventional helicopters, defined by (2.5), does not correctly predict ground effect for multirotors. The common trend amongst many UAV researchers to apply the Cheeseman-Bennett model to a multirotor aircraft without determining whether or not it is accurate, has created a research barrier that cannot be overcome unless a multirotor-specific ground effect model is developed. If research and autopilot development is taking place based on an invalid assumption that (2.5) is accurate for multirotor UAVs, the potential contribution of such work is limited. To provide a more accurate prediction of ground effect for the UAV community, an alternative to the classical Cheeseman-Bennett model is required that is formulated for small-scale multirotor aircraft.

This chapter describes, in detail, the process of developing and validating a parametric ground effect model specifically intended for multirotor UAVs. The chapter is structured to reflect the step-by-step procedure that is used to develop a system of equations to predict ground effect that rely on basic aircraft specifications as inputs. The model's input parameters can be easily measured for any aircraft design, generating a set of coefficients that are constant for the given aircraft. With the basic measurements known, the model can be used in place of (2.5), outputting the thrust ratio T_{IGE}/T_{OGE} as a function of the height ratio Z/R assuming the UAV has an on-board sensor to measure height from the ground. The intention is to provide a similarly convenient method of predicting multirotor ground effect that has made (2.5) the standard for conventional helicopters.

6.1 Curve Fitting Procedure

The results presented in Chapter 3 show that the classical Cheeseman-Bennet ground effect model for conventional helicopters, defined by (2.5), differs greatly from the observed ground effect performance of various multirotor configurations. The equation structure of (2.5) is a decaying exponential form, however, the observed multirotor ground effect curves do not follow this form. Therefore, the initial inclination to modify (2.5) by adding additional terms or correction factors is not feasible because no permutation of a decaying exponential function can fit the data. It is clear that a different equation form is required to accurately fit the ground effect curves from the multirotor characterization study. Because all of the curves display a similar shape, it is reasonable to seek a single equation form (as opposed to a piecewise function) that can fit all of the results.

A curve fitting analysis and optimization procedure is performed on all of the experimental datasets to establish the best candidate equation form with the minimum number of terms that can accurately predict T_{IGE}/T_{OGE} in all of the multirotor test cases. This procedure begins with a few potential equation forms that are known to exhibit similar shapes to what is observed in the results in Chapter 3. The equation form must be capable of displaying three key behaviors, these are be referred to as *fit requirements*:

1. Exponential or asymptotic growth in T_{IGE}/T_{OGE} towards ∞ as Z/R approaches zero.

2. A single oscillation period about the horizontal line defined by $T_{IGE}/T_{OGE} = 1.0$ with controllable unequal amplitudes and half-periods between the trough and peak.

3. The curve must converge to $T_{IGE}/T_{OGE} = 1.0$ as Z/R increases without any further oscillation.

The possible equation forms that are explored include the following:
a decaying power function with a sinusoidal component of the form (6.1),

$$y = \frac{1 + A\cos(Bx + C)}{Dx^n + E} \tag{6.1}$$

an underdamped negative exponential with a sinusoidal component of the form (6.2),

$$y = Ae^{-\gamma x}B\cos(\omega x - C) \tag{6.2}$$

and a rational polynomial with unequal orders of the numerator and the denominator of the form (6.3).

$$y = \frac{\sum_{i=1}^{n+1} p_i x^{n+1-i}}{x^m + \sum_{i=1}^{m+1} q_i x^{m-1}} \tag{6.3}$$

6.1.1 Equation Form Selection

The interactive MATLAB Curve Fitting toolbox provides an convenient method to test each equation form with relative ease and expediency. The toolbox allows the user to select x and y data from the current workspace variables, in this case the measured T_{IGE}/T_{OGE} and Z/R data from any individual test case. The user can then define the specific equation form that is to be used for the curve fit, either from a list of common generic forms, or a custom user-defined equation form. The toolbox displays the resulting fit of each equation form over the defined data points, as well as the chosen coefficients and quality metrics (aka "goodness of fit") such as residuals. An example screen image of the MATLAB Curve Fitting toolbox is shown in Fig. 6.1.

The interactive toolbox is used to generate curve fits for a single ground effect test, which includes three test cases, and therefore, three discrete datasets. The proposed equa-

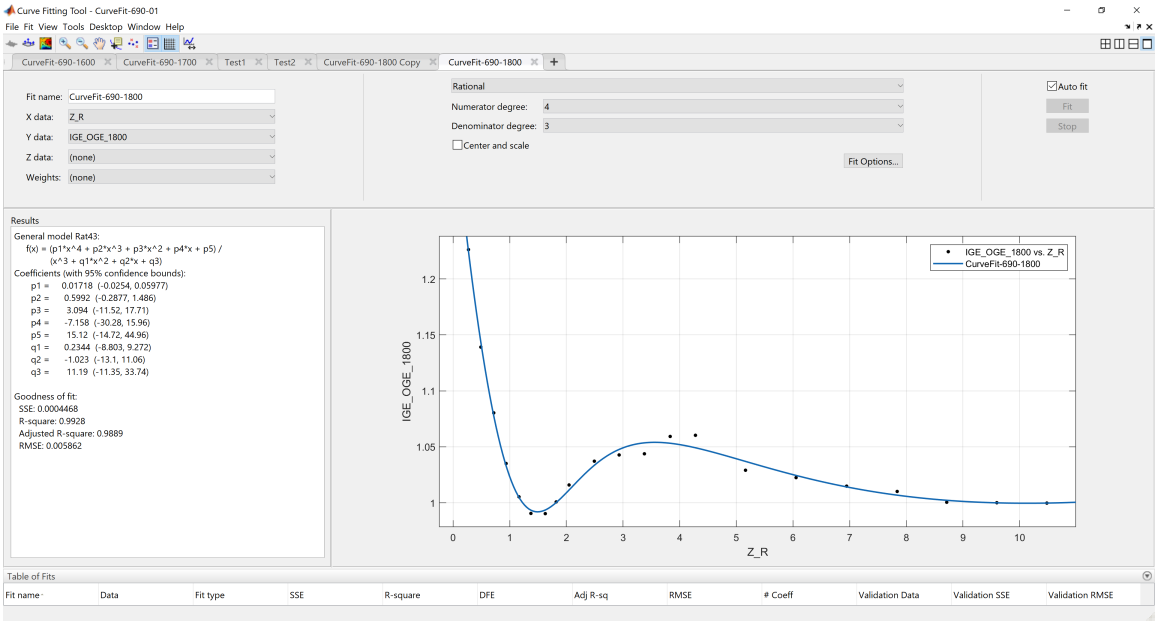

Figure 6.1: Interactive MATLAB Curve Fitting toolbox performing a fit operation on the data from single ground effect test case. The upper portion of the window selects the x and y datasets, the type of equation used for the fit, and the equation parameters. The lower portion of the window displays the fitted curve over the data points, the chosen coefficients, and the "goodness of fit" metrics.

tion forms are applied to each dataset, and the equation parameters are manually tuned to generate the largest R^2 value and satisfy the three fit requirements listed earlier.

The equation with the form of (6.1) has the advantage of having the most similar structure to (2.5), but cannot fully satisfy the second and third fit requirements. Specifically, (6.1) cannot fully converge to $T_{IGE}/T_{OGE} = 1.0$ particularly after a single-period oscillation, and the amplitude of the first trough is always much greater than the amplitude of the following peak. Additionally, the half-periods of the trough and peak cannot differ because they are fixed by the sinusoidal component of the equation, also failing to satisfy the second fit requirement.

The equation with the form of (6.2) can, in fact, converge to $T_{IGE}/T_{OGE} = 1.0$ after a single-period oscillation, as anyone familiar with second-order systems has encountered, thus satisfying the first and third fit requirements. However, (6.2) is also incapable of fully satisfying the second fit requirement in a similar manner as (6.1).

Based on the results obtained using the toolbox, the best candidate equation form is chosen to be the rational polynomial, defined earlier by the generic form (6.3). This is the only candidate equation that can fully satisfy all three fit requirement, and consistently produced the largest R^2 values for all of the data sets. Generally, using a higher-order form of (6.3) produces R^2 values that are closer to 1.0, thus indicating a more accurate fit to the data. The trade-off is the increased bulk and complexity of a higher-order equation, and ultimately, the usefulness and convenience of the final equation to UAV researchers must be considered. A compromise is made to use an equation with the lowest order (and therefore the fewest terms) while still producing a quality fit with an $R^2 \geq 0.950$ in all test cases. The final equation form that is chosen for the multirotor ground effect model is defined by (6.4), which produces a fit with an $R^2 \geq 0.985$ for each individual test case data set.

$$\frac{T_{IGE}}{T_{OGE}} = \frac{p_1 x^4 + p_2 x^3 + p_3 x^2 + p_4 x + p_5}{x^3 + q_1 x^2 + q_2 x + q_3} \qquad Where: \quad x = \frac{Z}{R} \tag{6.4}$$

6.1.2 Curve Fitting Refinement and Optimization

The MATLAB Curve Fitting toolbox is an easy interactive method of generating equations of various forms to fit a set of data points. There are, however, limitations in the toolbox's input parameters, adaptability and usefulness for post-processing and manipulation of the generated outputs. These limitations are especially apparent when performing numerous curve fits that must later be analyzed and compared to one another to generate further correlations between multiple datasets. As such, the interactive toolbox is only used to determine the best equation form to fit the data, and some basic starting parameters from which to formulate additional curve fits on other datasets. From this point, the remaining curve fitting procedure, post-processing and associated analysis are accomplished within the traditional MATLAB scripting environment.

Generating the code for a particular curve fit from within the toolbox is straight-forward, but the code needs to be adapted to overcome some of the toolbox's limitations. The code can be modified to allow multiple consecutive curve fits on different datasets to be output to the same data structure, allowing for subsequent comparisons of the various fits and their coefficients. The code for a single curve fit is then duplicated for all of the remaining test cases in the ground effect study, generating the coefficients and "goodness of fit" metrics for each case.

Occasionally, a curve fit does not appear to follow the trend of the data points, with one or two asymptotic discontinuities in the middle of the plot where the curve goes to $\pm\infty$ then converges back towards the data points, as shown in Fig. 6.2. It is discovered that these discontinuities are being intentionally created by the curve fitting algorithm, which by default,

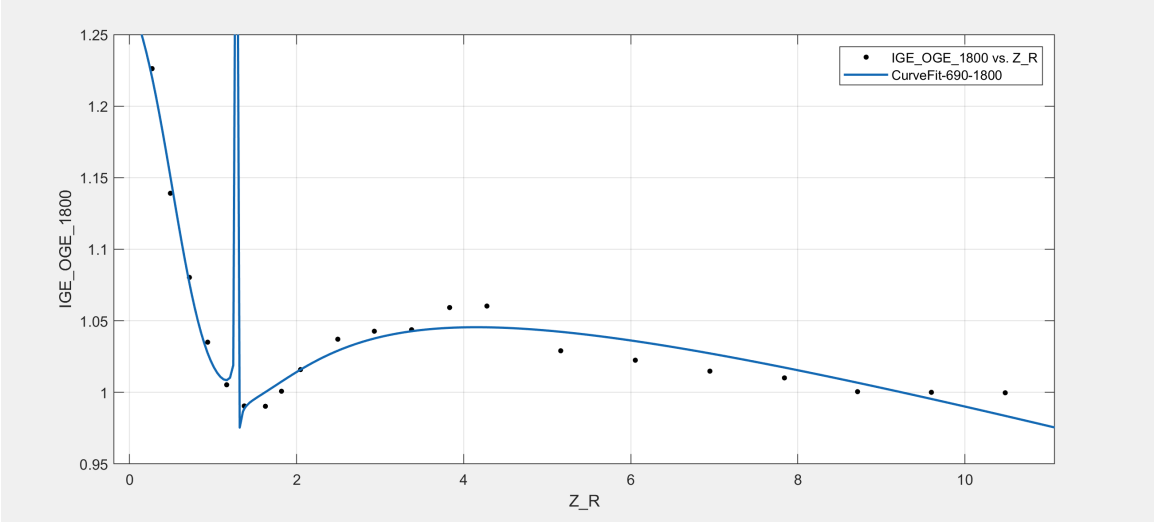

Figure 6.2: Example of a discontinuity in a fitted curve as a result of the optimization algorithm attempting to maximize the R^2 value.

is controlled entirely by a cost function for maximizing the R^2 value. Further investigation of the discontinuities reveals that they are allowing the fitted curve to closely intersect a data point that would otherwise be an outlier, and thus, decrease the R^2 value. Unfortunately, even an occasional discontinuous curve is unacceptable, and would invalidate the rest of the ground effect modeling process that relies on comparison and correlation of the coefficients from various curve fits. Specifying a different optimization algorithm (Levenberg-Marquardt) that uses more than one cost function resolves the discontinuity problems by accepting an outlier data point that reduces R^2 in favor of maintaining a smooth curve. The after further comparison of the algorithms, the Levenberg-Marquardt algorithm is chosen for all of the curve fit operations because it produces more consistent and smooth curves for all of the data with minimal decreases in the R^2 values.

All of the information for each individual curve fit is stored in a single cellular data structure in the MATLAB workspace. After the curve fitting process has been completed for each test case, the associated coefficients are copied into a $n \times 8$ matrix, with n being the number of test cases and eight columns for the coefficients of (6.4) generated by a

single curve fit. Using the same process, a $n \times 1$ vector is created to store the R^2 values of each curve fit. Once in matrix / vector form, the curve fit outputs can be easily viewed and accessed by the subsequent operations in the code.

In three of the test cases, the curve fit coefficients are observed to be 3-5 orders-of-magnitude higher than the rest of the fitted curves, yet surprisingly, they still had similar shapes and high R^2 values. It is apparent that the same curve can be generated using two unique sets of coefficients of vastly different magnitudes, as long as they are appropriately matched with the correct proportionality. While intriguing, it is not practical to for the curve fits to have such variation because the coefficients must later be correlated to the physical parameters that correspond to each test case. It's desirable that all of the values in each column of the final coefficient output matrix are within one order of magnitude. The offending curve fit operations are provided with additional upper and lower bounding parameters to constrain the acceptable range of coefficients available to the optimization algorithm. Additionally, predefined start points for all eight coefficients are defined using averages from curve fits of other similar datasets.

The final R^2 values across all of the curve fits for the ground effect study range from $0.981 \leq R^2 \leq 0.998$ with an average of $R^2 = 0.989$, indicating that the curve fit procedure is successful and accurate. With all of the multirotor ground effect data fitted with a curve of the same equation form, and all of the resulting coefficients within an acceptable range, the curve fitting procedure is complete. The next step in the development of a multirotor ground effect model is to correlate the change in the coefficient values with the physical test parameters that are the independent variables of the ground effect study.

6.2 Development of a Parametric Model

This section focuses on the physical experiment parameters that are explored in the ground effect study described in Chapter 3. The goal is to correlate changes in the physical independent variables with corresponding changes in the curve fit coefficients between each respective test case. This section focuses on three physical parameters used throughout the ground effect study:

- Propeller spacing (L), measured in millimeters across the diagonal of the multirotor from center-to-center at the motor's centerline axis of rotation.
- Propeller size (R), measured as the propeller radius from the centerline of the motor shaft to the tip of the propeller blade (i.e. blade chord length plus hub radius). Since propellers are most commonly sized in inches, this unit is used in the plots for easier comparison, but in the ground effect model R is converted to millimeters for consistency.
- Motor / propeller speed (ω), measured in rotations per minute (rpm) based on telemetry from the motor speed controllers.

Each of these physical parameters is investigated as an isolated independent variable that is incremented between various test cases while keeping the other parameters constant. This experimental methodology is intended to produce quantifiable trends that will be reflected in the data and subsequently the curve fit coefficients. The raw coefficient values of the curve fits are not explicitly listed during the comparisons because it is difficult to identify trends from a table of numbers. Instead, this section presents plots of the eight coefficients as a function of the physical parameters, thus graphically illustrating the trends and correlations. The final multirotor ground effect model includes parameterized

functions for all eight coefficients which can be used to calculate the numeric values in any specific case, if so desired.

6.2.1 Propeller Spacing Parameterization

As described in Chapter 3, one of the features of the instrumented test stand includes a quadrotor test frame, shown in Fig. 3.8, that accommodates various propeller spacings using incremented motor mounting locations across the arms of the frame. This experimental apparatus facilitates studying the effect of propeller spacing on the measured ground effect curves. The test cases that apply to correlating propeller spacing use the same 9×4.7 nylon propellers ($R = 114.3mm$), but include multiple cases at three throttle settings ($\omega = 7000$, $\omega = 8400$, and $\omega = 9600rpm$). To isolate L as the physical parameter of interest, the coefficients of the three test cases at each spacing are averaged to create a single set of coefficients at each L value. This has the advantage of minimizing the effect of outlier data points in any single test case.

The averaged curve fit coefficients are plotted as a function of propeller spacing L, as shown in Fig. 6.3. There are clear trends in each of the coefficients as the value of L changes in increments of 100 mm.

A simplified curve fitting procedure is applied to each of the coefficient curves in the plot. This procedure applies a quadratic (second-order) fit to define each coefficient as a function of L, with the most simplified equation necessary to provide a good approximation. The resulting parameterized model coefficients as a function of L are defined by the set of equations (6.5).

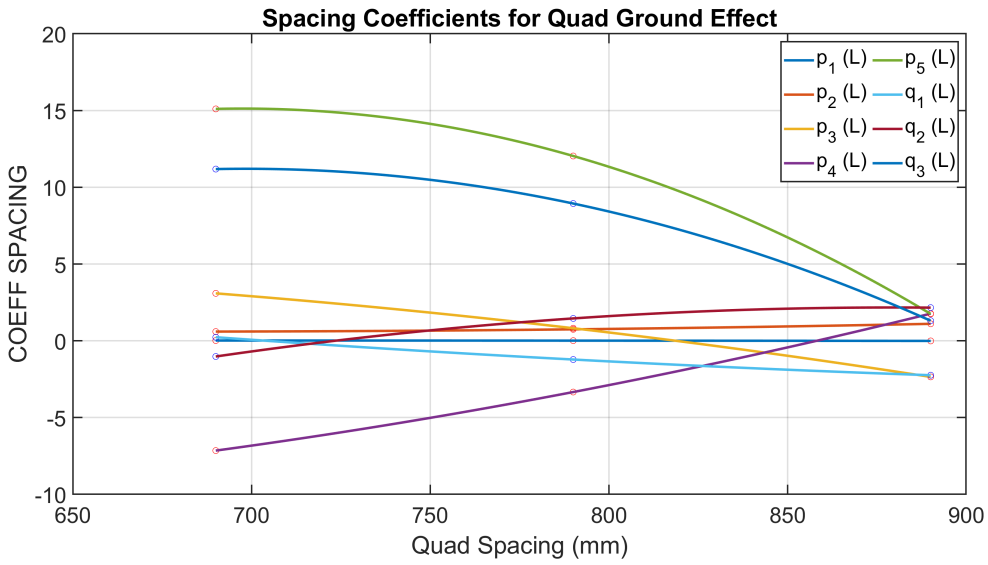

Figure 6.3: Plot of curve fit coefficients as a function of propeller spacing L (mm).

$$
\begin{aligned}
p_1(L) &= -0.000000558(L^2) + 0.0007520(L) - 0.2358072 \\
p_2(L) &= 0.00001063(L^2) - 0.0142738(L) + 5.3865291 \\
p_3(L) &= -0.00004497(L^2) + 0.0438583(L) - 5.7591472 \\
p_4(L) &= 0.00006469(L^2) - 0.0576019(L) + 1.7967276 \\
p_5(L) &= -0.0003640(L^2) + 0.5083474(L) - 162.3486203 \\
q_1(L) &= 0.00002152(L^2) - 0.0463831(L) + 21.9878385 \\
q_2(L) &= -0.00008886(L^2) + 0.1563105(L) - 66.5715394 \\
q_3(L) &= -0.0002718(L^2) + 0.3800496(L) - 121.6408223
\end{aligned}
\tag{6.5}
$$

6.2.2 Propeller Size Parameterization

As described in Chapter 3, multiple propeller sizes are evaluated using the quadrotor test frame at a fixed spacing of 690 mm, the experimental results of which are shown in Fig. 3.14. It is well established by (2.5) that the size of the lifting rotor is directly related to the thrust ratio T_{IGE}/T_{OGE} that defines the ground effect performance of any rotorcraft. The

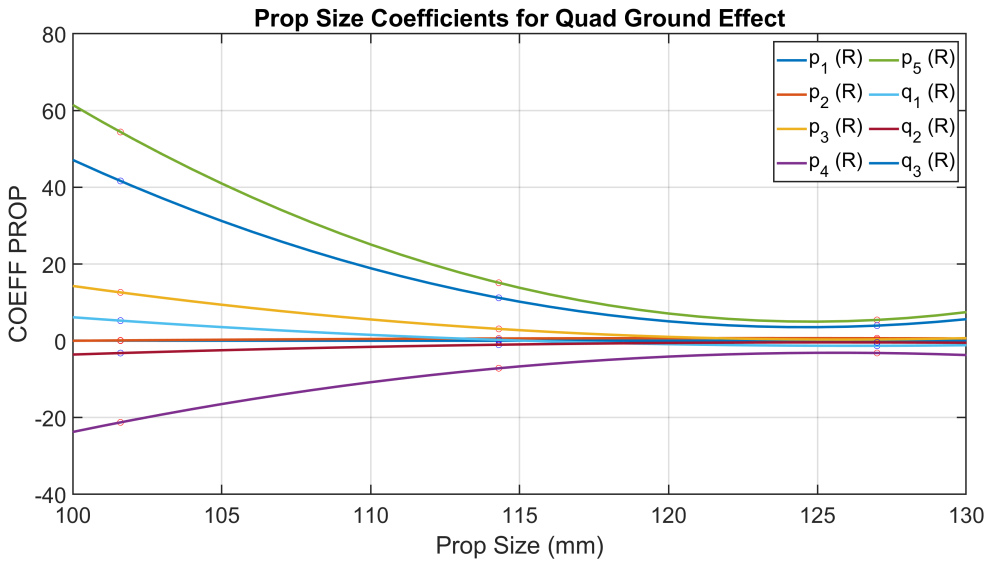

Figure 6.4: Plot of curve fit coefficients as a function of propeller radius R (mm).

test cases that apply to correlating propeller size all use the same $L = 690mm$ spacing, and are all conducted at the same throttle setting ($\omega = 9600rpm$). Therefore, this correlation only provides a single test case for each propeller size R, and does not benefit from the averaging of multiple test cases that is possible in the propeller spacing correlation. The curve fit coefficients are plotted as a function of propeller size R, as shown in Fig. 6.4. Again, there are clear trends in each of the coefficients as the value of R changes.

The same simplified curve fitting procedure that is used in the previous subsection is applied to each of the coefficient curves in the plot. The plot in Fig. 6.4 shows that all coefficients display a trend that is roughly parabolic as R increases. Therefore, a quadratic curve fit is applied to each of the coefficients to avoid oversimplification and create potential errors. The resulting parameterized model coefficients as a function of R measured in millimeters are defined by the set of equations (6.6). It is important to note that when the multirotor ground effect model is applied to a specific aircraft, all of these coefficient equations become numeric constants. In other words, the apparent bulk and complexity of (6.6) does not complicate the final ground effect equation defined by the form (6.4).

$$
\begin{aligned}
p_1(R) &= 0.0000639(R^2) - 0.0150904(R) + 0.9069553 \\
p_2(R) &= -0.0013402(R^2) + 0.3286861(R) - 19.4598466 \\
p_3(R) &= 0.0209858(R^2) - 5.2797888(R) + 332.4024290 \\
p_4(R) &= -0.0313786(R^2) + 7.8848093(R) - 498.4424184 \\
p_5(R) &= 0.0917575(R^2) - 22.9034206(R) + 1434.206622 \\
q_1(R) &= 0.0107960(R^2) - 2.7259295(R) + 170.7625625 \\
q_2(R) &= -0.0048989(R^2) + 1.2289387(R) - 77.4886021 \\
q_3(R) &= 0.0719462(R^2) - 17.930647(R) + 1120.7216262
\end{aligned}
\tag{6.6}
$$

6.2.3 Motor / Propeller Speed Parameterization

The final physical parameter that is investigated in the ground effect study described in Chapter 3 is motor / propeller speed (ω). According to (2.5), the speed and power of the lifting rotor are assumed to be constant, and therefore, are not included in the classical ground effect model for conventional helicopters. One of the goals of the ground effect study is to establish if these assumptions have a significant impact on ground effect performance by varying ω throughout the ground effect study. While the assumption of a constant ω is generally valid for conventional helicopters that use a variable-pitch main rotor at a roughly constant speed, it is not valid for multirotors that use individual motor speeds to provide control authority and modulate the combined thrust to generate lift.

The results of the ground effect study shown in Figs. 3.11 and 3.13 do show minor differences in the T_{IGE}/T_{OGE} curves at the different throttle set-points. The differences in ω, however, do not exhibit any quantifiable trend in T_{IGE}/T_{OGE} between any of the corresponding test cases in the ground effect study. The observation suggests that ω is not an influential physical parameter for modeling ground effect for multirotors. This conclusion is further substantiated by the fact that ground effect performance is most commonly

characterized as the dimensionless thrust ratio T_{IGE}/T_{OGE}, in which the increased thrust generated at a higher ω factors out. The result is that in the ideal scenario, T_{IGE}/T_{OGE} is completely independent of ω, and will be the same at a give Z/R regardless of the propeller speed.

The variations observed in the plots of Figs. 3.11 and 3.13 at different ω values are therefore attributed to random measurement errors that are inherent in even the best experimental apparatus. These determinations indicate there is no purpose in Parameterizing ω in the multirotor ground effect model.

6.2.4 Parametric Model of Multirotor Ground Effect

As this chapter has thus far established, the multirotor ground effect model incorporates the equation form defined by (6.4) with eight coefficient values that are dependent on physical parameters based on the aircraft design. The coefficients of the model have been parameterized for the physical parameters of propeller spacing (L) and propeller radius (R), but only in isolated cases. The next step in the model development procedure is to combine the two parameterized coefficient equations defined by (6.5) and (6.6) into a single set of eight equations that are functions of both L and R.

This is accomplished by solving the system of equations represented by (6.5) and (6.6) using known values of both L and R from test cases that are common to both correlations. The values chosen for this task are $L = 690mm$ and $R = 114.3mm$. The numerical solutions of (6.5) are subtracted from the equations in (6.6) because all of the propeller size test cases are performed at a spacing of $L = 690mm$. Likewise, the numerical solutions of (6.6) are subtracted from the equations in (6.5) because all of the propeller spacing test cases are performed with the same propeller with $R = 114.3mm$. The final set of

model coefficients are the means of the two sets of functions that result from the system of equations, and are defined by (6.7) as functions of both L and R.

$$
\begin{aligned}
p_1(L,R) &= -0.0000002794(L^2) + 0.0003761(L) + 0.00003197(R^2) - 0.0075479(R) + 0.3357119 \\
p_2(L,R) &= 0.0000053178(L^2) - 0.0071388(L) - 0.0006703(R^2) + 0.1643906(R) - 7.0388236 \\
p_3(L,R) &= -0.000022529(L^2) + 0.0219849(L) + 0.0104943(R^2) - 2.6402066(R) + 163.3198037 \\
p_4(L,R) &= 0.000032426(L^2) - 0.0289233(L) - 0.0156903(R^2) + 3.9426111(R) - 248.2897537 \\
p_5(L,R) &= -0.00018056(L^2) + 0.2518899(L) + 0.0458834(R^2) - 11.4527617(R) + 636.8788317 \\
q_1(L,R) &= 0.000010736(L^2) - 0.0231523(L) + 0.0053983(R^2) - 1.3630188(R) + 96.3637597 \\
q_2(L,R) &= -0.000044379(L^2) + 0.0780762(L) - 0.0024483(R^2) + 0.6141837(R) - 71.9829075 \\
q_3(L,R) &= -0.00013482(L^2) + 0.1883013(L) + 0.0359764(R^2) - 8.9660684(R) + 500.2544495
\end{aligned}
\tag{6.7}
$$

These coefficients can be numerically solved for a specific multirotor aircraft design knowing only the values of L and R, and then substituted into the ground effect model (6.8) to provide a numerical prediction of T_{IGE}/T_{OGE} based on the measured height from the ground (Z).

$$
\frac{T_{IGE}}{T_{OGE}} = \frac{p_1 x^4 + p_2 x^3 + p_3 x^2 + p_4 x + p_5}{x^3 + q_1 x^2 + q_2 x + q_3} \qquad Where: \quad x = \frac{Z}{R} \tag{6.8}
$$

6.3 Validation of Parametric Model

The final step in the model development procedure is to validate the parametric equations using the data collected from the ground effect study in Chapter 3. In this section, the proposed multirotor ground effect model is evaluated using a *cross-validation* technique to identify and address potential issues such as *selection-bias* or *overfitting*. The model is tested repeatedly using different subsets of experimental data in various combinations.

In each validation scenario, the experimental data (consisting of every individual test case from the multirotor ground effect study) is partitioned into two unequal sets that do not share any test cases between them. The first partition is called the "*training dataset*," which contains the majority of the test cases, and is used to define the model's parametric equations based on the individual curve fits of each test case. The second partition is called the "*validation dataset*," which consists of the two remaining test cases that are not included in the training dataset. The training datasets used in our analysis consist of ten test cases from a total of twelve, and the remaining two cases in each partition form the validation dataset. Each of the twelve test cases is used in one of the validation datasets, and is part of the training dataset in all the other partitions; ensuring that each test case is utilized equally in the overall analysis.

The various model permutations are used to predict the ground effect curves for their corresponding validation dataset, and the curves are compared to the measured data points from those two test cases. The performance of the model in each scenario is quantified according to how accurately the model-predicted curve fits the given validation dataset (i.e. the R^2 value of each validation test case). The details and results of the cross-validation procedure are shown in Table 6.1 according to the various dataset partitions in the six validation scenarios.

Because the model is defined using the training dataset, then tested using the validation dataset, the resulting predictions are more indicative of a real-world independent prediction scenario. The data partitioning is different for each validation scenario, so the training and validation datasets always contain different combinations of test cases, and each produce slightly different results. If the range of R^2 values across all of the validation scenarios is reasonable, the final model is likely to produce accurate independent predictions across a variety of datasets. The six parametric models from the different cross-validation scenarios

are combined by averaging the coefficients of the parametric equations, thus producing a final parametric model that is more accurate and reliable.

The cross-validation procedure leads to minor changes to the parametric equation coefficients as a result of averaging the results of the six validation scenarios. The set of parametric functions given in (6.7) reflect these changes, and have already been corrected according to the results of the cross-validation. Therefore, the final multirotor ground effect model defined by (6.7) and (6.8) are representative of the combined training models of the six validation scenarios.

Using the parametric model from (6.7) and (6.8), a brief MATLAB script is written to incorporate user-defined L and R values as inputs. One or more arrays of Z values are also input from actual experimental datasets, corresponding to the measured rotor-disk heights above the ground plane in these test cases. Finally, the experimentally measured and post-processed T_{IGE}/T_{OGE} data is input as one or more matrices of three redundant sets of thrust measurements (multiple concurrent data measurements at each point reduces the effect of mechanical vibration and noise). The experimental data is used for comparison, providing a known reference on which to judge the model's accuracy and generalizability . Figs. 6.5 and 6.6 show plots of the model-predicted ground effect for four separate test cases that were not part of the twelve cases used in Table 6.1 or the final model formulation. The independently-sourced measurement data points are scattered as colored markers, while the model-predicted ground effect curves are shown as solid lines of the same color. These plots serve to illustrate the model's accuracy when predicting multirotor ground effect performance for independent "never-before-seen" datasets, thus recreating a "real-world" application scenario.

These plots demonstrate the proposed model's ability to accurately predict the ground effect performance of different multirotor aircraft configurations within a range of physical scales that are representative of many popular modern UAV designs. From the results of

Test Case Parameters		**Data Partitioning for Validation Scenarios**					
#	L , R , ω (mm) , (mm) , (rpm)	**# 1**	**# 2**	**# 3**	**# 4**	**# 5**	**# 6**
1	690 , 114 , 7000	Validate	Train	Train	Train	Train	Train
2	690 , 114 , 8400	Train	Validate	Train	Train	Train	Train
3	690 , 114 , 9600	Train	Train	Validate	Train	Train	Train
4	690 , 127 , 9600	Train	Train	Train	Train	Train	Validate
5	690 , 102 , 9600	Train	Validate	Train	Train	Train	Train
6	690 , 76 , 9600	Train	Train	Train	Validate	Train	Train
7	790 , 114 , 7000	Validate	Train	Train	Train	Train	Train
8	790 , 114 , 8400	Train	Train	Train	Train	Validate	Train
9	790 , 114 , 9600	Train	Train	Validate	Train	Train	Train
10	890 , 114 , 7000	Train	Train	Train	Train	Train	Validate
11	890 , 114 , 8400	Train	Train	Train	Train	Validate	Train
12	890 , 114 , 9600	Train	Train	Train	Validate	Train	Train
R^2 high.		0.9810	0.9754	0.9806	0.9676	0.9801	0.9827
R^2 low.		0.9662	0.9700	0.9779	0.9661	0.9731	0.9737
R^2 avg.		0.9736	0.9727	0.9792	0.9669	0.9766	0.9782
Overall R^2		**0.9745**					

Table 6.1: Breakdown of cross-validation procedure, dataset partitioning, and model prediction performance.

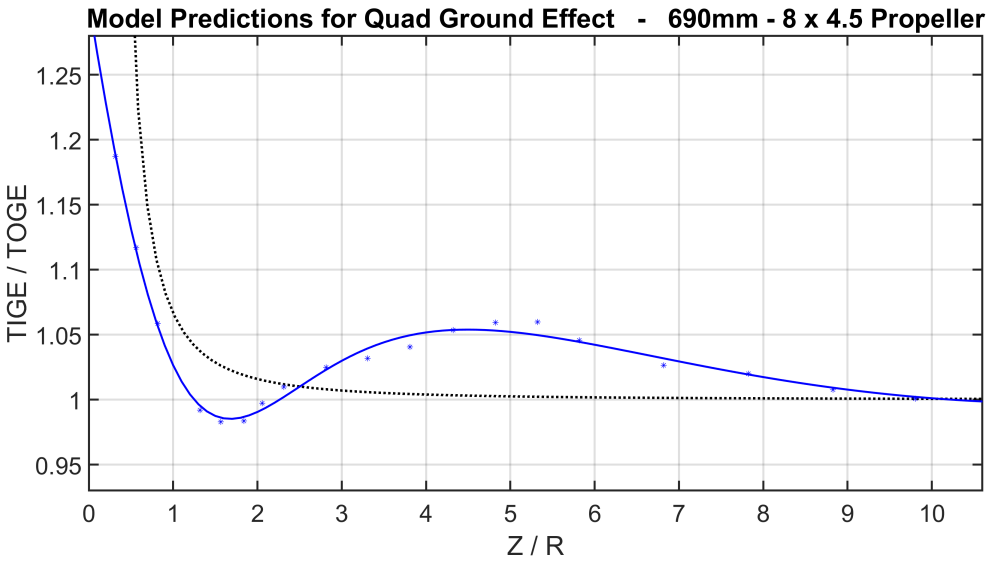

Figure 6.5: Model-predicted ground effect curve for a single test case in a validation dataset. This case is for 8×4.5 composite propellers ($R = 102$mm) at 9600 rpm with a spacing of $L = 690$mm .

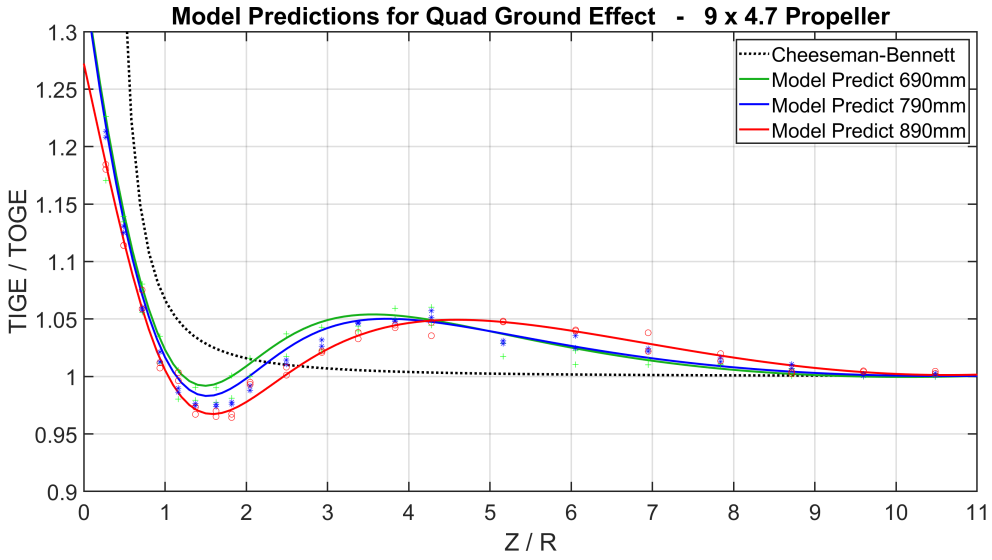

Figure 6.6: Model-predicted ground effect curves for a validation dataset of various propeller spacings L (mm). All cases use 9×4.7 nylon propellers at 8400 rpm.

the model validation, as shown in Table 6.1 and in Figs. 6.5 and 6.6, the accuracy of the parametric model predictions fall within the range $0.9661 \leq R^2 \leq 0.9827$, with an overall mean of $R^2 = 0.9745$ across twelve test cases, well within the generally acceptable level of accuracy of $\pm$ 5%. These performance metrics indicate that the parametric model in (6.7) and (6.8) can be applied accurately to a wide range of different test cases. The R^2 values of the curve fits, discussed in Section 6.1, are slightly higher than those of the final model, but the curves fits only provide this high level of accuracy in specific test case.

This model requires only basic physical parameters as inputs, and a simple piece of code (in any popular programming language) can be written to generate a numerical solution of ground effect thrust for the given aircraft design. Once the aircraft parameters are are set, the model requires only a single measurement input, Z, which can be obtained by a small, simple and inexpensive sensor (e.g. an ultrasonic echo sensor) on-board the UAV. While the model's equation form is more complex than that of (2.5) or (2.7), it is still computationally simple compared to even a basic PID-based flight controller. A basic microcontroller and an inexpensive distance sensor are all that's required to provide real-time ground effect prediction onboard a multirotor UAV. Future research will likely be able to improve upon this model, but information presented in this chapter can provide the UAV community with a more accurate and straight-forward method for predicting the ground effect performance of multirotor UAVs.

Chapter 7

Conclusion & Future Work

The work presented in this dissertation represents a comprehensive research picture of the study of wall, ceiling, and ground effect. The research presented in this dissertation consists largely of empirical data collected under controlled experimental conditions. This dissertation also presents the procedure for modeling ground effect for small-scale multirotor UAVs. This chapter describes the conclusions of this work and its contributions to the UAV research community. This chapter also describes the potential future work that remains in this field of study to accomplish the goal of developing an improved autonomous flight controller.

7.1 Conclusions

The work presented in this dissertation represents a comprehensive empirical study of close-quarter aerodynamic interactions for small-scale multirotor UAVs flying near large surfaces and obstacles. These studies focus on the comparison of single-rotor and multirotor aircraft designs under specific flight conditions. This work has been broken into three topics:

- Ground effect - the apparent increase in lift experienced by an aircraft as it approaches the ground
- Ceiling effect - the apparent increase in lift experienced by an aircraft as it approaches a ceiling
- Wall effect - the apparent attractive force and pitching moment experienced by an aircraft as it approaches a vertical wall

A complete literature review is performed for each of these topics, and if possible, a comparison of single-rotor and multirotor aircraft, and the potential influence the aircraft configuration can have on the observed behavior. Empirical data for each topic is presented, and a comparison to existing theory is provided. A discussion of the results, and explanation of specific observations is offered in the three topic areas. Specific conclusions and contributions for each topic are detailed in the remainder of this section.

7.1.1 Ground Effect

A comprehensive study of ground effect for small-scale UAVs is presented as part of this dissertation. The work presented in Chapter 3 begins by detailing the design and construction of an instrumented test stand and ground effect apparatus for studying UAV performance in ground effect. This test stand and apparatus are later used in the ceiling effect

study that is presented in Chapter 4. Chapter 3 validates the accuracy of the test stand and experimental apparatus by evaluating single-rotor test cases, and comparing the results to the classical theory defined by (2.5).

The claim made in this dissertation is that the classical Cheeseman-Bennett ground effect theory for conventional helicopters cannot be accurately applied to multirotor aircraft due to the interactions between the discrete wakes produced by each of the rotors. This claim is confirmed by the results presented in Chapter 3 for multirotor ground effect performance, which show a clear deviation from the classical ground effect theory defined by (2.5). A detailed discussion is provided in Chapter 3 explaining the rationality for why the multirotor ground effect behavior differs from the classical theory. A discussion is offered for each of the individual characteristics that are observed throughout the multirotor ground effect curves, and literature is presented to substantiate these claims. Chapter 3 concludes that the classical ground effect model for conventional helicopters cannot be accurately applied to a multirotor UAV, and that the development of a new model is necessary to predict multirotor ground effect.

Chapter 6 describes the procedure for developing a multirotor-specific ground effect model based on the empirical data from the ground effect study. This procedure begins with the selection of a suitable equation form that can produce curves that fit the multirotor ground effect data presented in Chapter 3. The modeling procedure continues by applying a set of curve fits to the measured multirotor ground effect data. The coefficients of the curve fit equations are parameterized to correspond to physical measurements of the multirotor aircraft. The easy-to-obtain physical parameters can be input into the final model to generate a numerical prediction of ground effect for a variety of multirotor aircraft. The final multirotor ground effect model is validated through its application to various test scenarios, and studying the quality of the model fit to the measured data points. Chapter 6, therefore, provides a user-friendly model for multirotor ground effect that can be incor-

porated into an autonomous flight controller to provide an accurate prediction of ground effect performance.

7.1.2 Ceiling Effect

This research also presents a comprehensive study of ceiling effect for both single-rotor and multirotor small-scale UAVs. The results presented in Chapter 4 describe the hovering performance of a single isolated propeller at varying distances to the ceiling. The chapter also presents hovering performance data for various quadrotor configurations at similar distances to the ceiling. In both cases, this data is compared to the classical theory for predicting ceiling effect given by (2.8).

The results of the ceiling effect study support the claim that (2.8) can accurately predict the apparent increase in lift experienced by an aircraft in close proximity to the ceiling. This is true for both single-rotor and multirotor UAV configurations. Furthermore, the discussion in Chapter 4 describes the reasoning for this agreement with the classical theory in contrast to the ground effect study. This research concludes that the classical theory given by (2.8) can be effectively used in future development of autonomous flight controllers to predict the aircraft behavior in proximity to a ceiling or other similar horizontal overhead surface.

7.1.3 Wall Effect

Finally, this dissertation describes an empirical study of near-wall effect for small-scale multirotor UAVs. Chapter 5 details the design and construction of a wall effect testing apparatus that is implemented to evaluate wall effect for UAVs. The results presented in Chapter 5 describe the hovering performance of a quadrotor UAV at various distances

from a large vertical wall. This data is compared to the limited existing research into characterizing wall effect and understanding the mechanisms involved.

The results of the wall effect study show both a horizontal force that pulls the aircraft towards the wall, and a pitching moment that rotates the top side of the aircraft towards the wall. The literature review of wall effect has suggested that researchers believe that the pitching moment is the cause of the attractive force between the wall and the UAV. By pitching the aircraft towards the wall, the thrust vector is no longer vertical, and is pointed slightly towards the wall. It is hypothesized that this is therefore responsible for pushing the UAV towards the wall.

The results presented in Chapter 5 are the first to demonstrate that the attraction force is not a result of of the pitching moment. Because the experimental apparatus used in the wall effect study completely immobilizes the UAV test frame, the pitching moment cannot produce the necessary change in aircraft pose that is necessary to create a resulting change in thrust vector. The data presented in this dissertation establishes that the pitching moment and the attractive force acting on the aircraft due to the proximity of the wall are not coupled, and are not related. This research established that two independent external forces are enacted on the aircraft as a result of flying near the wall.

7.2 Future Work

This research presents a comprehensive study of ground effect, ceiling effect, and wall effect, as well as a model for predicting ground effect for multirotor UAVs. The work presented here represents a significant step towards the development of improved autonomous flight controllers for multirotor UAVs that are specifically designed to cope with the aerodynamic effects of flying close to walls, ceilings and floors. Future work will be able to focus on the control systems and software development necessary to achieve this goal. Future

researchers can directly apply the information from the ceiling effect and ground effect studies in Chapters 3, 6 and 4 to begin development of an improved flight control system. This information can be accurately applied to a variety of multirotor aircraft designs.

Further investigation of ceiling effect and ground effect may include studying the extreme scales of multirotor UAV platforms (i.e. very large aircraft and micro-scale aircraft). Future work may also include similar studies at extreme altitude, temperature and other environmental conditions. Finally, a study of rotor count may reveal if unusual UAV designs with eight or more rotors could have a significant impact on ground effect.

Additional research into wall effect is also a likely avenue for future UAV research. While this dissertation provides valuable information into the interactions of flying near a wall, it is not a complete investigation with respect to different UAV scales and configurations. Because there is no established theory for predicting wall effect, future work on this topic could produce a completely new set of UAV dynamics to govern flight behavior near walls.

Advances in computational methods and simulation could also provide future UAV research with interesting and significant contributions to the community. The development of CFD simulations could provide valuable insights into the aerodynamic mechanisms that produce ground, ceiling and wall effect. Large-field stereo PIV studies may also reveal some of the flow patterns for a variety of UAV aircraft. As computational power increases, these possibilities may soon become a reality.

Bibliography

[1] J. Alvarenga, N. I. Vitzilaios, M. J. Rutherford, and K. P. Valavanis. "scaled control performance benchmarks and maneuvers for small-scale unmanned helicopters". In *2015 54th IEEE Conference on Decision and Control (CDC)*, pages 6035–6042, December 2015.

[2] J. Alvarenga, N. I. Vitzilaios, and K. P. Valavanis. "survey of unmanned helicopter model-based navigation and control techniques". In *Journal of Intelligent & Robotic Systems (JINT)*, volume 80, pages 87–138, December 2014.

[3] Cecilia R. Aragon and Marti A. Hearst. "improving aviation safety with information visualization: A flight simulation study". In *Air Transportation and Safety*. NASA Ames Research Center, January 2005.

[4] Bellinger. "experimental investigation of effects of blade section camber and planform taper on rotor performance". In *USAAMRDL TR 72-4*, 1972.

[5] S. Bouabdallah and R. Siegwart. "design and control of a miniature quadrotor". In *Advances in Unmanned Aerial Vehicles*, page 171â€"210. Springer Press, 2007.

[6] A. R. S. Bramwell. *Bramwell's Helicopter Dynamics*. AIAA, 2001.

[7] Fernando Caracena, Ronald L. Holle, and Charles A. Doswell III. "vortex-ring circulation in a microburst". In *Microbursts: A Handbook for Visual Identification*, pages 5, 8, 9–14. NOAA/ERL/NSSL Mesoscale Research Division, February 1989.

[8] I.C. Cheeseman and W.E. Bennett. "the effect of the ground on a helicopter rotor in forward flight". In *Technical report, Aeronautical Research Council*. H.M. Stationery Office, 1957.

[9] S. A. Conyers, M. J. Rutherford, and K. P. Valavanis. “an empirical evaluation of ceiling effect for small-scale rotorcraft”. In *2018 International Conference on Unmanned Aircraft Systems (ICUAS)*, pages 243–249, June 2018.

[10] S. A. Conyers, M. J. Rutherford, and K. P. Valavanis. “an empirical evaluation of ground effect for small-scale rotorcraft”. In *2018 IEEE International Conference on Robotics and Automation (ICRA)*, pages 1244–1250, May 2018.

[11] K. Ryan D. C. Robinson, H. Chung. “computational investigation of micro rotorcraft near-wall hovering aerodynamics”. In *Unmanned Aircraft Systems (ICUAS), IEEE International Conference on*, pages 1055–1063, May 2014.

[12] G. M. Eberhart. “modeling of ground effect benefits for multi-rotor small unmanned aerial systems at hover”, December 2017.

[13] G. M. Eberhart and J. Wilhelm. “impact of varied power setting on thrust of multi-rotor vtol suas in ground effect”. In *AIAA Information Systems: AIAA Infotech @ Aerospace*, page 0226, January 2017.

[14] G. M. Eberhart and J. Wilhelm. “development of a ground effect bemt analysis method for multirotor suas”. In *AIAA Information Systems: AIAA Infotech @ Aerospace*, page 0747, January 2018.

[15] W. Engelhardt and A. Teleki. “high speed flight tests with the bo 105 rigid rotor helicopter”. In *Society of Experimental Test Pilots, 7th Annual European Section Symp.*, 1975.

[16] R. Eppler and D. M. Somers. “a computer program for the design and analysis of low-speed airfoils, including transition”. In *NASA TM-80210 and NASA TM-81862*, August 1980.

[17] Federal Aviation Administration (FAA). Advisory circular (ac) 61-13b. In *Basic Helicopter Handbook*. FAA, U.S. Department of Transportation, 1978.

[18] Flight Standards Service FAA. “helicopter emergencies and hazards rotorcraft flying handbook”. In *FAA Manual H-8083-21*, pages 5–11. FAA, U.S. Dept. of Transportation, 2001.

[19] Fradenburgh. “the helicopter and the ground effect machine”. In *JAHS 5-4*, 1960.

[20] S. Gao, C. Di Franco, D. Carter, D. Quinn, and N. Bezzo. “exploiting ground and ceiling effects on autonomous uav motion planning”. In *Unmanned Aircraft Systems (ICUAS), IEEE International Conference on*, June 2018.

[21] Hayden. “the effect of the ground on helicopter hovering power required”. In *AHS 32nd Forum*, 1976.

[22] C. G. Hooi, F. D. Lagor, and D. A. Paley. “flow sensing, estimation and control for rotorcraft in ground effect”. In *IEEE Aerospace Conference (IAC)*, June 2015.

[23] J. Huang and K.T. Chan. “dual-wavelike instability in vortex rings”. In *5th Annual IASME/WSEAS International Conference on Fluid Mechanics and Aerodynamics*, pages 258–262, August 2007.

[24] Wayne Johnson. “vertical flight i & ii”. In *Helicopter Theory*, pages 28–91, 93–124. Princeton University Press, 1980.

[25] K. Knight and R. A. Hefner. “analysis of ground effect on the lifting airscrew”. In *NACA TN 835*, 1941.

[26] D. Lee, A. Awan, S. Kim, and H.J. Kim. “adaptive control for a vtol uav operating near a wall”. In *Guidance, Navigation, and Control, AIAA International Conference on*, 2012.

[27] J. G. Leishman. “helicopter performance”. In *Principles of Helicopter Aerodynamics, 2nd ed.*, pages 258 – 260. Cambridge University Press, 2006.

[28] T. J. Maxworthy. “the structure and stability of vortex rings”. *Journal of Fluid Mechanics*, 51(1):15â€“32, 1972.

[29] B. W. McCormick. *Aerodynamics of V/STOL Flight, 1st ed.* Academic Press, 1967.

[30] B. W. McCormick. “the production of thrust”. In *Aerodynamics, Aeronautics, and Flight Mechanics, 2nd ed.*, pages 291–316. John Wiley & Sons, 1995.

[31] G. Heredia P. J. Sanchez-Cuevas and A. Ollero. “multirotor uas for bridge inspection by contact using the ceiling effect”. In *Unmanned Aircraft Systems (ICUAS), IEEE International Conference on*, June 2017.

[32] D. J. Pines and F. Bohorquez. “challenges facing future micro-air-vehicle development”. In *in Journal of Aircraft, vol. 43, no. 2*, pages 290–305, April 2006.

[33] C. Powers, D. Mellinger, A. Kushleyev, B. Kothmann, and V. Kumar. “influence of aerodynamics and proximity effects in quadrotor flight”. In *International Symposium on Experimental Robotics*, June 2012.

[34] R. W. Prouty. “aerodynamics of hovering flight”. In *Helicopter Performance, Stability, and Control, 1st ed.*, pages 63–68. Krieger, 1995.

[35] W. J. M. Rankine. “on the mechanical principles of the action of propellers”. In *Transactions of the Institute of Naval Architects*, pages 13–30, 1865.

[36] V. J. Rossow. “effect of ground and/or ceiling planes on thrust of rotors in hover”. In *Technical report, NASA-TM-86754, REPT-85256, NAS 1.15:86754*. NASA Ames Research Center, July 1985.

[37] I. Sharf, M. Nahon, A. Harmat, W. Khan, M. Michini, N. Speal, M. Trentini, T. Tsadok, and T. Wang. “ground effect experiments and model validation with draganflyer x8 rotorcraft”. In *Unmanned Aircraft Systems (ICUAS), IEEE International Conference on*, pages 1158–1166, May 2014.

[38] Kristen Starr. “eluding aeolus: Turbulence, gusts, and wind shear”. In Richard P. Hallion, editor, *NASA’s Contribution to Aeronautics, vol. 2*, pages 2–64. National Aeronautics and Space Administration, 2010.

[39] Tim Tucker. “flying through the vortex”. *Rotor & Wing International*, September 2015.

[40] Th. von Karman. “from the propeller to the space rocket”. In *Aerodynamics, 1st ed. (Cornell University Press, 1954)*, pages 166–173. McGraw-Hill, 1963.

[41] Wikipedia. 2.2 radio controlled multirotors, April-16 2018. Online; accessed 17-May-2018.

[42] YouTube. Quadcopter ”wobble of death”: Vrs recovery and avoidance, August-1 2014. Online; accessed 17-May-2018.

[43] J. Zbrozek. “ground effect on the lifting rotor”. In *British R&M 2347*, 1950.